Surface and Interface Modes in Microwave Graphene-like Systems

Thesis

Submitted by Yulia Dautova to the University of Exeter as a thesis for the degree of Doctor of Philosophy in Physics
June 2022

College of Engineering, Mathematics, and Physical Sciences
UNIVERSITY OF EXETER

I certify that all material in this thesis which is not my own work has been identified and that no material has previously been submitted and approved for the award of a degree by this or any other University.

Yulia Dautova

June 2022

Women are not the same as men, but this does not mean they are second-class people. Current trends to erase all the uniqueness and differences between men and women are terrifying. Women have a special and unique role in this Universe, as do men. I truly believe that the main focus of the majority of women's lives is her family, with very few exclusions.

This research was done for my family, and with great support from them. Thus I want to dedicate this work to my family, who give my life meaning.

ACKNOWLEDGEMENTS

It takes a village to write up a thesis.

First of all, I would like to thank my supervisors, Prof Alastair P Hibbins and Prof J Roy Sambles, for their academic support and inspiration. I have learnt a lot from you and enjoyed being your student. I know that I wasn't an exemplary student – that is difficult in your 30s, when life has many other responsibilities. I am incredibly thankful to you for both pushing me and going easy on me when I needed it.

I would also like to acknowledge the EPSRC and the University of Exeter for giving me the opportunity to participate in their PhD programme and the training provided.

Every time I needed support, the doors of Misha Portnoi's office were always open. I was leaving afterwards with the feeling "Life is beautiful!". Every time I was struggling with theory, I would turn to Andrey Shytov's office. And was leaving afterwards with the feeling "I know that I know nothing". I value all you've done for me and I am thankful to you both for making my PhD experience much brighter and smoother.

Among other academics at the University of Exeter, I also want to say a big thank you to Feodor Ogrin, Volodymyr Kruglyak, Eros Mariani, Ian

Hooper and Saverio Russo. I can not forget my two undegradute lectors Lev Markovich Baskov, RIP, and Pavel Zorikovich Mkrtychyan, who nearly 20 years ago instilled in me a love to STEM.

I would also like to thank the people who welcomed us in Exeter and made us feel at home: Nadya Keenan, Fr. Peter and Irina Scorer, Fr. Porphyrios, Veronika Malby and Vesta Zavgorodnia.

Thanks to my friends, who have supported and helped me in various ways: Lena Onishko, Vicky Kyrimi, and Hannah Martins; to Inna Kurnikova and Margrieta Mikelane who became very close to our family.

It goes without saying how thankful I am to my family. To my parents and parents-in-law, to my brother and brother-in-law. You have always stuck by me, even from miles and thousands of miles away. And especially to my mum and mother-in-law, who were always ready to help, putting their own lives on hold. I hope that I will follow your example and do this for my children.

Finally, but most importantly, I thank my husband for:

1. Challenging me to study a PhD
2. Believing in me that I can do it
3. Explaining Physics, even when you were tired after a long day at work
4. Inspiration in my writing and proofreading my thesis
5. For just being my husband and being a pillar of strength
6. For two lovely children

...and for a million other things.

Abstract

Many concepts from solid state physics may be applied to electromagnetic waves propagating in periodic media. A large class of materials, called photonic crystals, that to some measure mimic natural materials, have been extensively studied since the end of the 20th century. In the last decade, after the isolation of the first two-dimensional material, graphene, interest in the artificial graphene systems has emerged. This work presents the results of mimicking graphene with the two microwave artificial analogues. The simplicity of the fabrication process and measurement techniques means they are perfect candidates for studying physics in natural graphene. By measuring near-fields across the samples we not only obtain local distribution of the electric fields, but are also able to plot the experimental dispersion relationships that are lacking in previous studies.

The first artificial graphene comprised of cylindrical metallic rods, which replicate carbon atoms, was fabricated and characterised. Dispersion curves of the bound electromagnetic eigenmodes were experimentally determined by measuring the electric near-fields just above the surface. Two linear crossings are evident in these dispersion curves at each of the K and K′ points of the Brillouin zone, mimicking the well-celebrated Dirac cones in real graphene. Breaking inversion symmetry of the system, which leads to the opening of the band gap, is also demonstrated in this work.

The second structure with a smaller ratio of out-of-plane to in-plane di-

mensions, more akin to real graphene, is comprised of in-plane metallic wires forming a hexagonal mesh. In this configuration, metal wires replicate bonding terms between the carbon atoms in graphene. Like the first structure, it features gapless Dirac dispersion at the corners of the Brillouin zone. We propose a simple, analytical LC circuit model capable of representing the electrodynamics of propagating modes inside the hexagonal mesh. Dispersion curves calculated with this circuit model are shown to fully match the experimental data using realistic values of the inductance and capacitance of the wire mesh. We suggest and show experimentally that by modifying wires individually one can introduce an effect similar to straining of the graphene.

The latter structure was used for studying topological edge modes supported at the interface between the two oppositely modified structures. A new super-cell of the hexagonal wire mesh lattice results in a double Dirac cone at the Γ point. Contraction and expansion of the hexagon in the super-cell open the trivial and non-trivial band gaps. Edge modes that exist at the interface of the expanded and contracted structures are studied. We reveal that the direction of the interface may or may not protect the edge modes from being hybridised. By scanning and measuring the near-field across the entire sample comprised of the two modified structures we obtain dispersion relationships for both surface and edge modes simultaneously. The manifestation of the edge modes hybridisation is shown in measured near-field distributions and supported by the analytical LC model and the effective Hamiltonian description.

TABLE OF CONTENTS

List of Figures

Figure **Page**

Acronyms List

1D One-Dimensional 20

2D Two-Dimensional 20

3D Three-Dimensional 20

AC Alternating Current 39

AG Artificial Graphene 12

BZ Brillouin Zone 11

CNC Computer Numerical Control 47

CS Contracted Structures 137

DC Direct Current 19

EM Electromagnetic 19

ES Expanded Structures 137

FEM Finite Element Method 65

FFT Fast Fourier Transform 12

IDE Integrated Development Environment 118

MTM Metamaterial 61

PBG Photonic Band Gap 43

PEC Perfect Electrical Conductor 77

PML Perfectly Matched Layer 77

CHAPTER 1

INTRODUCTION

The metal-dielectric interface supports Electromagnetic (EM) surface waves over a wide range of frequencies, from radio to optical. At optical frequencies, propagating modes are strongly localised at the interface and are commonly called Surface Plasmons (SPs) or Surface Plasmon Polaritons (SPPs). At microwave frequencies, this same mode is very weakly localised to the surface. For comparison, at a microwave frequency of 10 GHz (λ = 3 cm) the penetration depth into the metal (e.g. silver) is 0.6 μm (1/50000 λ), and the decay length in the air is 40 m (1333 λ) while at an optical frequency of 430 THz (λ = 700 nm) the decay length into a "good" metal, e.g. silver, is of order 25 nm (1/28 λ) and the decay length into the air is just 240 nm ($\approx 1/3\lambda$). Nevertheless, since all EM waves are governed by the same set of Maxwell equations then wave confinement to the surface should be possible at all frequencies below some limit, normally in the ultraviolet, dictated by the electron density within the metal. Thus strictly a confined surface wave exists on metals all the way from the ultraviolet to Direct Current (DC) but generally the label "surface plasmon" (SP) is reserved for visible to infra-red

and at microwave frequencies the mode is simply defined as a surface current.

In the middle of the 20th century it was appreciated that it is possible to much more tightly confine microwaves to the metal-dielectric interface by roughening or corrugating the metallic surface. This topic was revisited by Sir John Pendry in 2004 [1] who provided a new theoretical treatment of confining long wavelength waves to a patterned metal surface. Pendry showed that the electromagnetic properties of a surface penetrated by a periodic array of sub-wavelength holes can be approximated by an effective plasmonic-like dielectric function. The modified dielectric permittivity function is then used to calculate surface wave confinement and dispersion. Akin to optical surface plasmons, the resulting mode disperses away from the light line and asymptotes to the cut-off frequency of an isolated sub-wavelength hole. The term "Spoof Surface Plasmon (SSP)" was coined for bound microwave surface waves supported by corrugated metallic surfaces to highlight the similarity to surface plasmons at optical frequencies.

To demonstrate the similarities between spoof and real surface plasmons it was assumed that both the dimensions and the periodicity of the holes are sub-wavelength. This SSP behaviour is further modified when the periodicity of the corrugated holes approaches the operating wavelength. In this regime the dispersion of the SSP is strongly influenced by the approach to Bragg scattering which results in a plethora of effects. This patterned surface can then be seen as one of the types of Photonic Crystals (PhCs).

PhCs are periodic structures that can be classified as One-Dimensional (1D), Two-Dimensional (2D), or Three-Dimensional (3D) depending on the number of dimensions in which their dielectric function is modulated. While 1D, 2D, and 3D PhCs have been extensively studied theoretically it was the 3D electromagnetic crystals that were seen as analogues to real crystal structures. 2D PhCs did not have a solid state analogue until the first 2D material, graphene, was

experimentally obtained in 2004 by Konstantin Novoselov and Andrey Geim [2]. Graphene is a single layer of carbon atoms arranged into a honeycomb lattice. It is a zero bandgap semimetal with the valence and conduction bands intersecting at the two inequivalent corners of the first Brillouin zone, K and K′. Since its discovery graphene has attracted attention from an extensive range of scientific communities due to its unique properties.

Graphene-like microwave PhC and their supported surface waves is the main subject of this current work. Two different approaches were used to simulate the periodic graphene honeycomb structure for microwaves. In Chapter 4 we replicate the graphene atoms with resonators which interact and couple to each other. The most simple microwave resonator one can think of is a metallic rod. It possesses several resonant frequencies with the dipole resonance occurring when the excitation wavelength is approximately equal to twice the length of the resonator. The fabricated "graphene-like" structure consisted of an array of metallic rods arranged parallel to each other with their centres on a honeycomb lattice within a flat dielectric slab with the rods axes perpendicular to the slab. Results for the dispersion of the microwave modes supported by this structure are presented in the first part of Chapter 4.

The second, very different, approach to mimicking graphene at microwave frequencies is to mimic the coupling between the carbon atoms in graphene by creating a network of metallic links which connect nodes of the honeycomb lattice. This system is studied in Chapter 5. As we show, this structure supports surface waves with the dispersion governed by the symmetry of the resulting hexagonal wire mesh. Such design has several advantages. Firstly, it is more similar to real graphene as its depth is negligible by comparison with its planar dimensions. Secondly, it can be readily fabricated using printed circuit board technology making it cheap to make and easy to modify. Finally, this system can be conveniently simulated with a semi-analytical equivalent

LC circuit model. This model was purposely developed to support analysis of experimental results, and is presented in the second part of Chapter 5.

Both of these microwave graphene systems were studied using the near-field scanning technique which gives direct access to the complete dispersion diagram of the surface waves and their corresponding field profiles. This techniques is described in Chapter 3. We conclude Chapters 4 and 5 by showing how the band structure of surface waves supported by microwave analogues of graphene can be manipulated by breaking the symmetry.

In the last Chapter 6, we study edge modes at the interface between contracted and expanded hexagonal mesh systems. We show how symmetry manipulation can alter band structure, cause band gap opening, and create topologically protected edge states. The developed equivalent *LC* model is utilised to study two types of modes supported by the distinct different edge profiles of the interface. Depending on whether the interface is constructed using zig-zag or armchair edge profiles, it may or may not support topologically protected modes. Using near-field scanning, we measure the amplitude and the phase of the protected and unprotected edge modes, calculate their dispersion diagram, and show how the near-field spatial distribution characterises the type of detected mode. Using an analytical Hamiltonian approach we explain how the edge profile causes hybridisation of the interface modes cancelling their topological protection.

The introductory part of this work is organised as follows. Chapter 2 contains historical and theoretical background. Firstly, we introduce the reader to the concept of surface waves and key publications in this area. The generalised proof of the existence of surface waves at the metal-dielectric interface and their main characteristics are given in this chapter. The second part of Chapter 2 is dedicated to PhCs. Similarly to the first part, we present theoretical concepts and an overview of the key publications. We conclude

Chapter 2 with an introduction to the first 2D material, graphene, and its microwave analogues. The derivation of the graphene dispersion relationship from tight binding approximation is included in this chapter for introductory purpose. Chapter 3 is devoted to experimental and modelling methods used throughout this work. In the first half of this chapter, sample fabrication is described followed by measurement techniques and data processing. The second half of Chapter 3 describes modelling techniques which include Finite Element Modelling and Equivalent LC circuit. The next three chapters contain original work as described earlier. Finally, discussion of the future work is presented in Chapter 7.

CHAPTER 2

BACKGROUND THEORY AND HISTORICAL OVERVIEW

In this chapter we introduce the reader to the terms, historical background, and fundamental theory needed for further reading of this thesis. The chapter is divided into three parts that are structured in a similar way. We provide the review of publications in the discussed scientific area and a corresponding theoretical background.

In the first part we introduce Surface Electromagnetic Waves (SEW) and show how these waves are different from free-space electromagnetic waves. We start with the review of the discovery works of the 20th century as well as more recent applied research. We then derive general solutions for the surface waves, discuss what defines their confinement, and their properties.

The second part is dedicated to Photonic Crystals (PhCs). The review of PhCs is concentrated on microwave structures, including the very first structures and recent works. In this part, we also derive analytical band structure for 1D PhCs to explain how periodicity of the dielectric constant

causes the band gap in the dispersion band structure, pointing out that specific symmetry conditions can cause the gap to close. This leads us to the last section of this background chapter.

The last part includes a detailed review of gapless Two-Dimensional (2D) PhCs with triangular symmetry, often called Artificial Graphene (AG). We will show different types of AG and review studies that have been conducted in this field. The derivation of the graphene band structure using Tight-Binding (TB) is also included in this chapter.

2.1 Surface Electromagnetic Waves

SEWs are a class of EM waves that propagate along the interface between two materials. There is no guarantee that an arbitrary chosen pair of materials will support SEW at a specific frequency. Certain conditions of partnering materials must be satisfied to enable surface wave propagation. A significant class of SEW are supported by the planar metal-dielectric interface, to which this thesis is devoted; another class of SEW are supported by the interface of two homogeneous dielectric materials of which at least one is anisotropic [3].

We start with the discovery of radio SEW at the end of the 19th century. Half a century later there was breakthrough in area of SEW with the discovery of SPPs, the optical equivalent of SEW. We compare and draw similarities and differences between SEW at low and high frequencies. In Section 2.1.2 we provide a derivation for the SEW dispersion, explain the existence of surface waves at the metal-dielectric interface. We also discuss characteristics, such as penetration depth, propagation length, and surface impedance.

2.1.1 Historical Overview

The history of SEWs started in 1899 with Sommerfield's studies of the cylindrical conductor [4]. Later, in 1907 Zenneck mathematically described propagation of EM waves along the surface of another conductor, the Earth, for radio communication [5]. SEWs can only exist as TM waves for the planar interfaces, as will be shown later. However, specially designed surfaces can support TE SEW, as will be shown in this review. SEW is not free radiation, but is determined by collective oscillations of electrons near the surface of the conductor and thus propagates along the surface. However at radio frequencies SEW appears to be highly delocalised extending hundreds of wavelengths into free space. In 1944 Cutler accidentally excited *localised* surface waves along corrugated metallic

surfaces [6]. He was trying to enhance the transmission properties of radar antennae by introducing quarter wavelength deep corrugations on the metal surface, see Fig. 2.1. This study is therefore known to be the first observation of surface waves localised to a corrugated metallic interface. Following Cutler's research, Goubau and others [7–9] considered periodically and randomly roughened materials, e.g., surfaces with distributed sub-wavelength grooves or dimples (rectangular grooves [10–12], sinusoidal surface profile [13, 14]). Rotman showed the existence of bound surface waves on metals with lamellar structure of the surface [15]. Such corrugation allows confinement of the electromagnetic field to the metal-dielectric interface, "effectively" increasing the penetration depth into the metal. Theoretical and experimental studies of the propagation and guidance of the SEW on 1D-2D periodically structured perfectly conducting surfaces are summarised in the book by Maradudin [16].

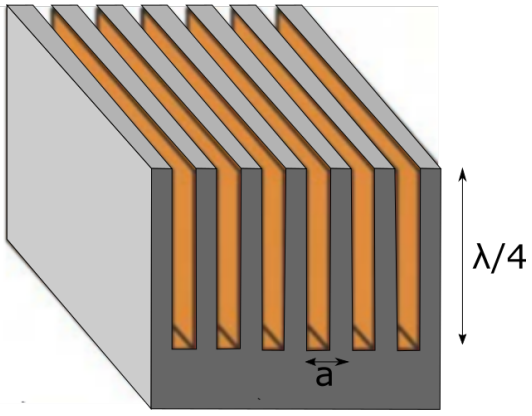

Figure 2.1: A traditionally corrugated surface consists of a metal slab with narrow quarter-wavelength deep slots.

While radio engineers were trying to confine radio waves to the metallic surface by patterning the surface of the metal, in 1957 Ritchie predicted that over the visible range of frequencies surface waves are localised naturally due to relaxation effects of electrons in metals [17]. This SEW was named a "Surface Plasmon Polariton" (SPP) reflecting that the wave involves both charge motion in the metal ("surface plasmon") and EM waves ("polariton") in

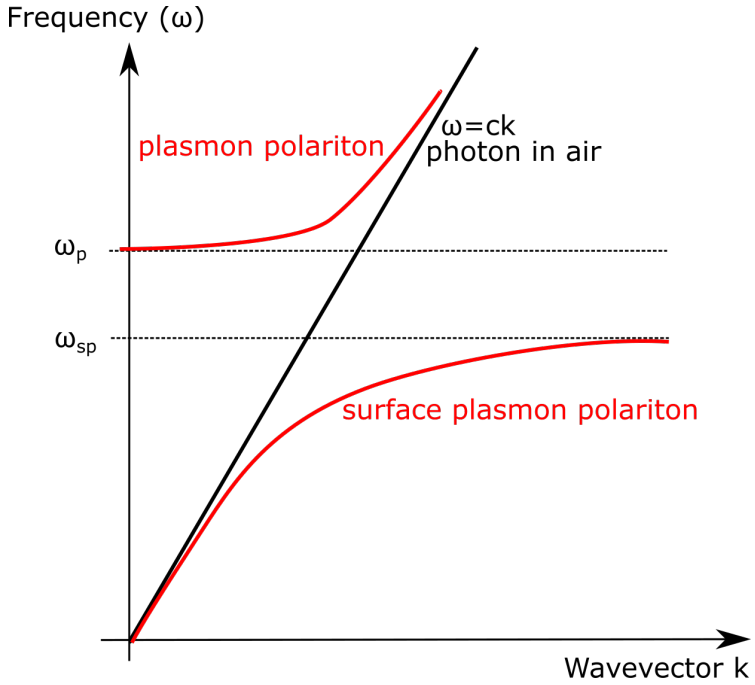

Figure 2.2: Schematic dispersion relationship of a surface plasmon polariton.

the air (or other dielectric). Major reviews of the theory of collective electronic excitations at metal surfaces have been given by Ritchie [18], Feibelman [19] and Liebsch [20]. It was shown that the SPP disperses away from the light line and assymptotes to $\omega_{sp} = \omega_p/\sqrt{2}$, where ω_p is plasma frequency, see Fig. 2.2. During the next two decades SPPs were extensively studied by many scientific groups [21–24].

In 2004 Pendry *et al.* drew parallels between "low frequency" surface waves on the corrugated metal-dielectric surface and SPPs at optical frequencies in his paper entitled "Mimicking Surface Plasmons with Structured Surfaces" [1]. They showed that the electromagnetic properties of a surface penetrated by a periodic array of sub-wavelength holes can be approximated by an effective plasmonic-like dielectric function. The modified effective dielectric permittivity function is then used to calculate surface wave confinement and dispersion. Akin to optical surface plasmons, the resulting mode disperses away from the light line and asymptotes to the cut-off frequency of an isolated sub-wavelength hole. The term "Spoof Surface Plasmon (SSP)" was coined for bound microwave

surface waves supported by corrugated metallic surfaces to highlight the similarity to SPPs at optical frequencies. Though it became very popular to use the term SSP we will stick to the conventional, more general and perhaps more accurate term "Surface Electromagnetic Wave".

The model proposed by Pendry was experimentally investigated by Hibbins *et al.* [25] using microwave reflectivity measurements. In this work the reflection of microwaves from a surface that was formed by a square array of hollow, square-shaped brass tubes placed on a brass plate was recorded. Diffractive coupling of the incident wave to the surface modes was achieved by placing an array of cylindrical brass rods on top of the brass tubes surface. The rods array period was two times the period of the tubes array. The SSP manifested itself as a dip in the frequency-dependent reflectance measurements. From the angle-resolved studies the authors could reproduce the second branch of the surface wave band structure in the first BZ which was also matched by numerical calculations.

Since then 2D metallic surfaces with holes of both infinite and finite depth have been studied theoretically and experimentally in the search for SEW [16, 26–33]. The most common considered design was a rectangular array of square-shaped penetrations – such a geometry simplifies the dispersion curve calculations. The other shapes investigated were circular holes in both the rectangular and triangular lattices [27, 34] and V-shape grooves [35–37].

One particular structure considered by Sievenpiper *et al.* [38] is a 2D array of so-called mushroom-like protrusions connected to the bottom ground plane, see Fig. 2.3. The protrusions are formed as metal patches on the top surface of the board, connected to the solid lower conducting surface by metal plated vias. This structure represents a class of corrugated surfaces with non-simply-shaped penetrations that supports TE SEWs. A finite element method was employed to obtain dispersion curves of the surface wave supported by this

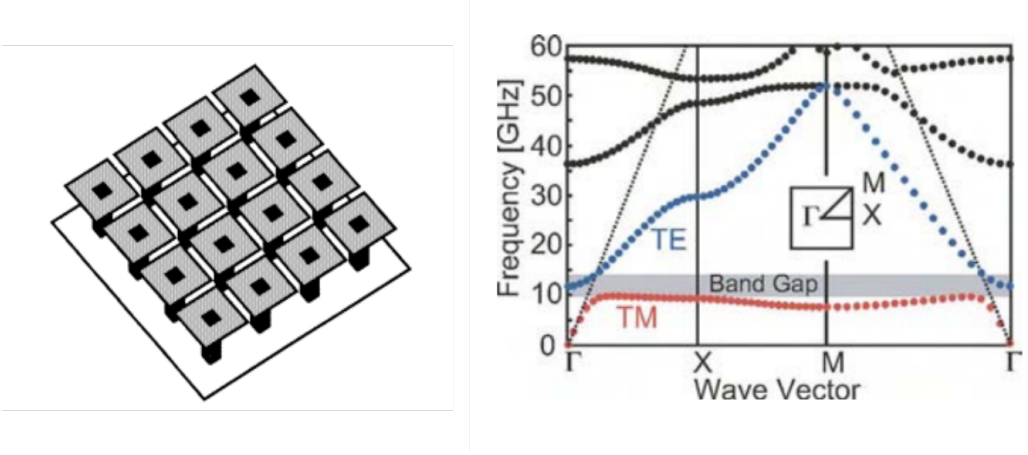

Figure 2.3: An example of a high impedance surface. The structure consists of a lattice of metal plates, connected to a solid metal sheet by vertical conducting vias. Dispersion of surface waves. Adopted from [39]

structure, see Fig. 2.3. A bottom TM branch first follows the dispersion of the free light and then suddenly becomes flat. The second TE polarised surface wave emerges at frequencies larger than that of the TM polarised branch, resulting in the formation of a full bandgap. These results were confirmed by experimental measurements performed by the authors. As we can see from the dispersion diagram (Fig. 2.3), the surface waves are highly localised (disperse far away from the light line), a result of the surface possessing high impedance. The concept of surface impedance will be described in Section 2.1.2.

High confinement of SEW along corrugated metal surfaces makes it possible to realise open waveguides: cylindrical waveguides [37, 41–44], channel waveguides [36, 45–48] or planar waveguides [49–52]. Other devices such as beam splitters, frequency selective devices, ulta-wideband and low loss filters, beam steerers can be also implemented using SEW [53–57]. SEW can also enhance transmission through a holey metallic surface due to field enhancement [58, 59], similarly to phenomena called Extraordinary Optical Transmission first reported by Ebbessen *et al.* [22]).

The concept of using SEW for antennas was initiated in the 1950s [60]. At that time materials used were heavy, bulky and costly, which limited their

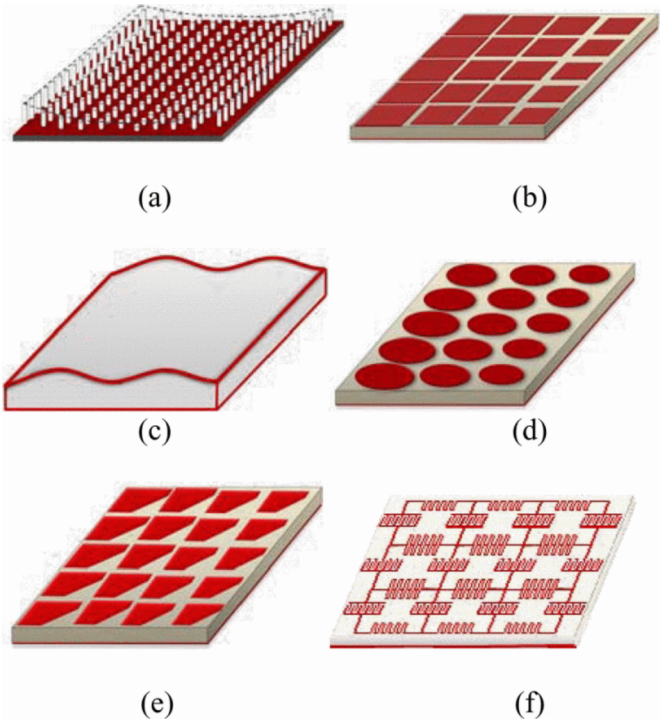

Figure 2.4: Possible solution for variable metasurfaces for leaky antennas at microwave frequencies: (a) pins with variable heights; (b) patch with variable sizes; (c) curved metallic or dielectric surface; (d) circular patches of variable sizes; (e) asymmetric patches with variable shapes (anisotropic surface impedance). (f) Transmission line based metasurface composed of microstrips loaded by inductance and capacitance. Adopted from [40].

application. However nowadays, advanced fabrication techniques make it possible to produce thin, lightweight materials with considerable design complexity. There is a class of materials with spatially variable impedance that are used for improving the performance of antennas, lenses and other optical devices. The propagating surface waves are being modified locally and transformed into a different configuration of wave function. This effect has the name "metasurfing". Fig. 2.4 shows some types of surface that can be used for metasurfing. The dimension of the elements and their variation should be small compared to the wavelength. The most common application of metasurfing include, Luneburg lens [61, 62], Maxwell's fish-eye [63], horn antennas [64]. Sinusoidal modulation of impedance can be used to create leaky-wave radiation [65] and was utilized to design antennas such as the ones described in the work by Maci's

group [66].

2.1.2 Derivation of Surface Wave Dispersion

SEW are EM waves which are localised near the boundary between two media and propagate along this interface. Their intensity reduces exponentially in the direction normal to the surface. Surface waves cannot exist on any surfaces, but require special conditions applied to the refractive indices of the media. Let us consider a monochromatic EM wave,

$$\begin{Bmatrix} \mathbf{E} \\ \mathbf{H} \end{Bmatrix} \propto \exp(-i\omega t), \tag{2.1}$$

at the interface of two non magnetic materials ($\mu_1 = \mu_2 = 1$) with the complex dielectric constants ε_1, ε_2. The x axis is oriented along the interface of two media, and the z axis is perpendicular to the interface pointing from media 2 to media 1 (see Fig. 2.5). Substituting Eq. (2.1) into Maxwell's equations gives

$$\nabla \times \mathbf{E} = -\frac{1}{c}\frac{\partial \mathbf{B}}{\partial t}, \quad \nabla \times \mathbf{H} = \frac{1}{c}\frac{\partial \mathbf{D}}{\partial t}, \tag{2.2}$$

and assuming for charge free media $\nabla \cdot \mathbf{E} = 0$, we obtain the standard equation for a monochromatic electromagnetic wave

$$\Delta \begin{Bmatrix} \mathbf{E} \\ \mathbf{H} \end{Bmatrix} + \varepsilon \frac{\omega^2}{c^2} \begin{Bmatrix} \mathbf{E} \\ \mathbf{H} \end{Bmatrix} = 0. \tag{2.3}$$

One of the solutions of this equation is a free-space wave for which **E** and **H** vectors are perpendicular to the wave vector **k**. However, there is another solution to this equation that corresponds to the SEW. Let us assume that solution is not dependent on the y coordinate and we will therefore search for a solution in the form

$$\begin{Bmatrix} \mathbf{E} \\ \mathbf{H} \end{Bmatrix} \propto \exp[i(k_x x - \omega t)], \tag{2.4}$$

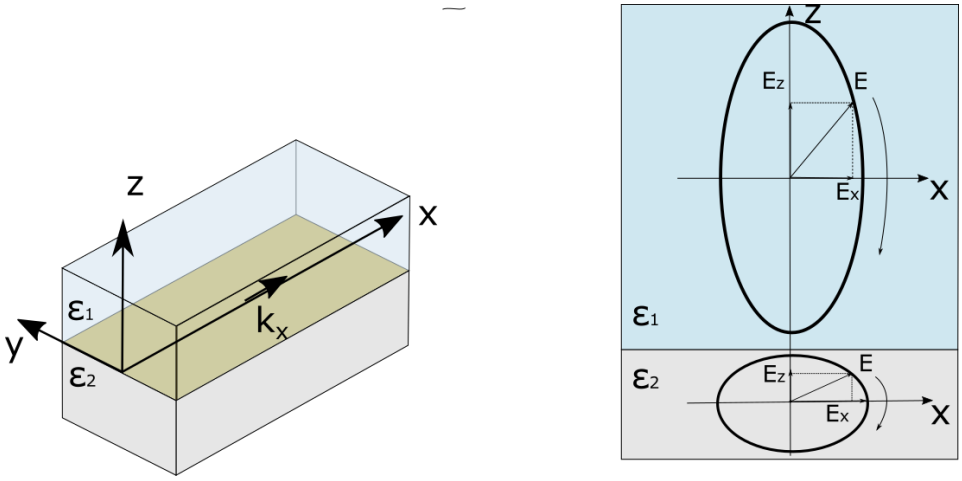

Figure 2.5: (Left) Sketch of the interface of two media and its coordinate system. (Right) Diagram of the electric field rotation in medium one and medium two.

Substituting Eq. (2.4) into Eq. (2.3) we obtain the following expression

$$\frac{\partial^2 \mathbf{E}}{\partial^2 z} - \left(k_x^2 - \varepsilon \frac{\omega^2}{c^2}\right)\mathbf{E} = 0. \tag{2.5}$$

The solution for the above equation has its electric field exponentially decaying along the z-axis

$$\mathbf{E} = \mathbf{E_0} \exp\left(-\kappa_{1,2}|z|\right) \exp(ik_x x - i\omega t), \tag{2.6}$$

where

$$\kappa_{1,2} = \left(k_x^2 - \varepsilon_{1,2} \frac{\omega^2}{c^2}\right)^{\frac{1}{2}}. \tag{2.7}$$

Vector components $\kappa_{1,2}$ are normal to k_x, the surface component of the wave vector. Wave vector component k_x must be the same in the two media.

Substituting the solution given by Eq. (2.6) into equation for $\nabla \times \mathbf{H}$ from Eq. (2.2) we obtain the following combination of equations

$$\begin{aligned} \frac{i\omega}{c}\varepsilon_{1,2} E_{x1,2} &= \mp \kappa_{1,2} H_{y1,2} \\ -\frac{i\omega}{c}\varepsilon_{1,2} E_{y1,2} &= 0 \\ -\frac{i\omega}{c}\varepsilon_{1,2} E_{z1,2} &= i k_x H_{y1,2} \end{aligned} \tag{2.8}$$

Taking into consideration boundary conditions $H_{y1} = H_{y2} \equiv H$, $E_{x1} = E_{x2} \equiv E_x$ we obtain the following for the x component:

$$\frac{i\omega}{c}\varepsilon_{1,2}E_x = \mp\kappa_{1,2}H. \tag{2.9}$$

The above solution is for a parallel-polarized wave, and may be classified as a transverse magnetic (TM) wave.

As stated above, $\mathbf{E}$ is exponentially decaying along the z-axis, which implies that $\mathrm{Re}(\kappa_{1,2}) > 0$ (see Eq. (2.6)). From Eq. (2.9) it follows that the dielectric constants of the two materials should satisfy the following relationship:

$$\frac{\varepsilon_1}{\varepsilon_2} = -\frac{\kappa_1}{\kappa_2}. \tag{2.10}$$

This condition means that for the surface wave existence it is necessary that the real part of the dielectric constant of the two materials are of a differing sign. One example when this condition is satisfied is a metal-dielectric interface for wave frequencies from microwave to optical. For the rest of the calculations we will assume that media 2 has negative dielectric constant. Substituting Eq. (2.10) in Eq. (2.7) we obtain

$$\begin{aligned} \kappa_1 &= \sqrt{-\frac{\varepsilon_1^2}{\varepsilon_1+\varepsilon_2}}\,k_0 \\ \kappa_2 &= \sqrt{-\frac{\varepsilon_2^2}{\varepsilon_1+\varepsilon_2}}\,k_0 \end{aligned}, \tag{2.11}$$

where $k_0 = \omega/c$ is wavevector in free space. It is clear that for Eq. (2.11) to be valid it is necessary that the dielectric constants satisfy condition below:

$$Re(\varepsilon_2) < 0 \quad and \quad |\varepsilon_2| > |\varepsilon_1|.$$

From Eq. (2.7) and Eq. (2.10) one can obtain the dispersion relationship for surface waves as below

$$k_s = n(\omega)\frac{\omega}{c}, \tag{2.12}$$

where

$$n(\omega) = \sqrt{\frac{\varepsilon_1 \varepsilon_2}{\varepsilon_1 + \varepsilon_2}} \tag{2.13}$$

is a complex refractive index for surface waves. Using Eq. (2.12) we can rewrite Eq. (2.11) in the following form

$$\begin{aligned} \kappa_1 &= \sqrt{-\frac{\varepsilon_1}{\varepsilon_2}}\, k_s \\ \kappa_2 &= \sqrt{-\frac{\varepsilon_2}{\varepsilon_1}}\, k_s \end{aligned} \tag{2.14}$$

From Eq. (2.8), using Eq. (2.14), we can derive components of the electric field at the interface of the two media

$$E_x = E_{x1} = E_{x2} = iH\sqrt{\frac{1}{-(\varepsilon_1 + \varepsilon_2)}}, \tag{2.15}$$

$$E_{z1} = -H\sqrt{\frac{\varepsilon_2}{\varepsilon_1}\frac{1}{(\varepsilon_1 + \varepsilon_2)}}, \tag{2.16}$$

$$E_{z2} = -H\sqrt{\frac{\varepsilon_1}{\varepsilon_2}\frac{1}{(\varepsilon_1 + \varepsilon_2)}}. \tag{2.17}$$

It can be seen that E_x phase is shifted by 90 degrees with respect to the H vector, and by 180 degrees to E_z. From Eq. (2.15) - Eq. (2.17) it can be seen that $|E_{z1}| > |E_x| > |E_{z2}|$. Therefore, if we fix the x coordinate as $x = X$, then vector E(X,t) is rotating clockwise in an elliptical shape in both media. In optically active media the ellipse will be flattened, and in media with positive ε it will be stretched (see Fig. 2.5).

A solution similar to the above for a perpendicular -polarised (transverse electric, TE) can not satisfy the boundary conditions and does not exist unless the two media have different permeabilities [67].

2.1.2.1 Characteristics of Surface Electromagnetic Waves

Once the surface wave equation is derived it is important to discuss other properties of SEW including penetration depth, amplitude of the wave in both

media, and propagation length. We will now study SEW on the metal-air interface.

To determine the properties it is necessary to know the frequency dependence of the dielectric constant. We use an analytical equation for ε for the metal obtained from Drude model [68], which well explains the transport properties in materials in microwave spectrum:

$$\varepsilon_c \approx 1 - \frac{\omega_p^2}{\omega^2 + \Gamma^2} + \frac{i\Gamma\omega_p^2}{\omega(\omega^2 + \Gamma^2)} \tag{2.18}$$

where ω_p is the plasma frequency and Γ is the frequency of electron collisions. Values of these constants for common metals are given in the below table

Metal	$\Gamma, 10^{13}$ 1/s	$\omega_p, 10^{16}$ s
Al	12.5	2.4
Cu	3.7	1.6
Ag	2.5	1.4

The propagation length at which the intensity of the electromagnetic surface wave propagating along the air-metal interface decays by a factor of e is given by $L = 1/(2\mathrm{Im}(k_x))$. The decay length dependence on the frequency for copper in air is plotted in Fig. 2.6. It can be seen that propagation length increases from tens of micrometers for $\lambda = 1$ μm to hundreds of meters for $\lambda = 1$ mm.

The decay distance of the electromagnetic field perpendicular to the metal surface at which the intensity falls to $1/e$ is referred as penetration depth. It is given by $\Delta = 1/[\mathrm{Re}(\kappa_1)]$ and is plotted in Fig. 2.7. One can see that in the microwave regime confinement of the mode is very poor. For $\lambda = 1$ mm $\Delta \approx 50$ cm (500 wavelengths). The dispersion of the mode at these frequencies coincides with the light line and is often referred to as a "surface current". In contrast for $\lambda = 1$ μm $\Delta \approx 1$ μm (1 wavelength). However, it is possible to more tightly confine SEW in microwave regime by corrugating the metal surface

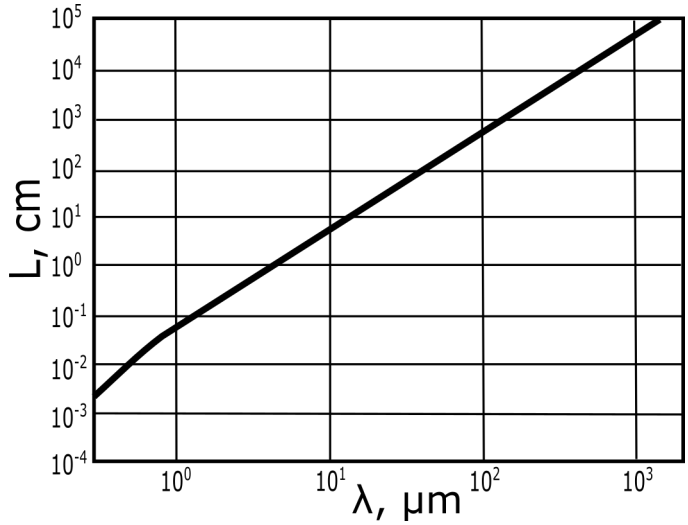

Figure 2.6: Propagation distance of the electromagnetic field along the metal (Cu)/air surface where intensity is reduced by a factor of e.

as mentioned earlier. Let us introduce a concept of the surface impedance to explain how patterning of the surface results in confinement of the SEW.

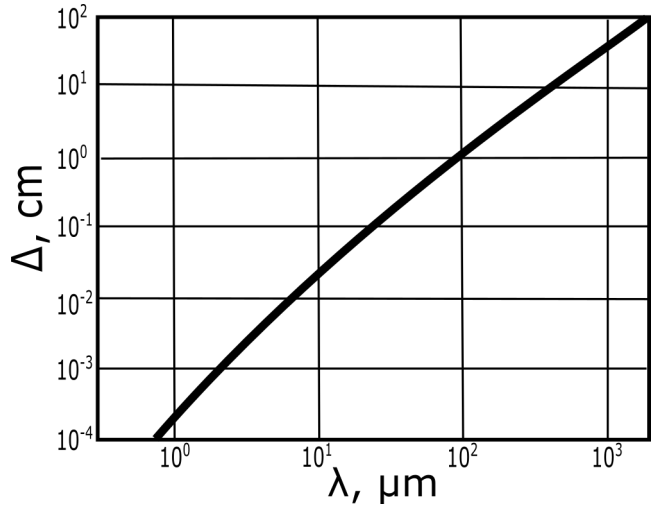

Figure 2.7: Penetration depth where the amplitude of the surface electromagnetic wave is attenuated e times for metal (Cu)- dielectric interface.

2.1.2.2 Surface Impedance

The surface impedance concept is, in fact, another approach that can be used to describe the interaction of electromagnetic waves with interfaces between different media. In 1930s Schelkunoff [69] proposed that impedance, earlier

introduced by Heaviside (1888) in the context of currents and voltages in Alternating Current (AC) circuits [70], can be generalised in the context of EM waves. Schelkunoff used the impedance concept to describe the ratio of the transverse electric field over the transverse magnetic field, since they depend solely on the host medium.

The absolute value of the metal dielectric constant is much larger than 1 before approaching plasma frequency. Under this condition the wavelength $\delta \approx c/\omega\sqrt{|\epsilon|}$ in the metal is small compared to the wavelength $\lambda \approx c/\omega$ in free space. The small value of δ means that derivatives of field components inside the metal normal to the surface are large compared to derivatives in the transverse direction. Thus, the electromagnetic field inside the metal in proximity to the surface can be considered as a plane wave, and, consequently, fields $\mathbf{E_t}$ and $\mathbf{H_t}$ are related to each other as

$$\mathbf{E_t} = \sqrt{\frac{\mu}{\varepsilon}}\mathbf{H_t} \times \mathbf{n}, \tag{2.19}$$

where $\mathbf{n}$ is normal to the surface directed towards metal. As can be seen, surface impedance in this case is defined as,

$$Z_s = \frac{|\mathbf{E_t}|}{|\mathbf{H_t}|} = \sqrt{\frac{\mu}{\varepsilon}}. \tag{2.20}$$

Surface impedance is a complex number $Z_s = Z' + iZ''$, where the real part is called resistance, and the imaginary part is called reactance. For highly conductive surfaces which include metals at microwave frequencies the surface impedance yields,

$$Z_s = \sqrt{\frac{\mu}{\varepsilon}} \approx \sqrt{\frac{i\omega\mu}{\sigma}}, \tag{2.21}$$

where ε and μ are the parameters of the conductor, σ is its conductivity, and we have neglected ε, as compared to σ/ω, it is small. The propagation in-plane wavevector number for a good conductor can be written as:

$$k_s^2 = k_0^2\left(1 + i\varepsilon\frac{\omega}{\sigma}\right). \tag{2.22}$$

Further approximation can be done as $\sigma/\omega \gg \varepsilon$, thus, $k_s \approx k_0$. This means that $\kappa^2 = k_s^2 - k_o^2 \approx 0$ and the wave is not confined to the surface. This further confirms the earlier derivations.

Let us now express k_s for TM and TE modes through the surface impedance for a general case. For TM surface waves, $H_x = H_z = E_y = 0$. The electromagnetic field decays in the z direction perpendicular to the surface with the decay constant κ and travels along the x direction with the wavevector k_s. The equation for the E_x component of the electromagnetic field in a general form reads as below (z>0):

$$E_x = C \cdot exp(-ik_s x - \kappa z). \tag{2.23}$$

H_y can be derived from Ampere's law, given three field components are equal to 0

$$i\omega\varepsilon E_x = \frac{\partial H_y}{\partial z}. \tag{2.24}$$

Substituting Eq. (2.23) into Eq. (2.24) results in the following expression for the y-component of the magnetic field

$$H_y = \frac{-i\omega\varepsilon}{\kappa} C \exp(-ik_s x - \kappa z). \tag{2.25}$$

For a TM - polarised electromagnetic wave the equation for the surface impedance is given by

$$Z_s = \frac{E_x}{H_y} \tag{2.26}$$

Substituting Eq. (2.23) and Eq. (2.25) into Eq. (2.20) results in the following relationship for surface impedance for TM modes

$$Z_s = \frac{i\kappa}{\omega\varepsilon}. \tag{2.27}$$

Performing similar calculations we also obtain surface impedance for TE modes as below

$$Z_s = \frac{-i\omega\mu}{\kappa}. \tag{2.28}$$

We can re-write the above equations in terms of the electromagnetic wave decay constant κ

$$\begin{array}{l} \kappa = -i\omega\varepsilon Z_s \quad \text{(TM waves)} \\ \kappa = -\dfrac{i\omega\mu}{Z_s} \quad \text{(TE waves)} \end{array}. \tag{2.29}$$

Since every field component should satisfy the Helmholtz equation, which reads as following

$$\left(\nabla^2 + k_0^2\right) E_x = 0 \tag{2.30}$$

we obtain

$$\kappa^2 - k_s^2 + k_0^2 = 0. \tag{2.31}$$

From the above equations we can derive the relationship for propagating constant k_s

$$\begin{array}{l} k_s = \sqrt{k_0^2\left(1 - \dfrac{Z_s^2}{\eta_0^2}\right)} \quad \text{(TM waves)} \\ k_s = \sqrt{k_0^2\left(1 - \dfrac{\eta_0^2}{Z_s^2}\right)} \quad \text{(TE waves)} \end{array}, \tag{2.32}$$

where $\eta = \sqrt{\mu_0/\varepsilon_0}$ is the impedance of free space and $k_0 = \omega/\sqrt{\mu_0\varepsilon_0}$ is the wave vector in free space. Propagating surface waves have a purely real propagation constant k_s as defined in Eq. (2.23). Naturally, it is only possible if the surface impedance has a purely imaginary value as follows from Eq. (2.32)). In turn, the decay factor κ is purely real (see Eq. (2.29)). As can be seen from Eq. (2.29), a surface with a positive reactance (an inductive surface impedance) is required

to support TM modes. For TE modes, a negative reactance is needed, i.e. a capacitive surface impedance. Clearly, the value of the surface impedance determines how strongly the field is confined to the surface.

A smooth conductor has low surface impedance, whereas introducing texture can result in increasing of the surface impedance. The recipe of creating high impedance surface is to position a capacitive grid (e.g., an array of small metal patches) above the metal sheet. The surface impedance of such structure is given as,

$$Z_s = \frac{i\omega\mu d}{1-\omega^2 C_g \mu d}, \tag{2.33}$$

where d is the thickness of the structure (distance between patches and the ground plane), μ is the magnetic permeability of the material between patches and ground plane, and C_g is capacitance of the grid [71]. At the resonant frequency $\omega_0 = \sqrt{1/C_g \mu d}$, the imaginary part of the surface impedance tends to infinity, and the system is effectively a magnetic wall. The most known high impedance structure is the so-called "mushroom" structure by Sievenpiper, reviewed earlier [38].

To summarise, SEW exist at the metal-dielectric interface for all frequencies. They are highly localised to the surface for the optical range of frequencies, but are delocalised for microwaves. To confine them to the surface one needs to increase the reactance of the metal surface by structuring it.

2.2 Photonic Crystals

A Photonic Crystal (PhC) is an media, often specifically fabricated, which mimics natural crystals for electromagnetic waves. The author prefers a more generalised term "electromagnetic crystal" that is sometimes used in the community as it indicates that these artificial structures can operate over a wide range of frequencies. However, the more common term "Photonic Crystal" (PhC) will be used throughout this work.

We start by reviewing some of very first PhCs designed and fabricated by Yablonovitch [72] and John [73] to operate at microwave frequencies to study quantum effects. We then proceed with highlights from the vast number of experimental studies reported up to the present date in this fascinating area. In the second part we show similarities between Schrödinger's equation that governs behaviour of electrons in solid state crystals with Maxwell's equations that govern electromagnetic wave propagation in periodic media. We also provide explanation of the Photonic Band Gap (PBG) that is naturally occurring in periodic structures.

2.2.1 Historical Overview

PhC is a media that is comprised of elements with differing optical constants that are arranged in a regular lattice, very much like natural crystals. Depending on the number of dimensions in which the optical the constant is varying one can distinguish One-Dimensional (1D), Two-Dimensional (2D), or even Three-Dimensional (3D) PhCs, see Fig. 2.8. As a result of this periodicity, there are forbidden zones in the frequency spectrum where for some or even all directions no waves can propagate inside the material. Almost all practical applications of PhCs arise from the existence of this forbidden zone, called Photonic Band Gap (PBG).

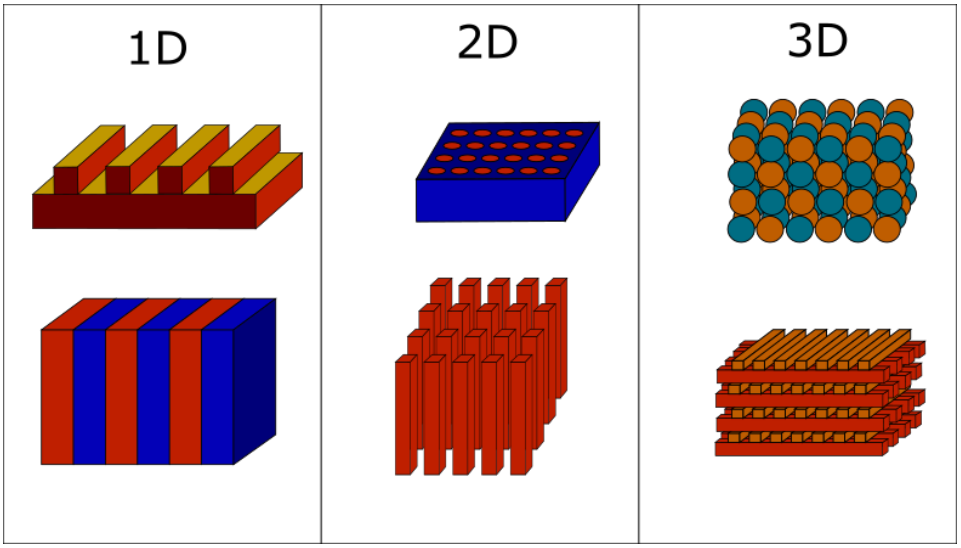

Figure 2.8: Examples of one-, two-, and three- dimensional photonic crystals.

Microwave PhCs are important as they can be used as a tool for designing photonic crystals that operate over the visible light spectrum. This is possible because of the scalability of Maxwell's equations. PhCs operating in the infrared and visible regions of the wave spectrum are more difficult and expensive to fabricate due to their micro- and nano-scale nature. By engineering a mimicking microwave structure first, it is possible to significantly reduce a photonic crystals production cost.

Two pioneering scientists discovered and promoted the exciting world of photonic crystal in 1987, namely Yablonovitch [72] and John [73]. They studied structures with periodically varying dielectric constant. It was shown that propagation of electromagnetic waves in such media is affected by scattering on the lattice surfaces in the same way as for electron waves propagating in solid-state crystals.

In 1991 Yablonovich demonstrated the first three-dimensional PhC structure, known now as Yablonovite [74], developed in an effort to achieve a complete PBG to control spontaneous emission of materials placed inside the PhC. It was fabricated by drilling an array of holes inside a dielectric material in a way that the holes in each cross-section of the slab are arranged in the inverse

diamond lattice, see Fig. 2.9. In a later work Yablonovitch *et al.* managed to modify the radiation profile of a bow-tie microwave antenna by placing the antenna on top of a face-centered cubic PhC possessing a bandgap [75]. The crystal substrate blocked a significant part of the radiation in the substrate direction at the bandgap frequencies.

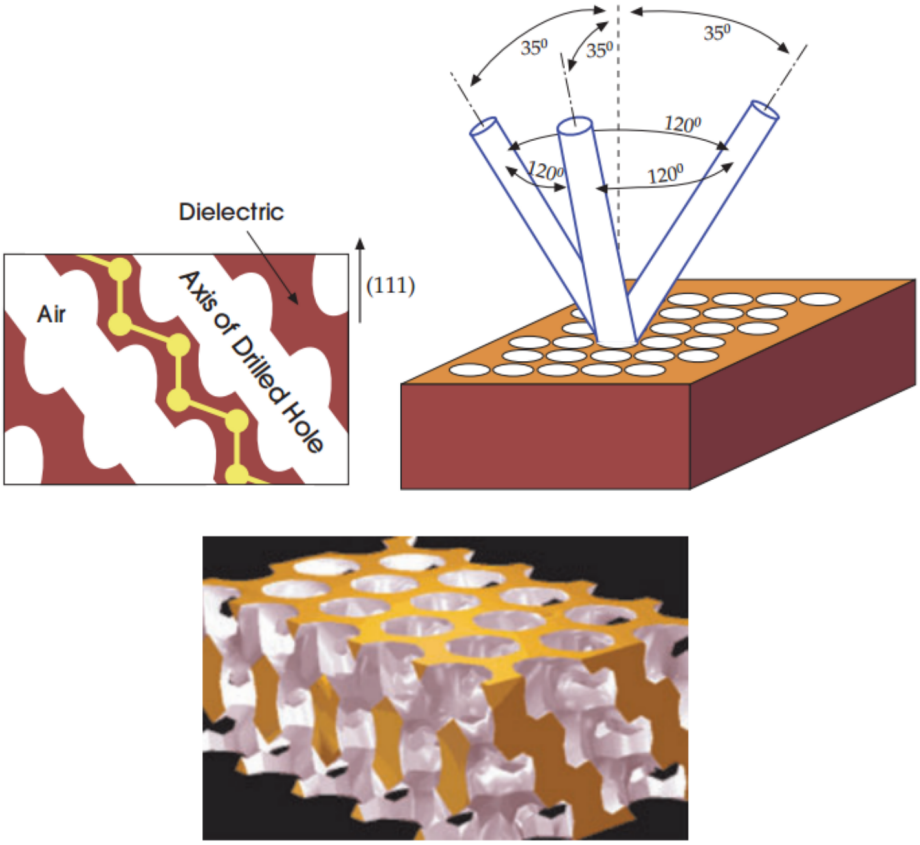

Figure 2.9: Yablonovite Photonic Crystal. (Right) Triangular array of holes is drilled three times, at an angle of 35.26° away from the normal and spread out 120° on the azimuth. (Left) $(1\bar{1}0)$ cross section . The dielectric connects the sites of a diamond lattice, shown schematically in yellow. The dielectric veins oriented vertically $[1\bar{1}1]$ have greater width than those oriented diagonally $[11\bar{1}]$. (Bottom) Computer rendering of the structure. Adopted from [76].

John meanwhile was interested in using PhCs to control Anderson localisation of photons [77]. He showed a new mechanism for strong Anderson localization in carefully prepared disordered dielectric PhCs. These structures were, in fact, a photonic analogue of amorphous semiconductors.

A different type of three dimensional crystal, a metallic wire mesh, was

shown to have an extra PBG commencing at zero frequency, acting like a waveguide cut-off frequency [78]. The "effective media limit" of the PhC, defined as a range of operating wavelengths that are much larger than the crystal periodicity constant, was introduced, probably, for the first time. The authors discussed possible applications of the "effective media regime" paving the way for the metamaterials concept, although, there were some years to come before the term "metamaterial" was introduced. Another diamond-like metallic microwave crystal was investigated in the paper by Fan *et al.* [79]. The three-dimensional electromagnetic crystal comprised of isolated metal spheres was reported to possess bandgaps larger than in dielectric crystals of similar structure.

Microwave PhCs are also important in their own right due to possible applications in the communication and radio location sectors. One of the possible application of PhCs with a full band gap is waveguiding. If a linear channel is created in the crystal structure it can act as a waveguide for the allowed "defective" modes with the crystal bandgap prohibiting wave propagation inside the media (Fig. 2.10). In one of the first papers Lin *et al.* demonstrated steering of the microwaves around sharp 90° corners with nearly 100% efficiency [80]. An interesting design of 2D PhC waveguide was suggested by Falcone *et al.* [81]. In this work a periodic array of air disks was created by drilling holes in a planar printed-circuit board. The structure was then confined between two metal plates forming an electromagnetic cavity and the waveguide was created inside this microwave crystal by introducing a linear defect.

The complementary system to the waveguide, an electromagnetic cavity, can also be realised within the PhC concept. One missing element from the crystalline structure results in the appearance of "defect modes" that are trapped between the nearest neighbours. In the work by Coves *et al.* [82] PhCs comprised of square and circular elements were designed to have only

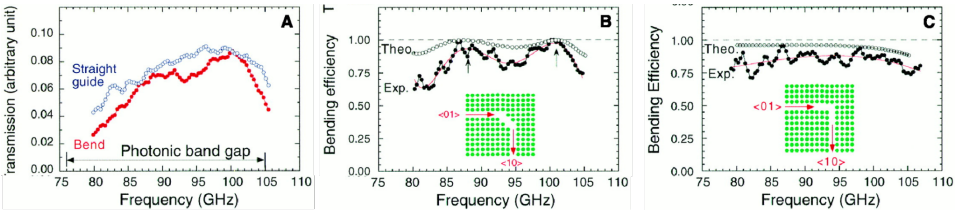

Figure 2.10: (A) Transmission spectra for a straight waveguide and a waveguide bend in a 2D photonic crystal. (B) Bending efficiency as a function of frequency. Near perfect bending efficiency is observed around 87 and 101 GHz. The PBG bending geometry is shown in the inset. (C) Bending efficiency of a PBG waveguide bend with zero radius of curvature. The PBG bending geometry is shown in the inset. Adopted from [80].

one cavity mode at an arbitrary frequency in a given range. Possible effects include modification of optical modes density [72], enhancement of linear and non-linear optical effects, for example, generation of second and third optical harmonics [83], Faraday effect [84], and others.

It is possible to engineer PhCs with the response needed for various applications. By controlling wave behaviour on demand, it is possible to create advanced photonic devices, such as filters [85], photonic switches [86], photonic crystal lasers [87], etc. The reader is referred to the reference [88] in which K. Inoue *et al.* summarized application of PhCs.

To complete this overview we would like to discuss fabrication methods of PhCs. Microwave PhCs received their popularity partially because they are easier to fabricate compared to the periodic nano-structures that operate at visible wavelengths. The very first microwave crystals were fabricated using drilling, milling, and layering of a bulk dielectric or metallic slabs, techniques that are still widely used. These methods are simple, cheap, and widely available. Drilling of holes or milling of the slab can be done using automated machinery called Computer Numerical Control (CNC). Such equipment can create simple structures following pre-loaded CAD patterns, but is generally limited to 1D and 2D structures. More complex structures require advanced fabrication techniques, such as two-photon polymerization [89], holographic

lithography [90], or rapidly evolving additive manufacturing, e.g. 3D printing [91].

2.2.2 Derivation of the Master Equation

As stated above PhCs are comprised of elements with differing optical constants that are arranged in a regular lattice, very much like natural crystals. The distance between neighbouring elements is of the order of the PhC operating wavelength. Electromagnetic waves propagating through such media experience Bragg scatterings on the lattice surfaces that defines the dispersion of the modes supported, i.e. allowed Bloch modes. By using Maxwell's equation in combination with the Bloch theorem it is possible to calculate the dispersion of the PhC eigenmodes. Numerical implementations of the eigenmodes calculations can be performed by employing various methods, including, e.g., the finite-difference method, the transfer matrix method, and the mode-matching method [92–94]. These methods are of great help for calculating band structure of large, complex PhC and designing photonic devices with a pre-defined functionality, but can mask underlying physics. For illustrative purposes we present analytical derivation of the band structure of a simple PhC with dielectric permittivity periodically varying in one direction only.

The Schrödinger equation of quantum mechanics that governs electron eigenstates in a solid-state crystal is given below

$$\nabla^2 \Psi(\mathbf{r}) = -\frac{2m}{\hbar^2}\left(E - V(\mathbf{r})\right)\Psi(\mathbf{r}), \tag{2.34}$$

where $\Psi(\mathbf{r})$ is the electron wave function, m is the electron mass, $\hbar$ is the reduced Plank constant, E is the electron energy, and $V(\mathbf{r})$ is the periodic potentials of the crystal lattice. Propagation of electromagnetic waves in a

non-conductive medium is governed by Maxwell's equations which read as

$$\begin{aligned} \nabla \cdot \mathbf{B} = 0, \quad \nabla \times \mathbf{E} + \frac{1}{c}\frac{\partial \mathbf{B}}{\partial t} = 0, \\ \nabla \cdot \mathbf{D} = 4\pi\rho, \quad \nabla \times \mathbf{H} - \frac{1}{c}\frac{\partial \mathbf{D}}{\partial t} = \frac{4\pi}{c}\mathbf{J}, \end{aligned} \tag{2.35}$$

where $\mathbf{E}$ and $\mathbf{H}$ are electric and magnetic fields, $\mathbf{D}$ and $\mathbf{B}$ are displacement electric and magnetic induction fields, ρ and $\mathbf{J}$ are the free charge and current densities. We will restrict ourselves to propagation within a homogeneous dielectric medium and therefore can set $\rho = 0$ and $\mathbf{J} = 0$. Next we will assume linear regime, taking the material to be macroscopic, isotropic and transparent. In this case, the below is true

$$\begin{aligned} \mathbf{D}(\mathbf{r}) = \varepsilon(\mathbf{r})\mathbf{E}(\mathbf{r}), \\ \mathbf{B}(\mathbf{r}) = \mu(\mathbf{r})\mathbf{H}(\mathbf{r}), \end{aligned} \tag{2.36}$$

where the relative permittivity $\varepsilon(\mathbf{r})$ is real and positive and the relative magnetic permeability $\mu(\mathbf{r})$ can be taken as unity for simplicity.

Taking into account all these assumptions, Maxwell's equations (Eq. (2.35)) can be written as

$$\begin{aligned} \nabla \cdot \mathbf{H}(\mathbf{r},t) = 0, \quad \nabla \times \mathbf{E}(\mathbf{r},t) + \frac{1}{c}\frac{\partial \mathbf{H}(\mathbf{r},t)}{\partial t} = 0, \\ \nabla \cdot \varepsilon(\mathbf{r})\mathbf{E}(\mathbf{r},t) = 0, \quad \nabla \times \mathbf{H}(\mathbf{r},t) - \frac{\varepsilon(\mathbf{r})}{c}\frac{\partial \mathbf{E}(\mathbf{r},t)}{\partial t} = 0. \end{aligned} \tag{2.37}$$

Let us assume that $\mathbf{E}$ and $\mathbf{H}$ can be presented in the following form with separated time dependency

$$\begin{aligned} \mathbf{H}(\mathbf{r},t) = \mathbf{H}(\mathbf{r})\exp(-i\omega t) \\ \mathbf{E}(\mathbf{r},t) = \mathbf{E}(\mathbf{r})\exp(-i\omega t). \end{aligned} \tag{2.38}$$

Substituting Eq. (2.38) into Eq. (2.37) we obtain the following form of the governing equations

$$\begin{aligned} \nabla \times \mathbf{E}(\mathbf{r}) - \frac{i\omega}{c}\mathbf{H}(\mathbf{r}) = 0 \\ \nabla \times \mathbf{H}(\mathbf{r}) + \frac{i\omega\varepsilon(\mathbf{r})}{c}\mathbf{E}(\mathbf{r}) = 0 \end{aligned} \tag{2.39}$$

If we decouple the above equations by dividing the second equation by $\varepsilon(\mathbf{r})$ and taking curl we then obtain a master equation similar to the Schrödinger equation (Eq. (2.34))

$$\nabla \times \left(\frac{1}{\varepsilon(\mathbf{r})} \nabla \times \mathbf{H}(\mathbf{r}) \right) = \left(\frac{\omega}{c} \right)^2 \mathbf{H}(\mathbf{r}). \tag{2.40}$$

This is an eigenvalue equation, with eigenvalue $\left(\frac{\omega}{c}\right)^2$ and an eigen-operator $\nabla \times \frac{1}{\varepsilon(\mathbf{r})} \nabla \times$. We now consider a medium with periodic dielectric function $\varepsilon(\mathbf{r}) = \varepsilon(\mathbf{r} + \mathbf{R_i})$ for some primitive lattice vectors R_i ($i = 1,2,3$ for 3D PhC). According to the Bloch-Floquet theorem the solution can be searched for in the form of $\mathbf{H}(\mathbf{r}) = \exp(i\mathbf{kr})\mathbf{H}_{n,\mathbf{k}}(\mathbf{r})$ where $\mathbf{H}_{n,\mathbf{k}}$ is a periodic envelope function satisfying the following equation

$$(\nabla + i\mathbf{k}) \times \frac{1}{\varepsilon} (\nabla + i\mathbf{k}) \times \mathbf{H}_{n,\mathbf{k}} = \left(\frac{\omega_n(\mathbf{k})}{c} \right)^2 \mathbf{H}_{n,\mathbf{k}} \tag{2.41}$$

The eigenvalues $\omega_n(\mathbf{k})$ are continuous functions of $\mathbf{k}$. Plotting of ω_n against $\mathbf{k}$ maps out all possible modes in the system, giving the band structure. Moreover, $\omega_n(\mathbf{k})$ is a periodic function of $\mathbf{k}$, where $\mathbf{k} = \mathbf{k} + \mathbf{G_j}$ with $\mathbf{G_j}$ being a primitive reciprocal vector defined by $\mathbf{R}_i * \mathbf{G}_j = 2\pi\delta_{i,j}$. This means that the eigen problem needs to be solved within a primitive reciprocal cell only, called the first Brillouin Zone (BZ).

Let us now explore the effects of periodicity on the band structure using a 1D example where $R_1 = a$ and $G_1 = 2\pi/a$. The first BZ is defined as the region where $k = [-\pi/a; \pi/a]$. All other wavevectors have an equivalent point in the first BZ. We define the dielectric constant ε as ε_1 for $x = [0; a/2]$ and ε_2 for $x = [a/2, a]$, but for the time being consider $\varepsilon_1 = \varepsilon_2$. Let us then derive the dispersion relationship for a plane wave in free space ($\omega(k) = ck$) experiencing such an "artificial" periodic media. The dispersion is defined for k within the first BZ, waves with $|k| > \pi/a$ are translated ("folded") into the first BZ (Fig. 2.11b) causing degeneracy at $|k| = \pi/a$. Electric fields at $|k| = \pi/a$ can be written

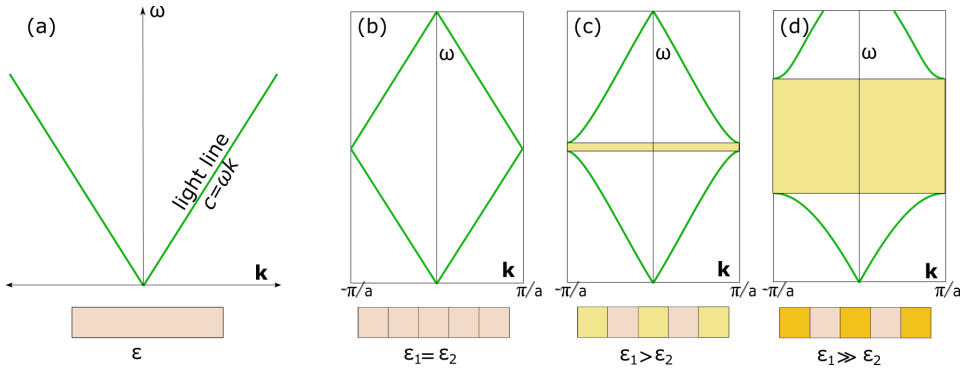

Figure 2.11: Dispersion relation for a free-space wave propagating in (a) uniform medium with the dielectric constant ε; (b) medium with artificial periodicity $\varepsilon_1 = \varepsilon_2 = \varepsilon$; (c) periodic medium with a smaller difference between varying dielectric constants $\varepsilon_1 > \varepsilon_2$; (d) periodic medium with a large difference between varying dielectric constants $\varepsilon_1 >> \varepsilon_2$.

as $\mathbf{E} \propto \exp(\pm i\pi x/a)$, or as a set of linear combination of $E_1(x) = \cos(\pi x/a)$ and $E_2(x) = \sin(\pi x/a)$. The accidental degeneracy is caused by "artificial" periodicity. However, if we apply variation to the dielectric function assuming $\varepsilon_1 > \varepsilon_2$, then the field $E_1(x)$ is concentrated in the higher-ε region ε_1, and possesses a lower frequency than $E_2(x)$. This results in the gap at $k = \pi/a$ (Fig. 2.11c). The bigger the difference between the dielectric constants ε_1 and ε_2 the bigger is the band gap (Fig. 2.11d).

2.3 Graphene and its Artificial Analogues

The majority of PhC features PBG in their dispersion, however there is a class of PhC inspired by Graphene, that have gapless dispersion. Graphene, a single layer of carbon atoms arranged in a honeycomb lattice, has created a profound impact on modern condensed-matter science and technology [95, 96]. It is a semimetal with linearly dispersing conduction and valence bands touching each other at so-called Dirac points. In the vicinity of the Dirac points electrons behave like relativistic elementary particles with zero rest mass, a unique phenomenon not previously observed in any other solid state system. From the theoretical point of view, Dirac conical singularities can be engineered in other 2D lattices, but may require fine tuning of the system parameters. However in lattices with triangular symmetry (e.g. honeycomb lattice) they occur naturally at the edges of the Brillouin Zone (BZ). Discovered first, graphene established a natural foundation for studying Dirac fermions and symmetry effects.

To be able to better relate dispersion of the Artificial Graphene (AG) studied in the rest of this thesis it is useful to re-visit the original derivation of the well celebrated Dirac cones in graphene using tight-binding theory.

2.3.1 Derivation of the Graphene Band Structure

Graphene structural properties are determined by strong σ bonds formed by the electrons occupying in-plane $2s$, $2p_x$ and $2p_y$ orbitals. The out-of-plane $2p_z$ orbitals, occupied by one electron, hybridise, form weak π bonds, and define the low-energy electronic structure of graphene.

Graphene's lattice can be seen as two overlapping triangular sub-lattices with inequivalent atoms, A and B (Fig. 2.12). This means that atoms A and B cannot be mapped one onto another by a lattice vector. There are two primitive

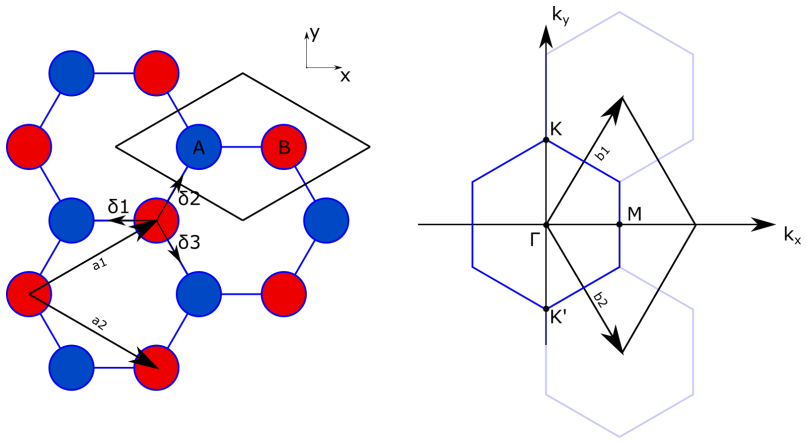

Figure 2.12: (Left) Crystal lattice of graphene in real space possesses a rhombic unit cell with A and B atoms. The primitive translation vectors $\mathbf{a_1}$ and $\mathbf{a_2}$ as well as nearest-neighbor vectors δ_1, δ_2 and δ_3 are shown. (Right) First BZ of graphene with high symmetry points Γ, M, K and K′ indicated, b_1 and b_2 are reciprocal lattice vectors.

lattice vectors defined as

$$\boldsymbol{a}_1 = \frac{a}{2}\left(3, \sqrt{3}\right), \qquad \boldsymbol{a}_2 = \frac{a}{2}\left(3, -\sqrt{3}\right), \tag{2.42}$$

where a = 0.124 nm is the distance between two neighbouring carbon atoms, $|\mathbf{a_1}| = |\mathbf{a_2}| = a\sqrt{3}$. The corresponding reciprocal lattice vectors are given by

$$\mathbf{b_1} = \left(\frac{2\pi}{\sqrt{3}a}, \frac{2\pi}{a}\right), \quad \mathbf{b_2} = \left(\frac{2\pi}{\sqrt{3}a}, -\frac{2\pi}{a}\right). \tag{2.43}$$

Fig. 2.12 shows the hexagonal BZ with the reciprocal lattice vectors depicted. The high symmetry points are defined as

$$\Gamma = (0,0), \quad K = \left(0, \frac{4\pi}{3\sqrt{3}a}\right), \quad K' = \left(0, -\frac{4\pi}{3\sqrt{3}a}\right), \quad M = \left(\frac{2\pi}{3a}, 0\right). \tag{2.44}$$

The nearest-neighbour vectors are given by the following expressions

$$\boldsymbol{\delta}_1 = -a\begin{pmatrix} -1 \\ 0 \end{pmatrix}, \quad \boldsymbol{\delta}_2 = a\begin{pmatrix} \frac{1}{2} \\ \frac{\sqrt{3}}{2} \end{pmatrix}, \quad \boldsymbol{\delta}_3 = a\begin{pmatrix} \frac{1}{2} \\ \frac{-\sqrt{3}}{2} \end{pmatrix}. \tag{2.45}$$

The electronic band structure of graphene can be calculated using the Tight-Binding (TB) approximation [97]. In this approximation electrons are considered strongly bound to the atoms, and therefore can only hop between

nearest neighbours. Graphene's electronic wavefunction, Ψ, is a linear combination of two individual Bloch functions corresponding to the two inequivalent sub-lattices

$$\Psi(\mathbf{k},\mathbf{r}) = \sum_j C_j(\mathbf{k})\psi_j(\mathbf{k},\mathbf{r}), \quad j = \mathrm{A},\mathrm{B} \tag{2.46}$$

where C_j are coefficients to be determined and j denotes A and B sub-lattices. The tight binding Bloch functions are given by

$$\psi_j = \frac{1}{\sqrt{N}} \sum_{\boldsymbol{R}_j} e^{i\boldsymbol{k}\boldsymbol{R}_j} \phi(\boldsymbol{r} - \boldsymbol{R}_j), \quad j = \mathrm{A},\mathrm{B}, \tag{2.47}$$

where $\mathbf{R}_j = n_j\mathbf{a}_1 + m_j\mathbf{a}_2$ is the translation vector and summation is taken over N atoms in the corresponding sublattice. Substituting the wavefunction given by Eq. (2.47) into the Schrödinger equation $\hat{H}\Psi = E\Psi$ and multiplying it by $\langle\psi_A|$ and $\langle\psi_B|$, we obtain two linear equations for coefficients C_j

$$\begin{aligned} C_A\left\langle\psi_A\middle|\hat{H}\middle|\psi_A\right\rangle + C_B\left\langle\psi_A\middle|\hat{H}\middle|\psi_B\right\rangle &= E\left(C_A\left\langle\psi_A\middle|\psi_A\right\rangle + C_B\left\langle\psi_A\middle|\psi_B\right\rangle\right), \\ C_A\left\langle\psi_B\middle|\hat{H}\middle|\psi_A\right\rangle + C_B\left\langle\psi_B\middle|\hat{H}\middle|\psi_B\right\rangle &= E\left(C_A\left\langle\psi_B\middle|\psi_A\right\rangle + C_B\left\langle\psi_B\middle|\psi_B\right\rangle\right). \end{aligned} \tag{2.48}$$

The term $\langle\psi_A|\psi_B\rangle$ can be neglected due to the exponentially decaying nature of the atomic wavefunctions. $\left\langle\psi_A\middle|\psi_A\right\rangle = \left\langle\psi_B\middle|\psi_B\right\rangle$ can be normalised and considered equal to unity. Taking the above consideration Eq. (2.48) can be simplified as

$$\begin{aligned} C_A H_{AA} + C_B H_{AB} &= EC_A \\ C_A H_{BA} + C_B H_{BB} &= EC_B, \end{aligned} \tag{2.49}$$

where $H_{ij} = \left\langle\psi_i\middle|\hat{H}\middle|\psi_j\right\rangle$. The energy spectrum of graphene can be obtained using the secular equation

$$\begin{vmatrix} H_{AA} - E & H_{AB} \\ H_{BA} & H_{BB} - E \end{vmatrix} = 0. \tag{2.50}$$

$H_{AA} = H_{BB}$ as carbon atoms are identical on the two sublattices. The solution for Eq. (2.50) is

$$E = H_{AA} \pm |H_{AB}|. \tag{2.51}$$

Using Bloch's functions defined by Eq. (2.47) we can calculate the band structure of graphene. The resulting electron energy is given by the below expression

$$E = E_0 \pm t\sqrt{1 + 4\cos\frac{\sqrt{3}k_y a}{2}\cos\frac{3k_x a}{2} + 4\cos^2\frac{\sqrt{3}k_y a}{2}}, \tag{2.52}$$

where $E_0 = \left\langle \phi(\mathbf{r}-\mathbf{R}_A)\middle|\hat{H}\middle|\phi(\mathbf{r}-\mathbf{R}_A)\right\rangle$ and $t = \left\langle \phi(\mathbf{r}-\mathbf{R}_A)\middle|\hat{H}\middle|\phi(\mathbf{r}-\mathbf{R}_B)\right\rangle$ is called hopping terms between the two atoms. The positive sign in the resulting equation corresponds to the electrons in the conduction band and negative sign corresponds to the valance band. It can be seen that the energy is symmetric with respect to E_0 and for convenience the energy spectrum is often shifted to zero.

The calculated electron dispersion is plotted in Fig. 2.13. As can be seen at $E = 0$, the diagram has six touching points at the edges of the BZ. In the vicinity of K points the dispersion is linear, thus electrons behave as massless Dirac particles. The slope of the linear dispersion is defined by the Fermi velocity and for graphene equals $v_F = 1 \cdot 10^6$ ms^{-1}.

Equi-energy plot on the middle bottom plot in Fig. 2.13 reveals circular contours in the vicinity of K points that evolve into triangular contours away from K points. This phenomena received the name "trigonal warping".

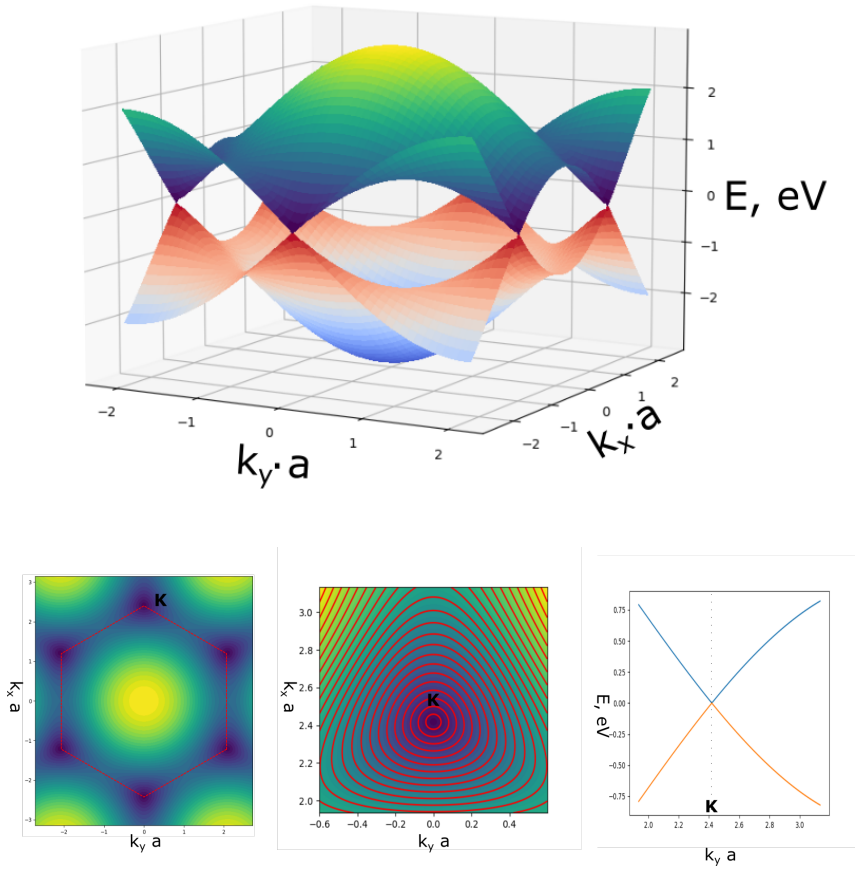

Figure 2.13: (Top) Band structure of graphene calculated using the tight-binding approximation for the nearest-neighbour hopping. (Bottom) From left to right: equi-energy contours for the conduction band. Red hexagon shows boundaries of the first BZ. Zoomed view of equi-energy contours around K point. Red lines guide iso-contours. In the vicinity of K points contours are of a circular shape, then gradually evolve into a triangular shape. Cross-section of the band structure in the vicinity of the K point showing linear dispersion.

2.3.2 Historical Overview

The unique properties of graphene which arise from its crystal structure stimulated a number of researchers to design and fabricate "quantum simulators" to study graphene physics. The term Artificial Graphene (AG) emerged to identify a class of purposely created materials with underlying triangular symmetry. Electronic AG is a straight analogy to the real graphene, however, other types of AG systems, photonic and even acoustic, attracted equal interest of the research communities. In AG interaction between artificial atoms can

be controlled by the shape of particles, material they are made of, their size, density, and distance to the nearest neighbours. The properties of AG systems can also be manipulated by applying external forces resulting in continuous change from weak to strong inter-particle interactions. This not only allows one to better explore the physics of graphene, but also gives a beneficial control over the parameters that are not accessible in natural graphene.

In this brief review we focus on photonic AG, more specifically, operating in the microwave regime. Should the reader wish to learn about other types of AG systems, a good review can be found in reference [98].

Long before the topic and the term AG became popular Maradudin calculated dispersion of the system comprised of dielectric rods of a circular cross-section arranged in an hexagonal array [99]. The rods were embedded in a host medium with a different dielectric constant. The electromagnetic waves were assumed to propagate within a plane perpendicular to the rods; two polarisations of the waves were considered. The authors were interested in the full PBG and its dependence on the ratio of the dielectric constant of the rods to the background dielectric constant and on the fraction of the total volume occupied by the rods. Dirac crossings were observed in different bands of the system depending on the wave polarisation and the above described parameters. If the rods' dielectric constant is bigger than the dielectric constant of the background, the Dirac crossing occurs between the second and third mode for both polarisations. If the rods' dielectric constant is smaller than the dielectric constant of the background, the Dirac crossing occurs for the first and second modes for E- (the electric vector parallel to the rods) polarisation and for the second and third modes for H-polarisation (the magnetic vector parallel to the rods). More details can be found in reference [99]. In 1991 no one believed that graphene (2D graphite) could be isolated, and thus, structures studied by Maradudin were not considered to have any practical application.

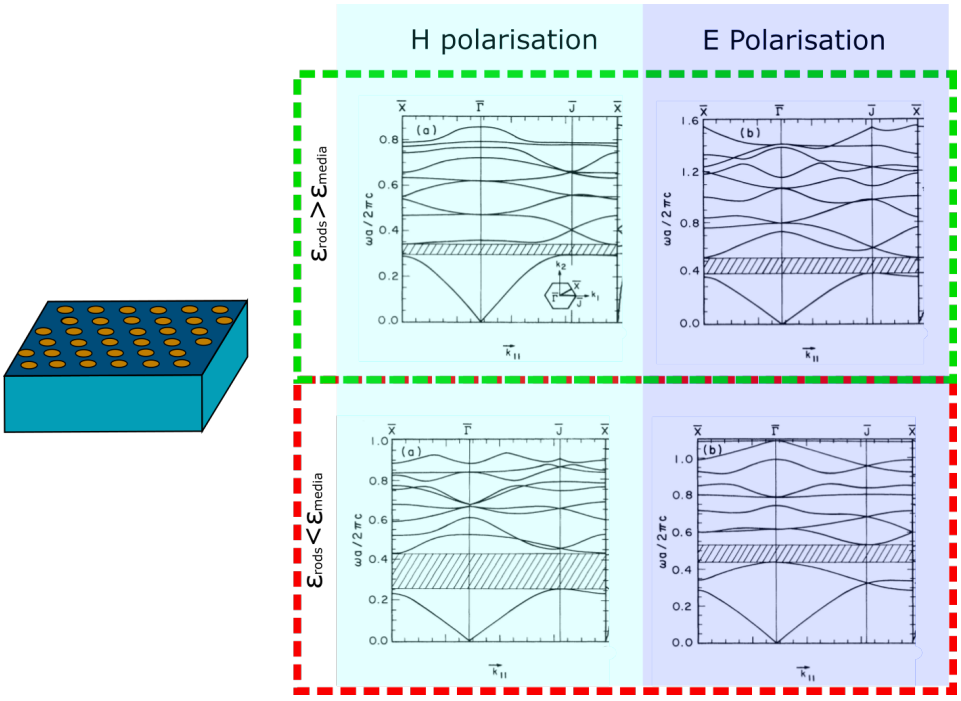

Figure 2.14: (Left) Sketch of the structure consisting of parallel dielectric rods arranged in triangular array embedded in a dielectric slab. (Right) Its photonic band structure. Columns show E- and H- polarisation cases. Rows show dielectric permitivity relationship between rods and surrounding media.

The first time when an artificial system was compared to real graphene was in the paper by Bittner *et al.* [100]. In this work the crystal was comprised of metallic cylinders with radius r= 5 mm and height h = 8 mm arranged in a triangular lattice, see Fig. 2.15. The authors numerically calculate the dispersion diagram and showed the existence of Dirac points at the corners of the BZ. The sample was placed between two metal plates. The reflection spectra showed a cusp feature corresponding to the calculated Dirac frequency in the band structure of the crystal, as shown in Fig. 2.15b. Further studies have been carried out demonstrating that transmission has a pseudo-diffusive $1/L$ dependence, with L being the thickness of the crystal, a phenomenon also observed in graphene [101].

Another AG was assembled out of dielectric resonators having a high-index of refraction [102–104]. Disks were placed in a metallic cavity, such that the coupling between the disks in the air happens through evanescent

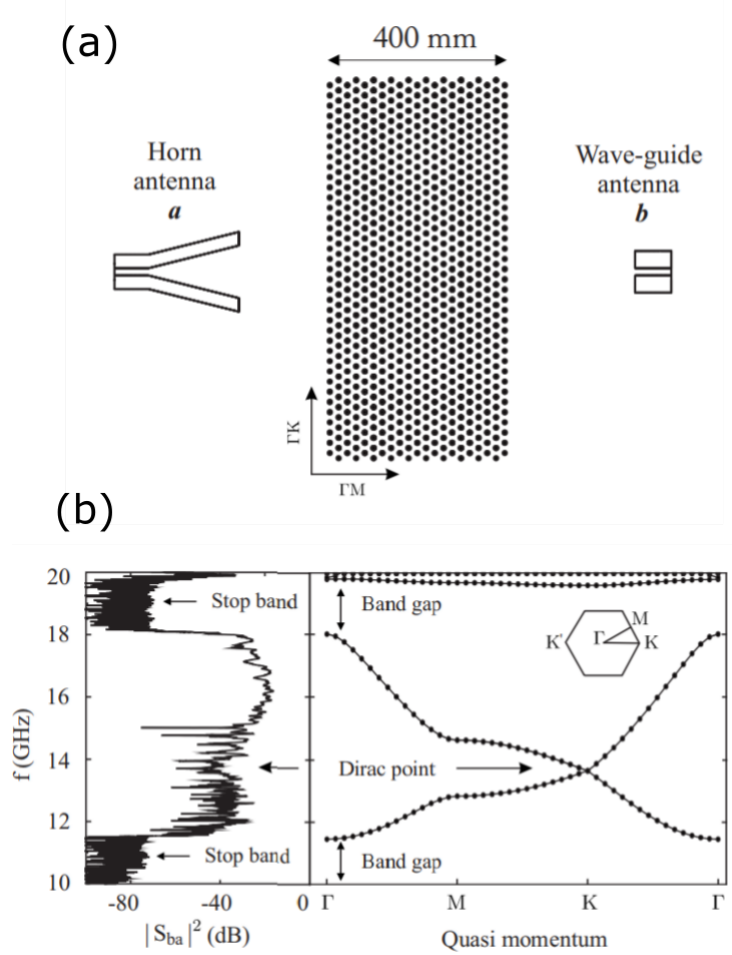

Figure 2.15: (a) Experimental setup. Long metallic rods were arranged in triangular array. Horn antenna is used to excite EM waves. (b) Measured transmission spectrum and calculated band structure. Adopted from [100].

fields, see Fig. 2.16a. This allows one to use a TB model to describe microwaves propagating through the structure, playing the role of the electrons in graphene. A linear dependence of reflection coefficient was observed in the vicinity of the Dirac frequency which corresponds to the eigenfrequency of a single disk, see Fig. 2.16b. In a later work [104] the authors calculated and measured the density of states of the studied AG as well as the wave function associated with each eigenfrequency. Topological phase transitions of Dirac points in anisotropic honeycomb lattices have also been observed [102]. Applying an anisotropy to the structure results in transition from gapless phase to the gapped phase.

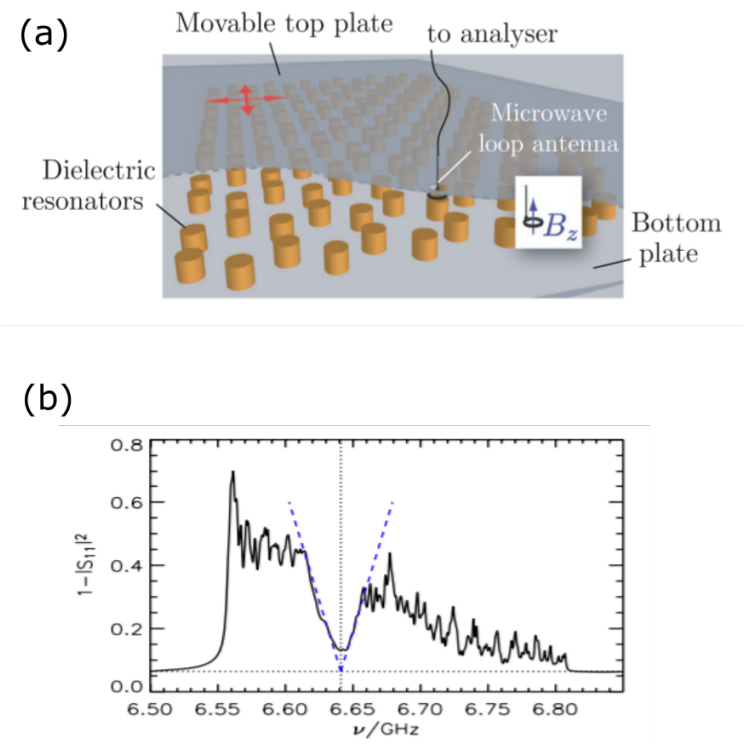

Figure 2.16: (a) Experimental setup. A dielectric rods were arranged in a honeycomb array inside a metallic cavity. Loop antenna is used to excite modes of the crystal. (b) Measured reflection spectrum shows dip in reflection at Dirac frequency of 6.64 GHz. Adopted from [102].

The cited above works demonstrate Dirac dispersion implicitly through reflection measurements. In this work we will demonstrate two AG systems that do not require to be inside the cavity and thus the full map of electric field can be obtained in order to directly obtain the dispersion relationship.

Graphene-inspired arrays of metallic particles have also been considered theoretically, and were shown to possess collective plasmon modes, full analogues to the electronic states in graphene [105, 106].

Graphene's unique dispersion relationship where electron behave as massless particles increased the interest in Dirac physics and topology of a wide scientific community. Back in 1988 Haldane showed in his theoretical paper that quantised Hall conductance can be achieved in what he called at that time "2D graphite" without an orbital magnetic field - the quantum anomalous

Hall effect [107]. Haldane used a TB defined on a honeycomb lattice with real valued nearest-neighbour hopping term and complex next-nearest-neighbour hopping term. This model is now known as Haldane model.

In 2008, the Haldane model was applied in the photonics domain [108, 109]. Haldane and Raghu demonstrated the existence of unidirectional propagating edge states in PhCs. The recipe to achieve this behaviour included usage of magneto-optic materials and hexagonal lattice geometry. These two conditions give means of introducing broken time-reversal symmetry and degeneracy points. Through their works, Haldane and Raghu have inspired the field of Photonic Topological Insulator (PTI) with many outstanding works to follow. Later, various research groups showed that one-edge mode in PhC can be observed in more general settings [110–112]. In [112] authors demonstrated that PhCs composed of an array of evanescently coupled helical waveguides arranged in a graphene-like honeycomb lattice supports one directional edge mode that is topologically protected from scattering, see Fig. 2.17.

The next step forward was to achieve photonic topological states without magnetic field and magnetic materials. Khanikaev *et al.* [113] suggested that it is possible to construct PTI using metacrystals - superlattices of designed electromagnetic media with carefully chosen parameters. The proposed design can be seen in Fig. 2.18a. The authors proposed to use a Metamaterial (MTM) with a high bi-anisotropic response, namely, a combination of cut wires and split ring resonators. They demonstrated that by combining two MTMs with opposite sign of magneto-electric coupling it is possible to create an edge state which is robust to defects and backscattering, see Fig. 2.18b and Fig. 2.18c.

In Chapter 6 we will show experimental results for another proposed design to achieve topologically protected states in AG. Instead of taking two atoms unit cell, Wu and Hu considered a larger cluster with six atoms. This results in back-folding of the modes and doubly degeneracy of Dirac crossings at the Γ

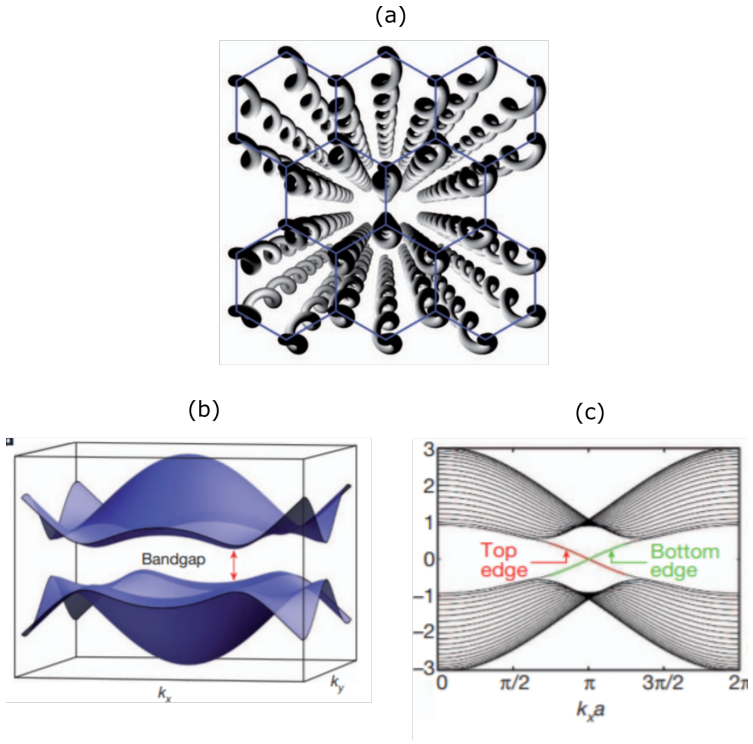

Figure 2.17: (a) Sketch of an artificial topological insulator system comprised of helices in a honeycomb array. (b) Calculated bulk band structure. (c) Calculated band structure of the edge modes propagating at the top and bottom of the array. Adopted from [112].

point. Authors suggested that specific deformation, namely moving elements away from the center of the cluster, would lead to the gap opening and band inversion at the Dirac point, a character for existence of topologically protected states.

In conclusion, we have given an overview of the studies most significant and relevant to this thesis in the exciting field of AG. Despite the extensive research done in this area, the experimental works lack direct observation of the Dirac spectrum and spectrum of the edge modes. To obtain dispersion relationship of the EM waves supported by the structure one needs to have experimental setup measuring fields across the entire sample (how this can be done is explained in Chapter 3). In the current thesis, we aim to address this gap. We also are in search of the most simple and thus easy modifiable AG using readily available in-house methods of fabrication.

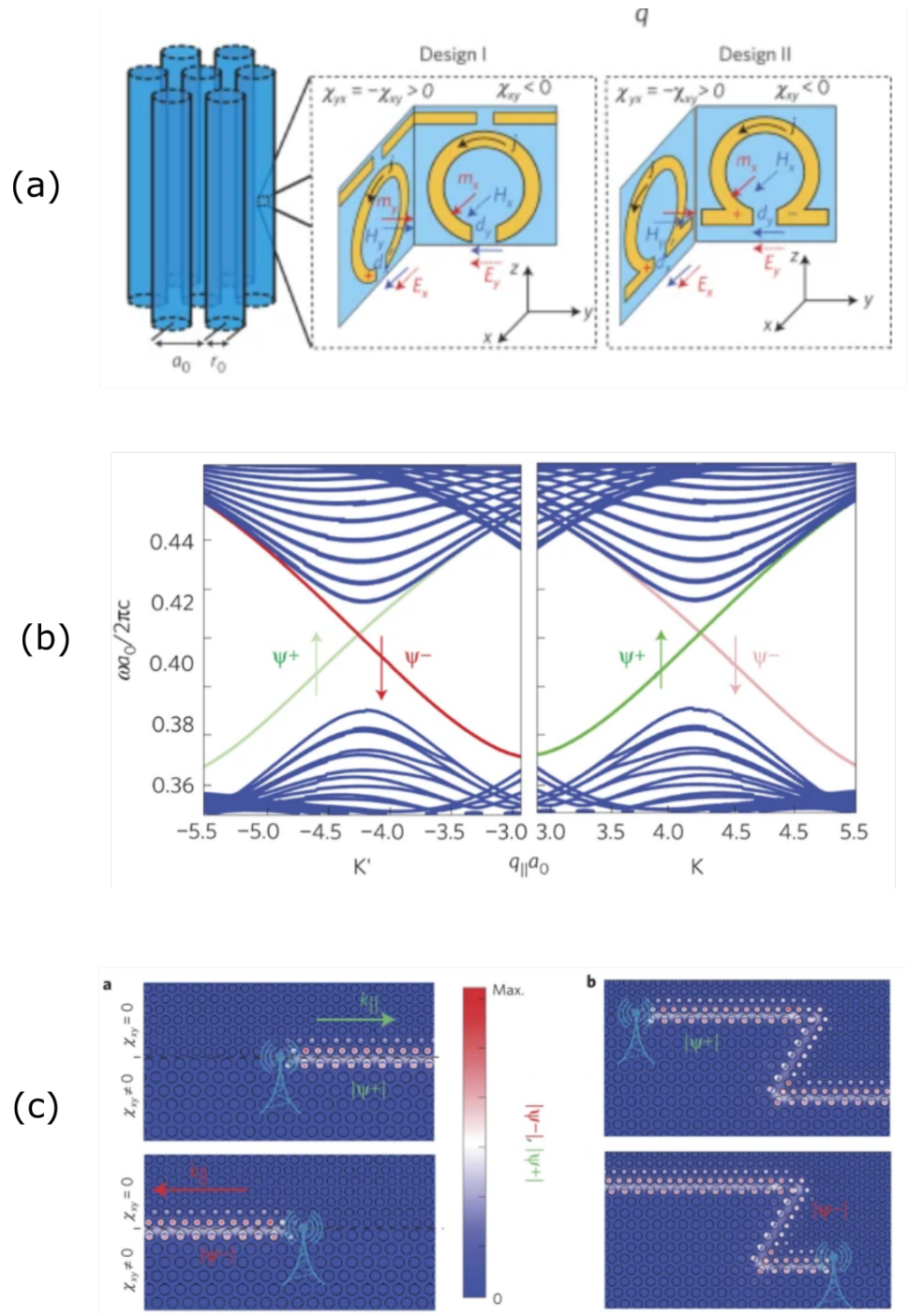

Figure 2.18: (a) The hexagonal lattice of the metacrystals and two possible microscopic structures of its metamaterial constituent rods with desirable bi-anisotropic response. (b) Dispersion of the spin-up (green) and spin-down (red) helical edge states supported by a bi-anisotropic domain wall. (c) Selective excitation of spin-up and spin-down photonic one-way edge states along a straight and zig-zag interfaces. Adopted from [113].

CHAPTER 3

METHODS

Compared with a Photonic Crystal (PhC) which operates in the visible part of the light spectrum, the microwave family of PhCs benefit from a variety of mature microfabrication techniques which are widely available and at a lower cost. Fabrication as well as measurement techniques do not require years of learning and perfecting specialised fabrication skills. This allows an academic researcher to concentrate on the phenomena under study as samples can be fabricated and improved within a short time frame. This also explains why the microwave regime is often used as modelling platform before transferring concept to nano scale regime.

In this chapter we first describe fabrication methods which were used to produce two types of microwave PhCs studied in this thesis. We then move on to explain the experimental techniques which were used to excite and detect both amplitude and phase of propagating surface waves. We also describe the details and specifics of data processing to obtain the band structure of the PhC eigenmodes. A Finite Element Method (FEM) supported by the commercial numerical package COMSOL Multiphysics® is used to compare measured band

structure with numerical models. Such models not only facilitate analysis of the experimental data, but also help one to understand the physical mechanisms behind propagating surface waves. Finally, the principals of equivalent LC circuit modelling used to model wired media will be introduced.

3.1 Experimental Techniques

3.1.1 Sample Fabrication

Two types of samples are considered in this work. In Chapter 4 we study an artificial microwave graphene comprised of metallic rods arranged in a honeycomb pattern. In this arrangement rods play the role of carbon atoms in real graphene. The rods are supported by a dielectric foam slab with low permittivity, close to air. A CNC machine was used to drill holes of the required diameter at the nodes of the honeycomb lattice. Steel rods were then manually inserted into each hole. Each rod represents a carbon atom in graphene.

A second type of microwave graphene structure is considered in Chapter 5 and Chapter 6. The sample is simply connected wires forming an hexagonal mesh. In this arrangement the wires represent bonding links between carbon atoms in real graphene. There are a plethora of patterning techniques which could be used to fabricate such structures. One could solder short wires to form an hexagonal mesh. Alternatively, one can start with a plain metal sheet and by selectively removing some areas obtain an hexagonal mesh. A diamond scribe can be used to perform this operation, but this is time consuming. Instead, photo lithography is a convenient and widely available method which may be utilised to achieve the desired wire-mesh microwave graphene.

Normally the full process of photo-lithography starts with depositing a negative or positive photoresist on top of the surface to be patterned. This

can be done by spin coating, dip coating, spraying, or jet dispensing. The photoresist is baked to evaporate solvents and to solidify it. It is then exposed to light radiation through a shadow mask to selectively modify the photoresist properties in certain areas. If a negative photoresist is used, the exposed areas are hardened by the photo radiation and becomes non-removable during the development process. If a positive photoresist is used, the exposed areas are softened and can be easily removed by the developer chemistry. Once the photoresist is developed, the remaining pattern of photoresist can be used as a protection mask. The next step is to remove areas unprotected by the mask by etching. Both dry and wet etching can be used to remove unprotected areas. In the dry etching process the sample is exposed to a directional plasma steam which removes unprotected areas of the metal film. In the wet etching process the sample is submerged into a solution of specific chemicals which dissolves unprotected areas.

A more simple patterning technique is utilised in the current work and is presented in Fig. 3.1. We miss the step of deposition of photoresist and its developing. Instead a protecting mask is directly created on top of the plain bi-layer sheet by printing the required pattern using a solid ink printer (Xerox ColorQube). The bi-layer sheet (ready to buy) is made of a 19 μm copper layer supported by 50 μm layer of Mylar. Mylar, also known as BoPET (Biaxially-oriented polyethylene terephthalate) is a polyester film made from stretched polyethylene terephthalate (PET) and is used for its high tensile strength, chemical and dimensional stability, transparency, reflectivity and electrical insulation. Solid ink printers use solid ink sticks which are made of wax and dye. When printing, the sticks are heated to the melting point and the ink is then transferred onto the paper to produce the printed image. It is similar to offset printing, where the image is produced and then placed onto the paper to create the print. The patterned sheet is then submerged into an iron chloride

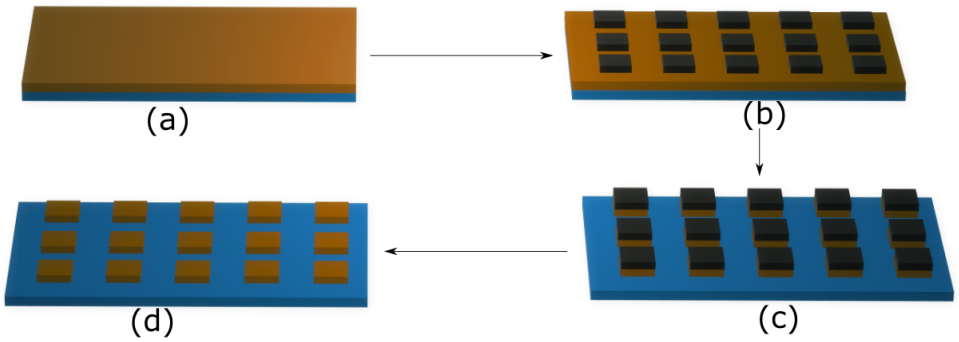

Figure 3.1: Fabrication of the wire-mesh microwave graphene. (a) Bi-layer plane sheet made of 18 μm copper layer supported by 50 μm polyester material. (b) Patterned protective layer. (c) Copper layer is etched in $FeCl_3$ solution. (d) Protective layer is removed by a solvent.

solution for about 2- 15 minutes (depending on the solution concentration and pattern to be etched) to remove unwanted unprotected areas. The chemical reaction of etching copper (Cu) with iron chloride solution ($FeCl_3$) reads as

$$2FeCl_3 + Cu \rightarrow 2FeCl_2 + CuCl_2 \tag{3.1}$$

Finally, printer ink can be removed by a solvent such as acetone but it can also be left on top of the patterned surface as it was shown that it has minimum influence on the propagating surface waves. Features down to 100 μm can be achieved using this simple fabrication methods with the resolution being limited by the single pixel resolution of the printer. Maximum supported sample size is limited by the paper size taken by the printer model, in our case A3. This fabrication method is fast and cheap - samples can be fabricated in less than 2 hours and cost less than £20.

3.1.2 Measurement Technique

A Vector Network Analyser (VNA) is used as the main tool to excite and detect propagating surface waves. Complex S-parameters are measured by the four-port VNA by recording the ratio of the emitted and received signals for the four possible pathways through the device under study. S-parameters are

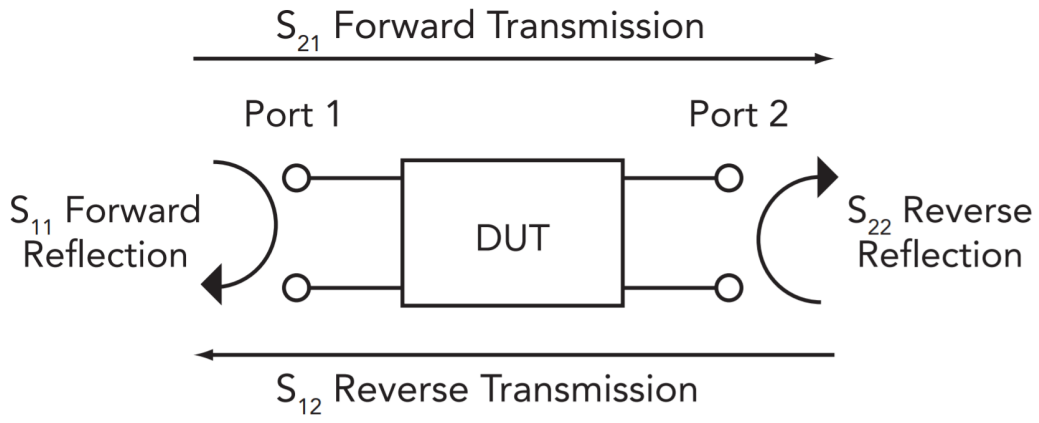

Figure 3.2: Schematic representation of VNA ports and corresponding S matrix parameters. Taken from the VNA manual.

usually recorded as matrix elements S_{ij} where i denotes the receiving port and j denotes the emitting port. In this notation S_{21} would be the ratio of the signal applied to the sample from the port 1 and measured at the port 2, schematic presentation can be seen in Fig. 3.2. Each element of S_{ij} is a complex number which records amplitude and phase of the incoming signal in reference to the outgoing signal. A VNA can be used in a frequency sweep mode to record S_{ij} parameters for a wide range of frequencies. This will give frequency characteristics of the sample under the test. The particular VNA used in this work, Anritsu VectorStar MS4647, is capable of measuring between 100 kHz and 70 GHz.

The generated VNA signal is transmitted by coaxial cables and can be radiated into the free space by antennas which are described later in this section. Coaxial cables used in this work are Gore Phaseflex, these cables are phase and amplitude stable which means that the signal is not affected even if the cable is deformed (below a certain deformation threshold). When the VNA is used to measure a system under the study, the resulting signal is a combination of the system response with the signal of the open loaded coaxial cables and antennas attached to the cables. A calibration process called short-open-loaded-through (SOLT) can be used to separate out the required

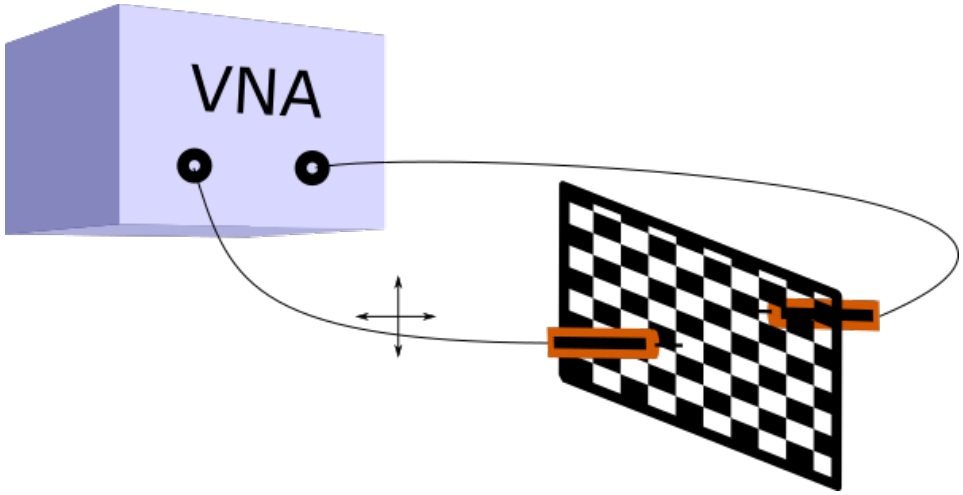

Figure 3.3: Experimental setup used to collect measured signal of propagating surface waves.

system response.

To excite and detect surface waves of the artificial microwave graphene a pair of simple probes were created by removing several millimeters of the outer conductor and dielectric cladding from the open end of a coaxial cable. This leaves the core conductor wire of a length l exposed into the free space. Length l defines the frequency when the core conductor wire antenna behaves as a dipole oscillator. When performing the measurements, one needs to make sure that the frequency range of the measurements are not in the region of resonance frequency of the antenna ($4l$). The source antenna should be placed above the sample element where it has maximum value of normal component of electric field. The oscillating charge at the tip of the source induces the charges at the element causing the collective oscillations of the whole structure.

The experimental set-up used throughout this work is shown in Fig. 3.3. The exciting antenna is placed in the proximity to the sample surface and is located at this fixed location during the whole experiment. Often this will be at the centre or at the edge of the sample. The position of the exciting antenna should be chosen thoughtfully to maximise the coupling strength. By tilting the antenna it is also possible to control the coupling efficiency between

the VNA signal and the system eigenmodes. The out-of plane wave vector component of the system eigenmodes is not restricted by $|\mathbf{k}| \leq \omega/c$ where ω is the wave frequency and and c is the speed of light. Therefore, this simple core conducting wire antenna will excite surface waves which are propagating radially away from the antenna location by coupling with the eigenmodes out-of-plane component. A dielectric, impedance-matched absorber such as carbon loaded foam can be used to prevent back-scattering of the waves from the sample edge.

A second antenna connected to the VNA is used to detect propagating surface modes. This antenna is identical to the emitting antenna and is brought into close proximity to the sample surface on the other side to minimise cross-talk. It collects amplitude and phase of the local electric field which are then recorded by the VNA. The second antenna can access the full area of the sample and is raster scanned across the sample area by a motorised dielectric mount with a maximum scanning area of 1 m x 1 m. A customised LabView code is used to control the VNA and to move the probe antenna in the x and y directions. The minimum step size of the scanner is 0.2 mm. To avoid gravity sag, the sample is mounted vertically and the detecting antenna is scanned in the vertical plane parallel to one of the sample surfaces.

An example of typical maps collected by this set-up are shown in Fig. 3.4. In the presented case, the exciting antenna is placed at the centre of the plane system under the study. In panel (a) the collected time-averaged electric field E_0 is plotted, panel (b) shows measured phase Φ, and in panel (c) we reproduce instantaneous electric field $E = \mathrm{Re}(E_0 \exp(i\Phi))$ of the measured surface wave using recorded values of E_0 and Φ. It can be seen that E_0 is a maximum at the position of the exciting antenna and gradually decays towards the sample edges approximately as $1/\sqrt{r}$ where r is the distance from the sample centre.

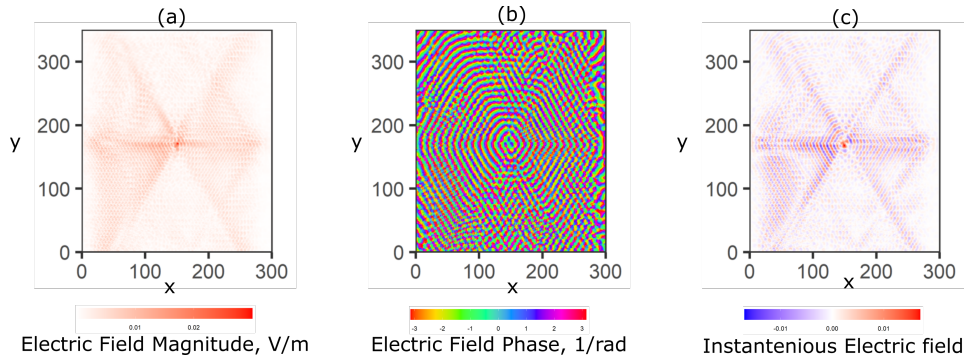

Figure 3.4: Collected signal of a propagating surface wave. (a) Time-averaged electric field E_0. (b) Signal phase Φ. (c) Reproduced instantaneous electric field $E = \mathrm{Re}(E_0 \exp(i\Phi))$.

3.1.3 Data Post Processing

Spatial FFT of the instantaneous electric field maps is used to extract and analyse propagating surface waves supported by the system. This allows one to separate multiple modes which are unavoidably excited even when a single frequency is applied to the system by the VNA. FFT results in a map of the system eigenmodes plotted in reciprocal space. It is convenient to present this map as an isofrequency plot when the intensity of all propagating modes at a given frequency (their Fourier amplitude) is plotted on a 2D graph, see Fig. 3.5 (left). Alternatively, a cross-sectional plot such as the one presented in Fig. 3.5 (right) can be used to show all supported eigenmodes and their intensity along a chosen direction of the in-plane wave vector **k**. On both figures one can see dispersion of the exciting radiation in free space. In Fig. 3.5 (left) it appears as a high-intensity circle and in Fig. 3.5 (right) it is evident as a mode with linear dispersion. System modes which are bound to the surface have a higher momentum in the reciprocal space compared to momentum of free space radiation at the same frequency.

Let us set the coordinates of the detecting antenna movements, for simplicity, in the x direction only, as $x_i = i \cdot \delta x$ where δx is the step size and i is an integer number between 0 and I. If we denote the sample length in the

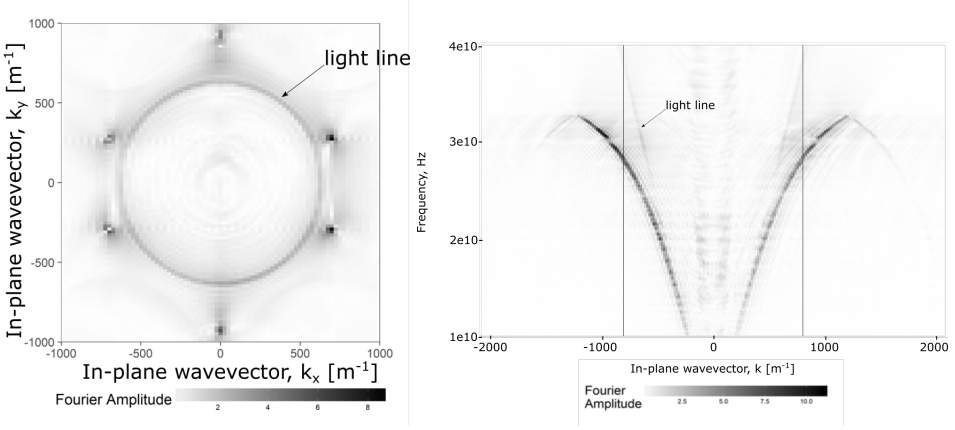

Figure 3.5: (Left) Example of 2D isofrequency plot of a propagating surface wave. (Right) Example of a cross-section plot of a propagating surface wave.

x direction as X_S, then the number of steps required to scan the full length is $I = X_S/\delta_x + 1$. After the FFT is applied to the collected data, the resulting reciprocal space maps will have a resolution of $\delta_k = 2\pi/(X_S + \delta_x)$ while the map length is given by $K_x = 2\pi/\delta_x$. A finer scanning step allows one to access modes with a larger wave vector while by fabricating and measuring larger samples we can increase the resolution of the reciprocal maps.

When choosing the length of scan and the scan step there are a few points one needs to consider: how many BZs need to be plotted, are there special points which need to have accurate value (high symmetry points). By measuring a minimum of two points per unit cell so that $K_x = 4\pi/U_x$ where U_x is the size of the unit cell in the x direction we can ensure that resulting eigenmodes maps cover the first two BZs. To have a point at an exact place T in reciprocal space one should choose the length of scan to be $X_s = \frac{2N}{\pi T}$, where N is an integer number. One can either trim the length of the scanned points or artificially add the needed number of points (i.e. zero padding) to the scan to achieve a value in the desired point.

Below we show a simple example of the FFT processing of the signal and how sampling size can affect the resulting spectrum. Let's define a signal as a sum of harmonics $f(x) = 0.2 * cos(x) + 0.1 * cos(2x) + cos(3x) + 0.5 * cos(4x)$

with sampling rate 1 mm as shown in Fig. 3.6a. The length of scan is 51 mm. We then perform FFT of the "collected" data. The extracted Fourier amplitudes are plotted against wave vector values in Fig. 3.6b. A different spectrum is obtained if the sample length is equal to an integer number of the signal wavelength. This case is presented in Fig. 3.6c. The side lobes of the FFT data have considerably reduced and the main harmonics are at the correct k-vectors with a bigger amplitude. However, a real signal will have an unknown wavelength making it impossible to choose the correct scanning size. But a simple method can be used to achieve the required resolution. To process the collected date, one can continuously remove measured points from one side of the collected data array until an integer number of wavelengths fits within the sampling length of the reduced data set. This technique is also handy when an exact point in reciprocal space is needed, e.g. edge of the BZ. Let's take a simple example. The period of the square lattice is $a = 4$ mm, with corresponding edge of the BZ equals to $K_{BZ} = \pi/a = 785.4$ m^{-1}. Let's "scan" $X_S = 300$ mm of the sample with a step of $\delta_x = 1$ mm. The resolution in reciprocal space is defined as $\delta_k = 2\pi/(X_S + \delta_x)$ and equal to $\delta_k = 20.87$ m^{-1}. This would give values at points n $\times\, \delta_k$, where n is an integer number. The nearest k values to the edge of the BZ are 772.34 m^{-1} or 793.12 m^{-1}. For the truncated by four points data array $\delta_k = 21.23$ m^{-1} which gives a value exactly at the BZ boundary. As was shown in the examples above, data with less points after truncating, can give extra information and can be a useful technique in data analysis.

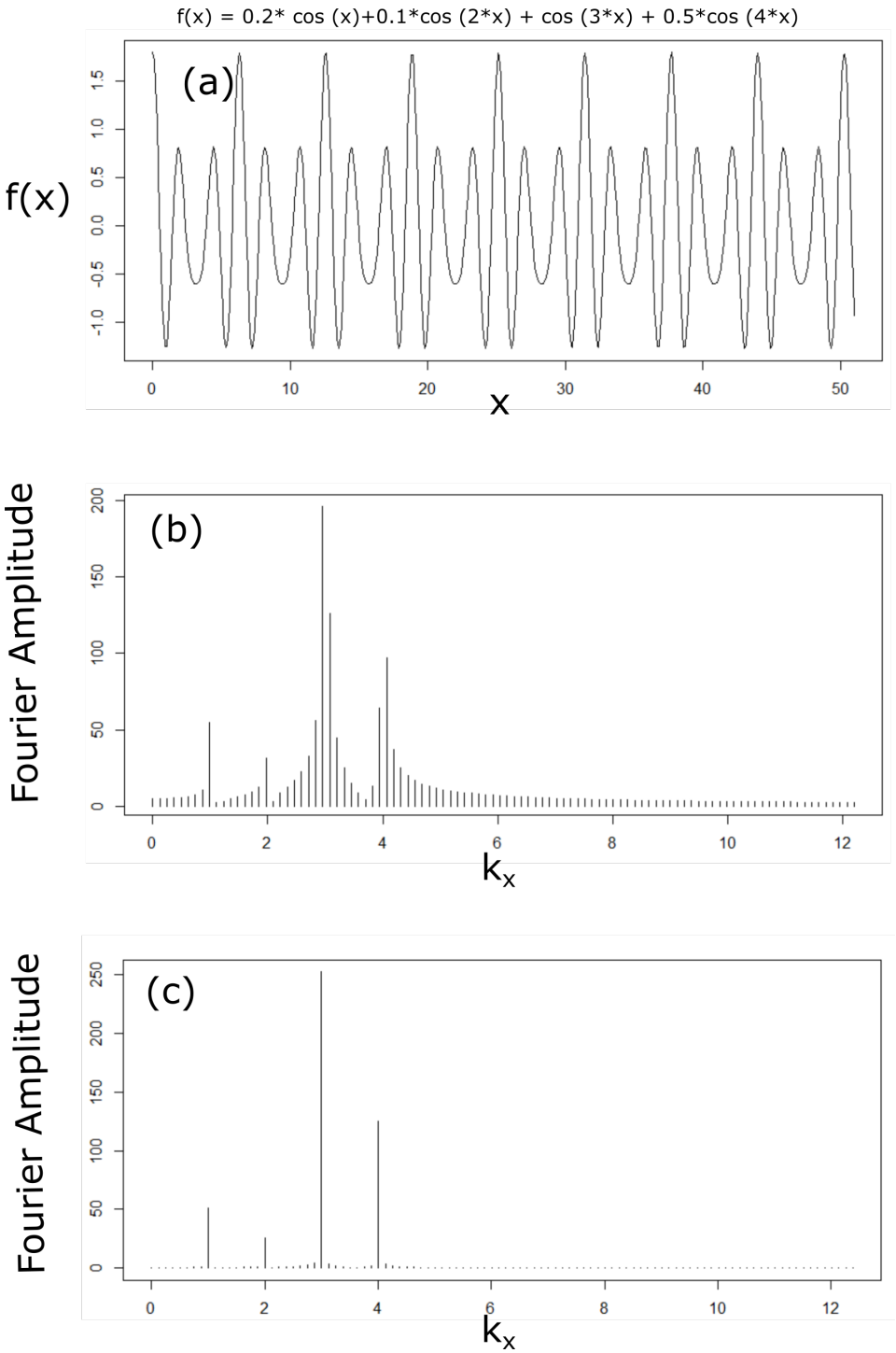

Figure 3.6: Example of performing FFT. (a) Analogue signal. (b) Wave vector extracted by the Fast Fourier Transform (FFT). (c) Wave vector extracted by the Fast Fourier Transform (FFT) after truncating original signal by four points.

3.2 Numerical Modelling

3.2.1 Finite Element Modelling

Numerical simulations are used throughout this work to predict eigenmodes supported by the microwave graphene systems under study. With modern modelling tools it is possible to design microwave systems with the desired performance without the need of iterative manufacturing. As we show in the following chapters, in all cases measured behaviour is almost an exact match to the simulations results.

Commercial package COMSOL Multiphysics® was chosen as a convenient tool for numerical simulations. This software has a powerful engine for solving Maxwell's equations using the Finite Element Method (FEM) and pre-defined models for various physical tasks, e.g. microwave systems. It also includes a graphical CAD module for creating 3D models of the system geometry.

In FEM, the object is divided into small, discrete elements. For 3D problems, tetrahedron elements are typically used to tile the object. This procedure is commonly called meshing. Maxwell's equations are then solved at the boundaries between the neighbouring elements. The solver calculates field components tangential to the single element edges at each vertex and field components normal to the edge face at the middle of each edge. This is shown in Fig. 3.7. Once the field components are calculated at these specific points they can be interpolated to other locations.

For eigenmode problems, the user first needs to create a 3D model of the system unit cell. Floquet boundary conditions governed by Floquet's theorem (better known as Bloch's theorem in condensed matter physics) are assumed at the borders of the unit cell. This allows one to model an infinite system without the need to create large 3D models and perform time-consuming calculations. In directions where the system has no periodicity, a different

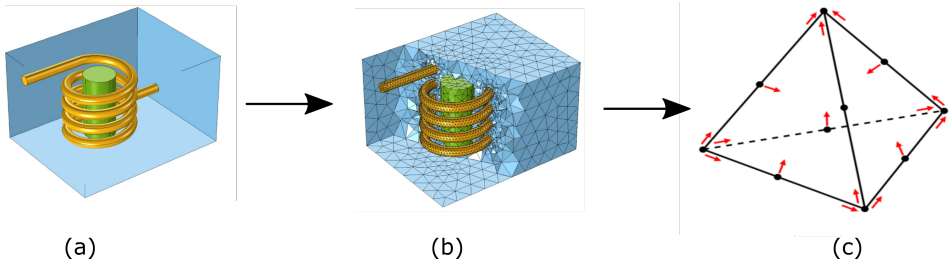

Figure 3.7: (a) A coil surrounding a magnetic core in an air domain. (b) The default Free Tetrahedral mesh feature is applied to the entire model. (c) Field components being calculated by the Finite Element Methods (FEM) for a tetrahedron mesh element. Adopted from Comsol manual.

type of boundary condition has to be defined. For all samples studied in this work, there are no physical obstructions in the out-of-plane directions. The radiation can flow with no surfaces or objects restricting wave propagation. In COMSOL Multiphysics® this can be approximated using a Perfectly Matched Layer (PML). This specific boundary condition is designed in such a way that ideally no radiation is reflected at the PML bottom surface. After reaching a PML the radiation penetrates inside and is gradually absorbed through the PML thickness. The top PML surface is usually terminated using a Perfect Electrical Conductor (PEC).

For electromagnetic eigenmode calculations, the software only needs to solve the wave equation which is derived from the full system of Maxwell's equations assuming no sources are present in the system. For electric field $\mathbf{E}$ the wave equation reads

$$\nabla \times \frac{1}{\mu}(\nabla \times \mathbf{E}) - k_0^2 \varepsilon \mathbf{E} = 0, \tag{3.2}$$

where μ and ε are the relative permittivity and permeability matrices, k_0 is the free-space wave vector. The above wave equation can be expressed in the matrix form and applied to the individual mesh elements:

$$\mathbf{Sr} - k_0^2 \mathbf{Tr} = 0, \tag{3.3}$$

where $\mathbf{r}$ is a coordinate vector, $\mathbf{S}$ and $\mathbf{T}$ are matrix operators, those explicit form will depend on chosen mesh, geometry and materials. By solving the

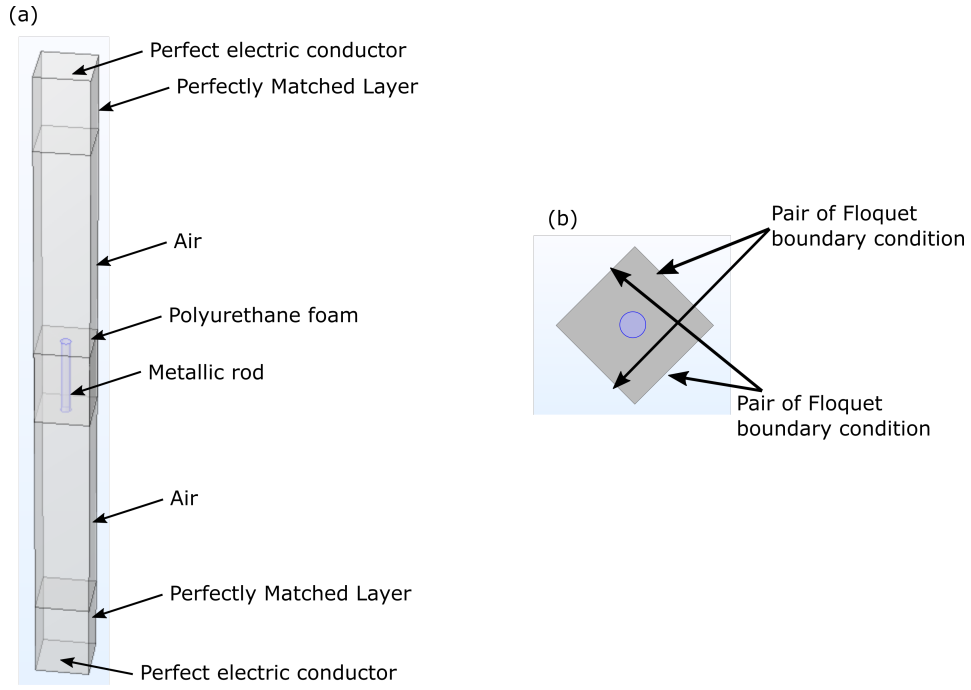

Figure 3.8: Sketch of the sample comprised of metallic rods in a square lattice

characteristic equation, the software obtains the full set of eigenvectors and eigenfrequencies. It should be noted that although eigenmode calculations allow one to reproduce the system bandstructure, no information is obtained about coupling strength of a given surface mode to the exciting radiation.

In order to calculate the correct electric field distribution, the FEM software needs to converge to the solution. This is an iterative procedure. First, the solver calculates field components for the vertices of the initial mesh. It then re-defines the mesh creating a denser meshing in the regions with largest field gradients. This procedure repeats until the difference between the calculated field from the neighbouring iterations is minimised to a given value. Once the convergence is achieved, the solver assumes that accurate enough field approximation has been obtained and the field distribution can be interpolated between mesh vertices.

An example of eigenmodes calculations using The COMSOL Multiphysics® is shown below. A simple system of periodic metallic rods in a square lattice is chosen for this demonstration. The geometry of the system unit cell is

shown in Fig. 3.8. In panel (a) we show a metallic rod which is represented by applying PEC boundary condition to all surfaces of the rod cylinder (which is a valid approximation for metals at microwave frequencies). Metallic rods are supported by a dielectric medium, e.g. polyurethane foam with permittivity and permeability close to air. Semi-infinite free space is created at the top and bottom of the unit cell as shown in the panel. It consist of a vacuum volume with the length of at least half the wavelength of the lowest studied frequency and PML at the top and bottom. PML absorbs radiation with no back-scattering. Finally a PEC layer is applied to enclose the unit cell in the vertical directions. In panel (b) we show a square unit cell from the top view. Floquet boundary conditions are applied in pairs to the opposite sides of the unit cell in the in-plane periodic directions, shown in panel (b).

The computed dispersion of the system eigenmodes is presented in Fig. 3.9. Discrete bold red dots of the obtained eigenfrequencies show dispersion of individual surface modes. The black line corresponds to the free space radiation, and is called the light line. Any modes above this line are radiative modes, and correspond to quantization within the full model which, among other elements, includes approximated semi-infinite spaces above and below the studied sample. These modes do not relate to the sample studied, and are artefacts of the model, and thus can be excluded in the Eigenfrequency search in COMSOL ®. Only the modes located below the linear dispersion of the free light are bound to the surface and are of interest for the purposes of this work.

Meshing. There are some considerations which need to be taken into account when creating the mesh for the structures described in this thesis. Firstly, we model infinite periodic structures and apply Floquet boundary conditions on the faces of the unit cell, thus the mesh on those paired faces should be identical. Comsol® functionality "Copy face" should be used to make sure the mesh profiles are identical. Secondly, the structures modelled in this

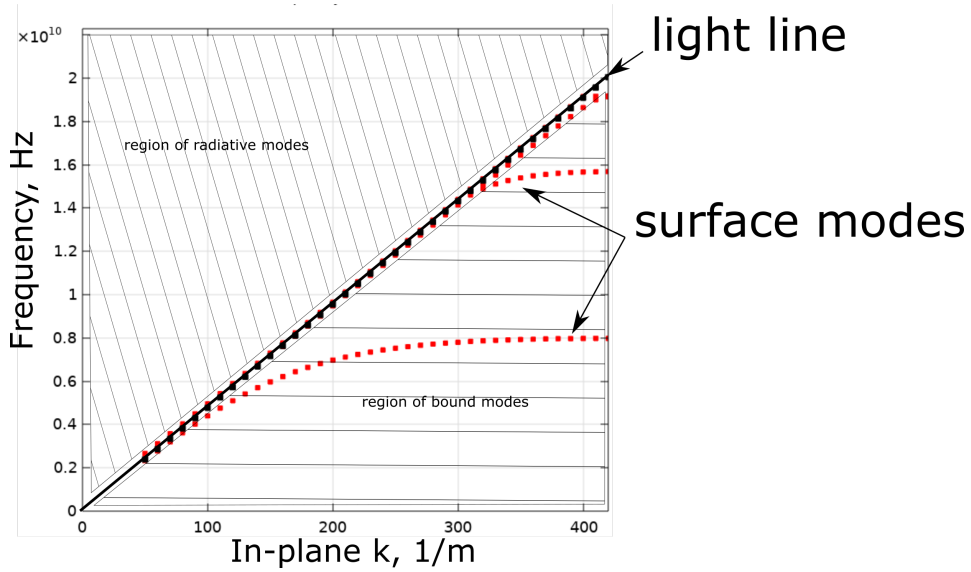

Figure 3.9: Dispersion calculated using Eigenfrequency solver in Comsol

thesis feature Dirac dispersion and critically depend on the symmetry. To preserve symmetry of the cell, a mesh should be created with respect to the symmetry. One may need to partition the unit cell into smaller parts and mesh one part first and then copy that mesh to the rest of the parts. Failing to do the right meshing may result in inaccurate results, i.e. a band gap may be present where there shouldn't be one. So in the case of the honeycomb lattice, C_6 symmetry, prior to meshing the rhombic unit cell needs to be divided into 12 equivalent pieces. Then only one of the pieces needs to be meshed, and this is copied across to other parts, see Fig. 3.10a. Finally, if the modelled structure has thin planar layers, such as in Chapter 4, it is advised to mesh the surface of the layer and then sweep it to the depth of the structure, rather than mesh with tetrahedrons, see Fig. 3.10b.

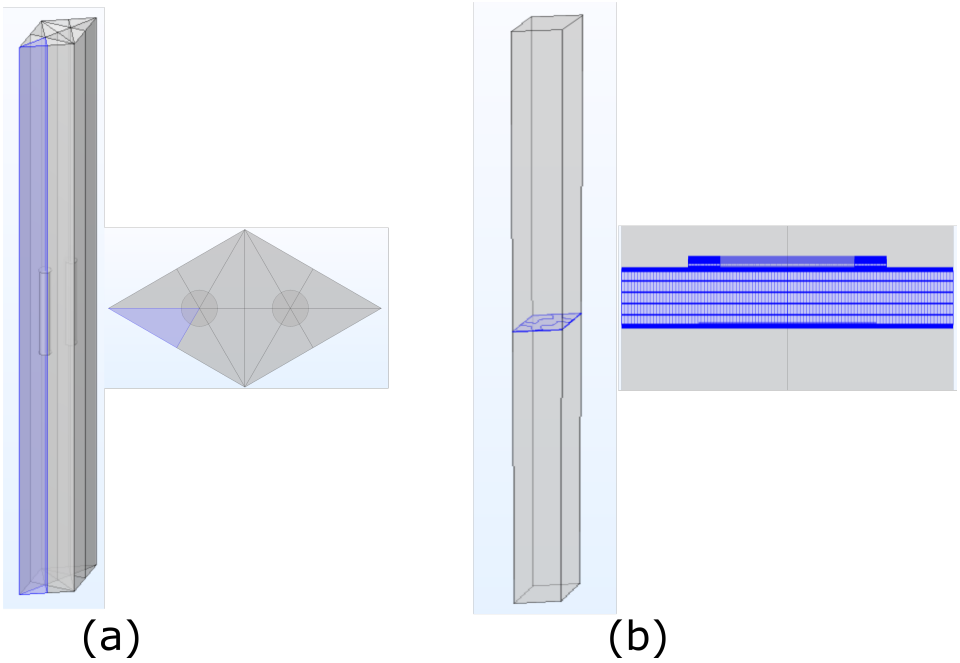

Figure 3.10: (a) Meshing of the rhomboid unit cell to preserve the symmetry of the cell. Cell is divided into twelve equal pieces. One piece was meshed and then copied across to other pieces. (b) Meshing the thin layer is done by meshing one of the flat surfaces first and then by sweeping meshed surface.

3.2.2 Equivalent *LC* Circuit Model

The focus of this work are periodic structures which emulate physics of real crystals for electromagnetic waves at microwave frequencies. Leon Brillouin wrote in his celebrated book "Wave propagation in periodic structures" [114] that "waves always behave in a similar way, whether they are longitudinal or transverse, elastic or electric. ... all problems discussed [in his book] deal with periodic structures of various kinds, and they all lead to similar results: these structures, be they electric or crystal lattices, behave like band-pass filters". This statement resonates with our work where atomic 2D crystals with the hexagonal lattice symmetry are being emulated with microwave analogies, which, in turn, can be described with the equivalent *LC*-circuit theory [115].

Connected metallic structure (e.g. studied in Chapter 5) supports electric currents which are propagating along it. To construct an equivalent *LC* circuit of a structure, one needs to determine the main source of the capacitance

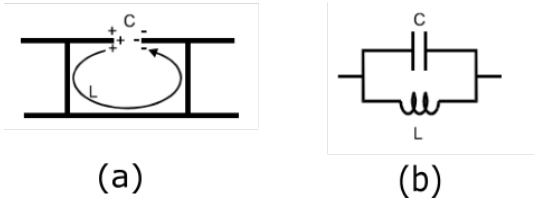

Figure 3.11: Equivalent LC circuit of a "mushroom" structure.

and inductance in the system. One of the simple and illustrative examples for defining an equivalent LC circuit is a "mushroom" structure discussed in Chapter 2 (Fig. 2.3). The main source of the capacitance is defined by the proximity of the top metal patches, the current loop meanwhile dictates the inductance term (Fig. 3.11a). Electromagnetic properties of the surface can be reduced to a rather simple equivalent LC circuit (Fig. 3.11b) [38]. However, if the constituent element of the surface is more sophisticated (i.e. split ring resonator, Jerusalem cross, or hexagonal mesh AG considered in Chapter 5), the equivalent LC model should reflect all capacitances and inductances in the system [116–118]. Once the equivalent LC elements have been defined inside the unit cell, one needs to define periodic boundary conditions by applying translation lattice vectors. Using Kirchhoff's laws one can find currents and voltage dynamics in the system. If currents and voltages are expressed via the flux variables, it is possible to obtain a set of equations which defines the eigenvalue problem. Detailed step-by-step calculations for a hexagonal mesh AG are shown in Chapter 5.

CHAPTER 4

RODDED ARTIFICIAL GRAPHENE

In this work we create an artificial graphene system operating at microwave frequencies by arranging metallic rod resonators into a honeycomb lattice. Two Dirac crossings are observed at all K and K′ points of the hexagonal BZ, a feature that has not been observed in graphene or other artificial graphene systems. We attribute this to the presence of higher order modes associated with individual rods. Our findings are confirmed by numerical, full-wave finite-element simulations which agree very well with the experimental data. We also show how one can achieve any desired frequency for the Dirac crossing by varying the parameters of the system. Later, in Section 4.2, we show the measured and modelled profiles of the electromagnetic fields at K and M points. In Section 4.3 we study the same system with broken inversion symmetry and its band structure.

4.1 Dispersion of Bound Electromagnetic Waves

To replicate the carbon atoms of graphene, steel cylindrical rods of diameter $d = 2$ mm and length $l = 15$ mm were inserted into a rigid foam slab (relative permittivity of $\epsilon_r = 1.05$), and arranged in a honeycomb array with a spacing between nearest rods $a = 5$ mm (see Fig. 4.1). The area of the sample was 250×300 mm and approximately 2400 rods were used. Electromagnetic modes within the sample were excited and detected using two stripped-end near-field antennas, connected to a microwave VNA. Both antennas were placed with their coaxial axes normal to the sample surface with the metal tips approximately 0.5 mm away from the surface and on opposite sides of the sample (to limit direct radiation transfer between the antennas). The near field of the source antenna provides sufficient in plane momentum to excite bound (i.e. non-radiative) modes in the foam-rod slab. To characterise the electromagnetic modes, the detecting probe was raster scanned across the sample surface with 1 mm step spacing in two orthogonal directions. Scanning with smaller step will not improve the resolution of the dispersion, as steps in real space dictate the length of the scan in momentum space and vice versa. See Chapter 3 for details.

The amplitude and relative phase of the local electric field (predominantly the z component, due to the orientation of the antenna) were measured at each spatial coordinate over a frequency range between 1 and 25 GHz, with 25 MHz steps.

A FFT is then applied to the measured field-data at each frequency step, to produce a matrix of complex Fourier amplitudes. Peaks in these amplitudes correspond to strong coupling to modes of the system, and hence by plotting the Fourier magnitudes as function of frequency and/or momentum (k_x, k_y), the

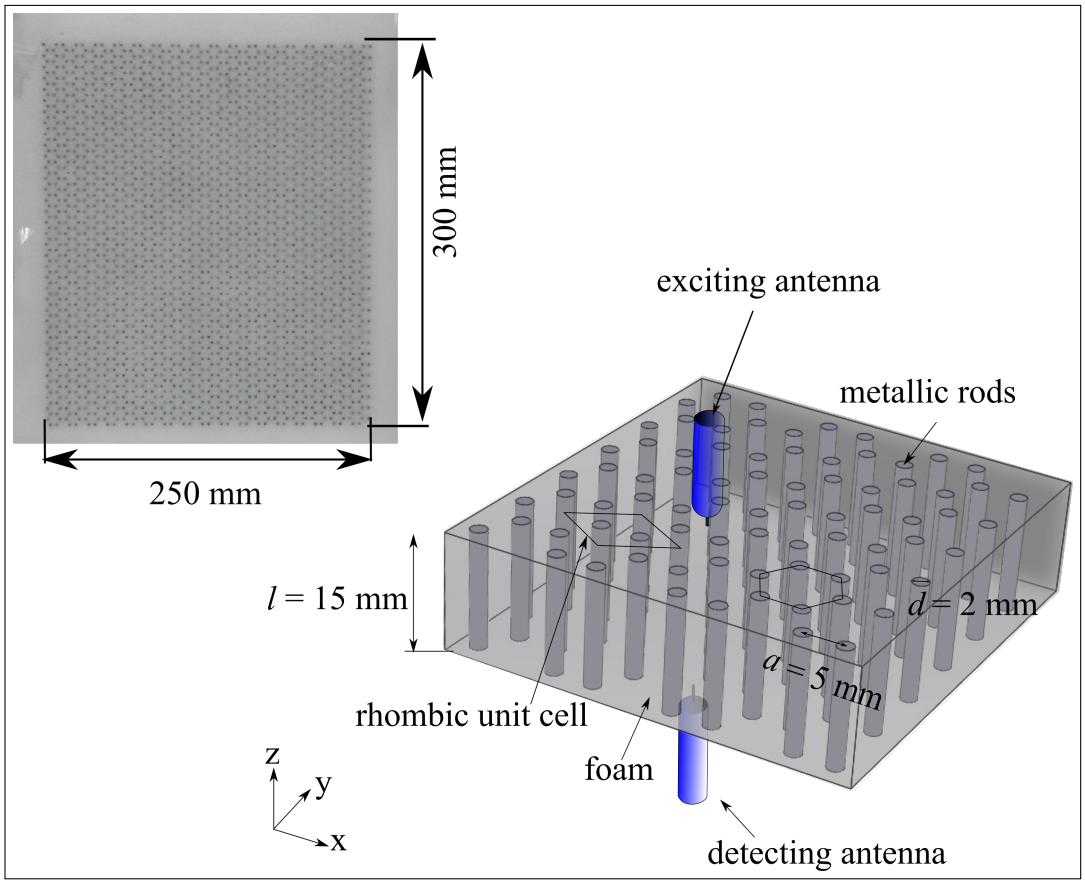

Figure 4.1: Schematic representation of the sample. Metallic rods of $d = 2$ mm diameter and $l = 15$ mm length are arranged in a honeycomb array inside a supporting dielectric foam with rod spacing $a = 5$ mm. Inset shows the photograph of the sample.

modes' dispersion and equi-energy contours can be observed. It is important to note that the absolute values of the Fourier amplitudes are not important (since they depend on the geometry and method of excitation), but the position of the maxima gives a good estimation of the system eigenfrequencies.

The full dispersion is then constructed by stacking iso-frequency data. For the complete band structure diagram (presented in Fig. 4.2) the data is constructed from three directions across the first BZ, namely $\Gamma - \mathrm{K}$, $\mathrm{K} - \mathrm{M}$ and $\mathrm{M} - \Gamma$. For the chosen rod spacing $a = 5$ mm the values of high-symmetry points are $\mathrm{K} = 483$ mm^{-1} and $\mathrm{M} = 418$ mm^{-1}. The data is measured in discrete points with 1 mm step and hence Fourier transform data is also discrete. As was shown in Chapter 3 the length of the scanning area should be decided by

considering which points are required post FFT processing. The optimal length of the scan in the direction towards K point is 247 mm and 255 mm in the direction to M point. Such scanning size ensures that the FFT array possesses data points at the high-symmetry points K and M.

The COMSOL Multiphysics® FEM frequency-domain solver was used to calculate the eigenmodes of the system. The metallic rods were treated as perfect electrical conductors embedded into a material with relative permittivity of $\epsilon_r = 1.05$ and with the remaining simulation domain described as air ($\epsilon_r = 1$). "Perfectly matched layers" were placed as top and bottom boundaries of the domain and Floquet periodic boundary conditions were applied to the four remaining sides of the rhombic unit cell in order to simulate an infinite honeycomb array (see Fig. 4.1). An eigenfrequency solver was used to obtain modes of the system with phase shift applied between the Floquet boundaries (that satisfy Floquet-Bloch theorem) in order to set the wave vector of the allowed modes. When meshing, extra care needed to be taken. To avoid breaking of the unit cell symmetry, meshing has to be identical for the two sub-lattices. Further details on how this was achieved can be found in Chapter 3.

The bound (non-radiative) modes of the sample are simply collective excitation of the rods, which disperse strongly on the approach to each eigenfrequency of an isolated rod. A metal rod is in resonance when approximately an integer number of half wavelengths is equal to the rod length

$$f \approx n\frac{c}{2l},$$

where n is an integer and l is the rod length. Strictly speaking, this is changed by the end effects and the rods finite thickness. However, the above equation provides a good approximation. For 15 mm long rods the first resonance is roughly at 10 GHz, the second being at 20 GHz, the third is at 30 GHz and so on. In Fig. 4.2 two Dirac crossings at the K point can be clearly seen at $f_{D1} = 8.325$ GHz and $f_{D2} = 16.325$ GHz. The frequency is further shifted down

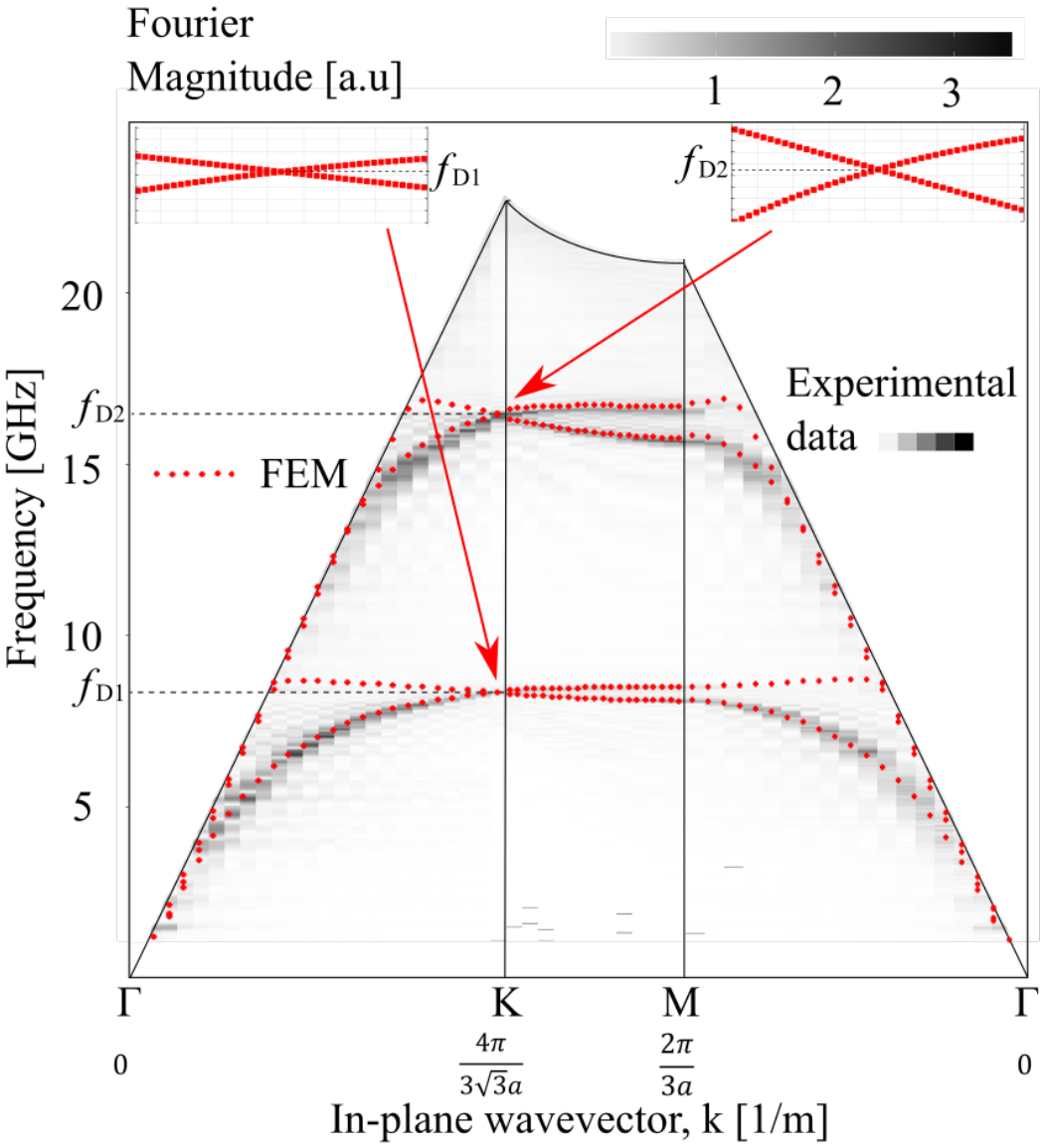

Figure 4.2: FFTs performed on the experimental field maps just above the surface of the sample provide an indication of the dispersion of the bound electromagnetic modes. Solid black lines represent the light lines (maximum momentum available to a propagating photon). Red points are results of the FEM modelling. Insets: Enlargements of the FEM predictions of the band structure in the vicinity of each Dirac crossing; The regions above the light lines correspond to radiative modes and are not under consideration. As such, the experimental data in these regions has been removed.

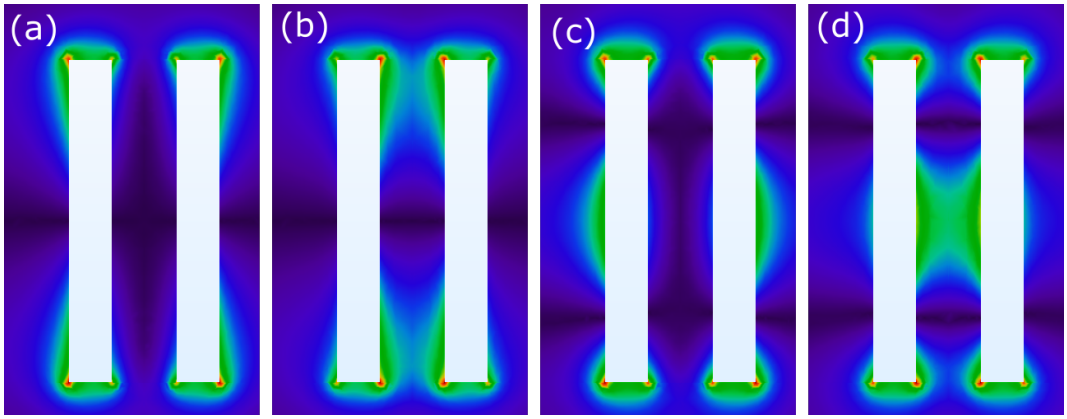

Figure 4.3: FEM predictions of the norm of the electric field for the 1st Dirac crossing at $f_{D1} = 8.325$ GHz (associated with the half wavelength resonance of the metallic rods) and for the 2nd Dirac crossing at $f_{D2} = 16.325$ GHz (associated with the full wavelength resonance of the metallic rods).

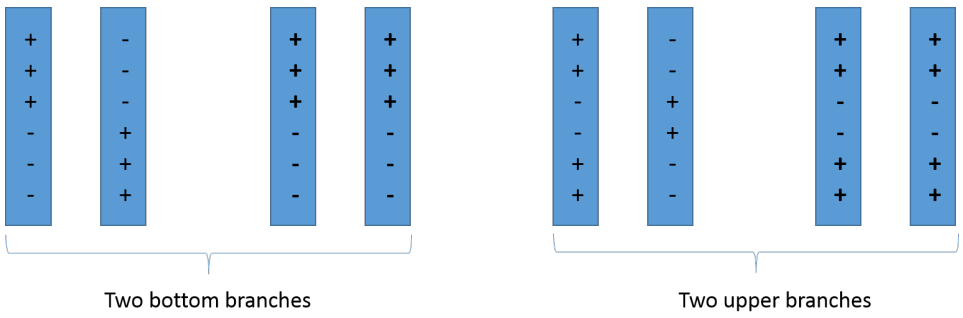

Figure 4.4: Schematic presentation of the charges along rods for four modes. If the modes are symmetric then the field inside are strengthened, if antisymmetric then fields are cancelled out.

due to collective oscillation effects. In Fig. 4.3 the magnitude of the total electric field is plotted along the rods length. Panels (a) and (b) show two modes for the first resonant frequency, panels (c) and (d) correspond to the modes of the second resonance. As can be seen from (a) and (b) panels the first resonance corresponds to one half wavelength resonance with maximum at the end of the rods and mode in the middle of the rods. The next resonant frequency (panels (c) and (d)) happens when two half wavelengths equal to the length of the rods with maxima at the end and the middle of the rods, and with two nodes quarter rod lengths away from the end of the rod. Two rods in the unit cell can oscillate in phase or out of phase. Fig. 4.4 shows a schematic representation of

out-of-phase and in-phase oscillations for the bottom branch and for the top branch. If the fields of the rods oscillate out-of-phase (odd symmetry) the fields are weakened between the rods, this can be seen in Fig. 4.3a and Fig. 4.3c. In contrast, if fields oscillate in-phase (even symmetry) then the field between the rods is strengthened (Fig. 4.3b and Fig. 4.3d).

Insets in Fig. 4.2 show an enlarged view of the predicted dispersion curves in the vicinity of the two mode crossings. Using a linear approximation for the dispersion relation near the K point, we obtain the following values for the Dirac group velocities for the guided modes supported by our system: $v_{D1} = 1.9 \times 10^6$ ms^{-1} (0.006 of the light speed); $v_{D2} = 6 \times 10^6$ ms^{-1} (0.018 of the light speed).

4.1.1 Iso-frequency Contours

The six equivalent Dirac points are evident on iso-frequency plots for f_{D1} = 8.325 GHz and f_{D2} = 16.325 GHz (Fig. 4.5). Scanning through the range of frequencies we confirm that there is no frequency at which a band gap opens. Similarly to real graphene, iso-frequency contours plotted below the Dirac frequencies f_{D1} and f_{D2} have a circular shape (Fig. 4.6), which corresponds to conical dispersion in the 3D k-space.

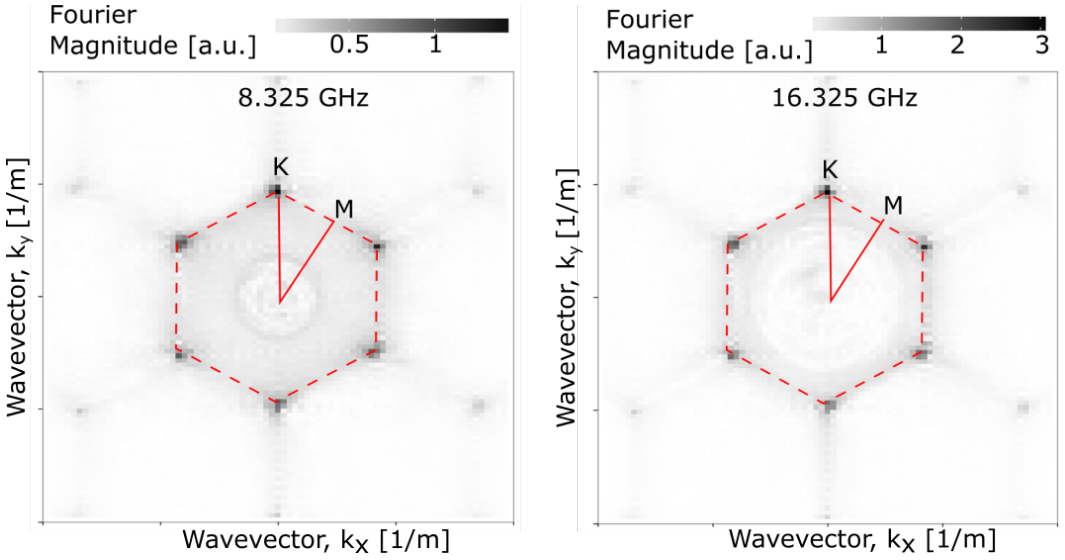

Figure 4.5: Equi-energy contours at the frequencies of the Dirac crossings $f_{D1} = 8.325$ GHz (left) and $f_{D2} = 16.325$ GHz (right).

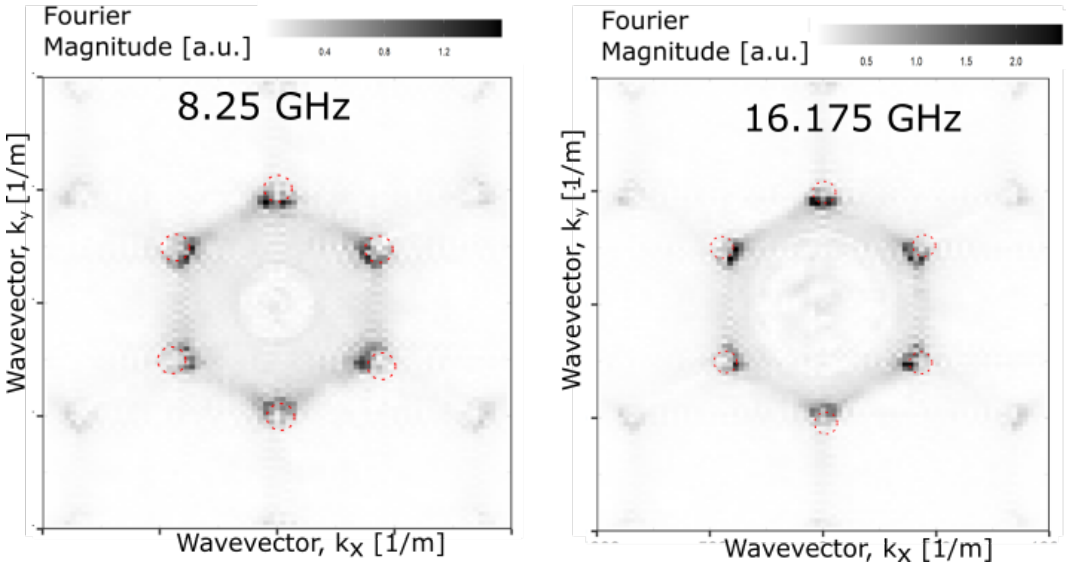

Figure 4.6: Equi-energy contours at the frequencies below the Dirac frequencies $f_{D1} = 8.25$ GHz , $f_{D3} = 16.175$ GHz. Circular shape confirms conical shape of 3D dispersion in the proximity to Dirac points.

4.1.2 Missing Upper Mode

Note that the upper modes which form the two Dirac crossings are absent in the experimental data (Fig. 4.2) for the Γ-to-K and Γ-to-M directions within the 1st BZ. To investigate this phenomena we plot dispersion in the extended zone scheme. For instance, the Γ-to-K direction becomes equivalent to the Γ-to-M direction when crossing the 1st BZ into the 3rd BZ (Fig. 4.7a). Similarly, the Γ-to-M direction becomes M-to-Γ equivalent in the 2nd BZ (Fig. 4.8a), and finally, going from the M-to-K direction brings us to the K-to-Γ equivalent in the 2nd BZ (Fig. 4.9a). In Fig. 4.7b it can be clearly seen that the upper modes of both Dirac crossings are missing on the Γ-to-K plot in the 1st and higher BZ (Fig. 4.7). However, in Fig. 4.8b the modes are missing in the 1st BZ but are present in the 2nd. Finally in Fig. 4.9b the modes which were not visible in the previous figures are now present.

The suppression of the upper bands in the 1st BZ can be shown to be a

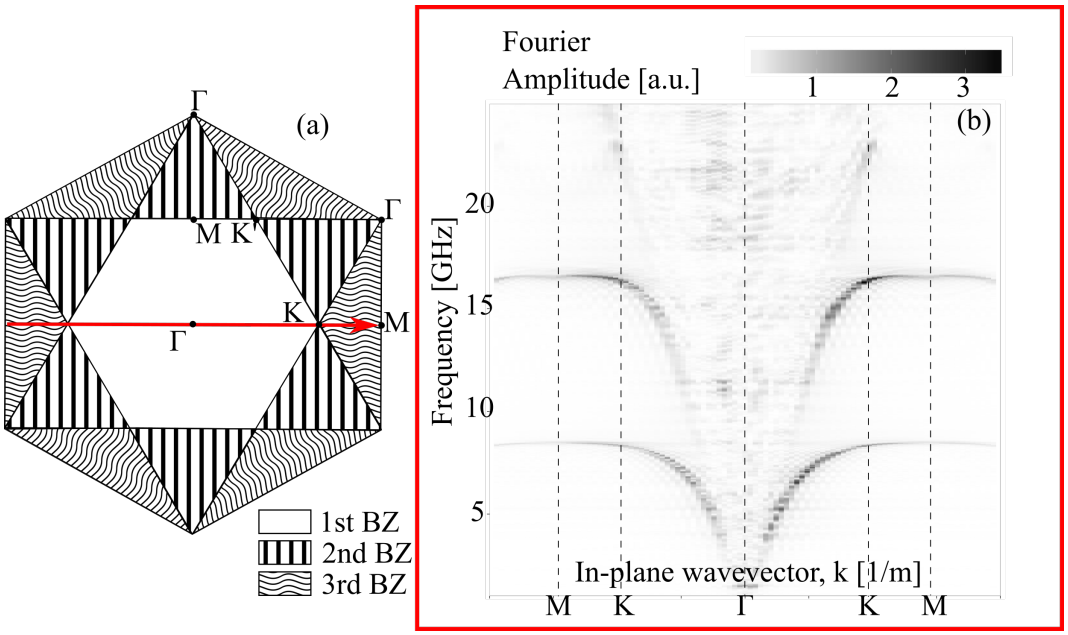

Figure 4.7: (a) Structure of the honeycomb BZs. First three zones are indicated. Red arrow indicates directions corresponding to the extended dispersion plot. (b) Experimentally determined dispersion relation for Γ-to-K direction extended into the 3rd BZ to the M-equivalent point (along the red line in (a)).

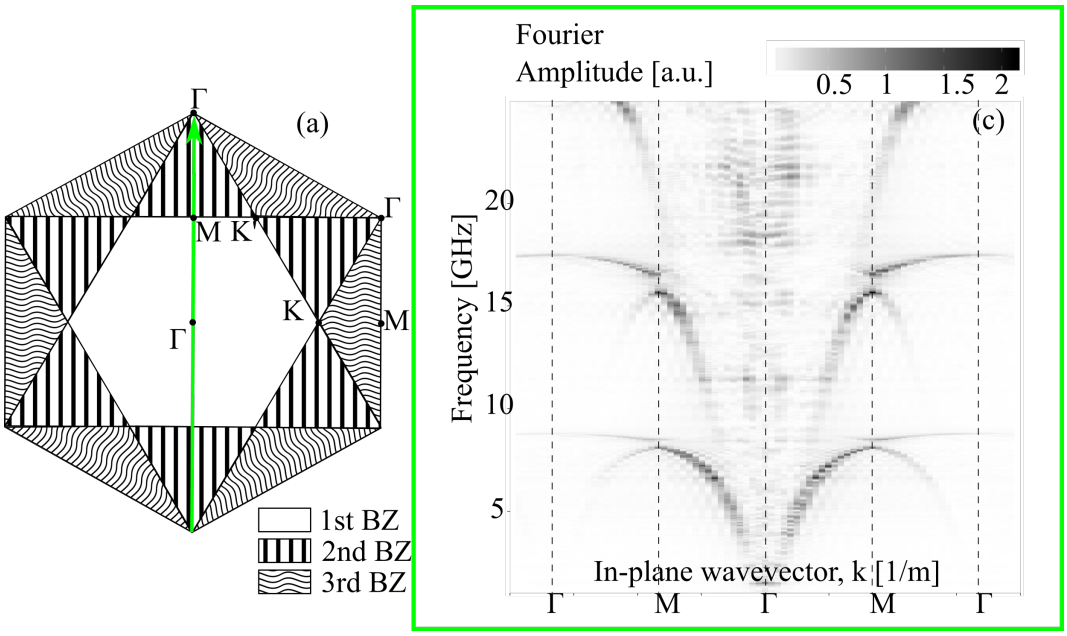

Figure 4.8: (a) Structure of the honeycomb BZs. First three zones are indicated. Green arrow indicates directions corresponding to the extended dispersion plot; (b) Γ-to-M direction extended into the 2nd BZ to the Γ-equivalent point (along the green line in (a)).

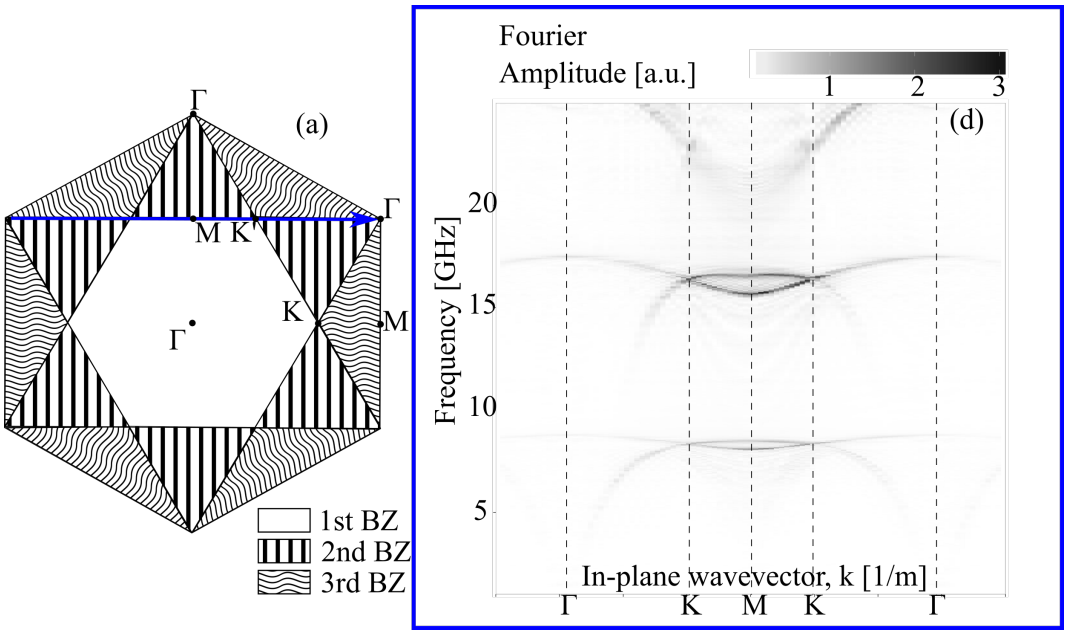

Figure 4.9: (a) Structure of the honeycomb BZs. First three zones are indicated. Blue arrow indicates directions corresponding to the extended dispersion plots; (b) Experimentally determined dispersion relation for M-to-K direction extended into the 2rd BZ to the Γ-equivalent point (along the blue line in (a)).

consequence of the symmetry of these modes. Let the electric field distribution of the mode with Bloch vector $\mathbf{k}$ be expressed as

$$\mathbf{E}(\mathbf{r}) = \mathbf{E}_{\mathbf{k}}(\mathbf{r}) e^{i\mathbf{kr}},$$

so that the Bloch function $\mathbf{E}_{\mathbf{k}}(\mathbf{r})$ is periodic under translations by the lattice vectors $\mathbf{T}$

$$\mathbf{E}_{\mathbf{k}}(\mathbf{r}+\mathbf{T}) = \mathbf{E}_{\mathbf{k}}(\mathbf{r}).$$

We treat $\mathbf{r}$ as a two-dimensional vector $\mathbf{r} = (x, y)$, assuming the observations are always performed in the same horizontal plane. The Fourier transform of this field profile at the wave vector $\mathbf{q}$ can be recast in the form of an integral over a primitive cell as follows

$$\int \mathbf{E}_{\mathbf{k}}(\mathbf{r}) e^{-i\mathbf{qr}} \mathrm{d}\mathbf{r} = \sum_{\mathbf{T}} \int_S \mathbf{E}_{\mathbf{k}}(\mathbf{r}) e^{i(\mathbf{k}-\mathbf{q})\mathbf{r}} e^{i\mathbf{T}(\mathbf{k}-\mathbf{q})} \mathrm{d}\mathbf{r} = 4\pi^2 \sum_G \delta(\mathbf{q}-\mathbf{k}-\mathbf{G}) \int_S \mathbf{E}_{\mathbf{k}}(\mathbf{r}) e^{-i\mathbf{Gr}} \mathrm{d}\mathbf{r}, \tag{4.1}$$

where $\sum_{\mathbf{T}}$ is a sum over all translation vectors of the lattice, the integral on the right hand side is performed over a primitive cell, and $\mathbf{G}$ is an arbitrary reciprocal lattice vector, and $\delta(\mathbf{q}-\mathbf{k}-\mathbf{G})$ is the Dirac delta-function. Eq. (4.1) immediately follows from the standard identity from band theory

$$\sum_{\mathbf{T}} e^{i\mathbf{T}(\mathbf{q}-\mathbf{k})} = 4\pi^2 \sum_{\mathbf{G}} \delta(\mathbf{q}-\mathbf{k}-\mathbf{G}).$$

Eq. (4.1) shows that the Fourier transform vector $\mathbf{q}$ can differ from the Bloch vector by an arbitrary reciprocal lattice vector $\mathbf{G}$. In other words, every reciprocal lattice vector $\mathbf{G}$ contributes a replica of the mode at the wave vector $\mathbf{q} = \mathbf{k} + \mathbf{G}$. The intensity of the replica depends on $\mathbf{G}$ via the integral on the right hand side of Eq. (4.1). Let us consider the case when the vector $\mathbf{q}$ is between Γ and K. This gives $\mathbf{G} = 0$ and $\mathbf{k} = \mathbf{q}$. Then, the integral over a unit

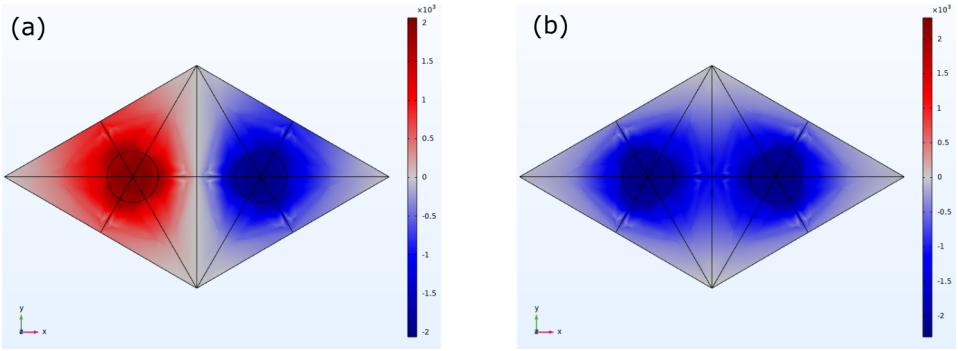

Figure 4.10: Prediction of the normal component of the electric field above a unit rhombic cell of the sample surface for $k_x = 0$ m^{-1} and $k_y = 300$ m^{-1} on the line from Γ-to-K for upper mode (normalised) (a) and for bottom mode (b).

cell vanishes if the Bloch mode is antisymmetric with respect to the mirror reflection about the Γ-K line. This is indeed the case for the upper branch, as obtained by FEM modeling, as can be seen in Fig. 4.10a. Therefore, the signal of this mode is indeed suppressed due to the vanishing integral in Eq. (4.1). For values of $\mathbf{q}$ outside of the 1st BZ, one has to employ a non-zero value of $\mathbf{G}$ in Eq. (4.1), so that the symmetry does not lead to suppression. This explains the re-emergence of the mode at larger values of $\mathbf{k}$ along the symmetry line. For comparison, the bottom branch is symmetric with respect to mirror reflection about the Γ-K line (Fig. 4.10b).

Let us now explain how the absence of the modes arises from the honeycomb symmetry. Mirror reflections along the three $\Gamma - \mathrm{K}$ lines transform the lattice into itself, exchanging the A and B sub-lattices. In general, these mirror symmetries, are not a symmetry of individual Bloch modes: each mirror reflection transforms a mode at a wave vector $\mathbf{k}$ into a mode at its mirror image $\mathbf{k}^\star$: $\mathbf{E}_\mathbf{k}(\mathbf{r}) \to \mathbf{E}_\mathbf{k}(\mathbf{r}^\star) \propto \mathbf{E}_{\mathbf{k}^\star}(\mathbf{r})$. The symmetry only implies that the two mirror modes have the same frequency, and one can construct odd and even functions by taking symmetric or antisymmetric combination of these. However, if the wave vector $\mathbf{k}$ lies on the $\Gamma - \mathrm{K}$ line it is unchanged under mirror reflection, $\mathbf{k} = \mathbf{k}^\star$, and the sub-lattice symmetry becomes the symmetry of each mode on this line. Hence, on the Γ-to-K line, each mode must be either symmetric or

antisymmetric under the mirror reflection: $\mathbf{E_k}(\mathbf{r}^\star) = \pm\mathbf{E_k}(\mathbf{r})$. Using FEM modeling we find that the upper modes near the Dirac points are anti-symmetric (Fig. 4.10) and, thus, their Fourier transform is zero in the 1st BZ as two sub-lattices give contributions of the opposite sign.

4.1.3 Tuning of Parameters

The system under study is a dipole resonator. One can achieve a desired frequency and group velocity by tuning such system parameters as the length of the rods and the rod spacing. With increasing rod length and keeping the same lattice constant the modes are shifted down as shown in Fig. 4.11. Contrarily, if we decrease rod length, the resonance frequency will shift up, above the light line, resulting in no Dirac crossing under the light line. By adjusting the ratio of the rods length to the lattice constant one can control the number of modes and presence of Dirac crossings below the light line.

Let us consider a sample made with 30 mm rods and with the nearest rod distance of 5 mm. The resonance frequencies of an individual rod are located at approximately 5 GHz, 10 GHz, 15 GHz, etc. For $a = 5$ mm the corner of the BZ is located at $K_{bz} = 4\pi/3\sqrt{3}a = 483\ m^{-1}$. The frequency of the free space radiation at a given k value is given by $f = ck/2\pi$. For $K_{bz} = 483$ m^{-1} the frequency of free space radiation is $f = 23.1$ GHz. This means that there should be four Dirac crossings below the light line. Indeed, we obtain four crossings located around 4.5 GHz, 9 GHz, 13.5 GHz, and 18 GHz as can be seen from Fig. 4.11.

Results of The COMSOL Multiphysics® modelling with parametric sweep of the rods length and fixed lattice constant are presented in Fig. 4.12. Rod length varies from 5 mm to 15 mm with 2 mm steps. With the rods increase in length the Dirac crossings frequency decreases as evident from Fig. 4.12. In Fig. 4.12a the dispersion diagram is plotted for various rod length, and in

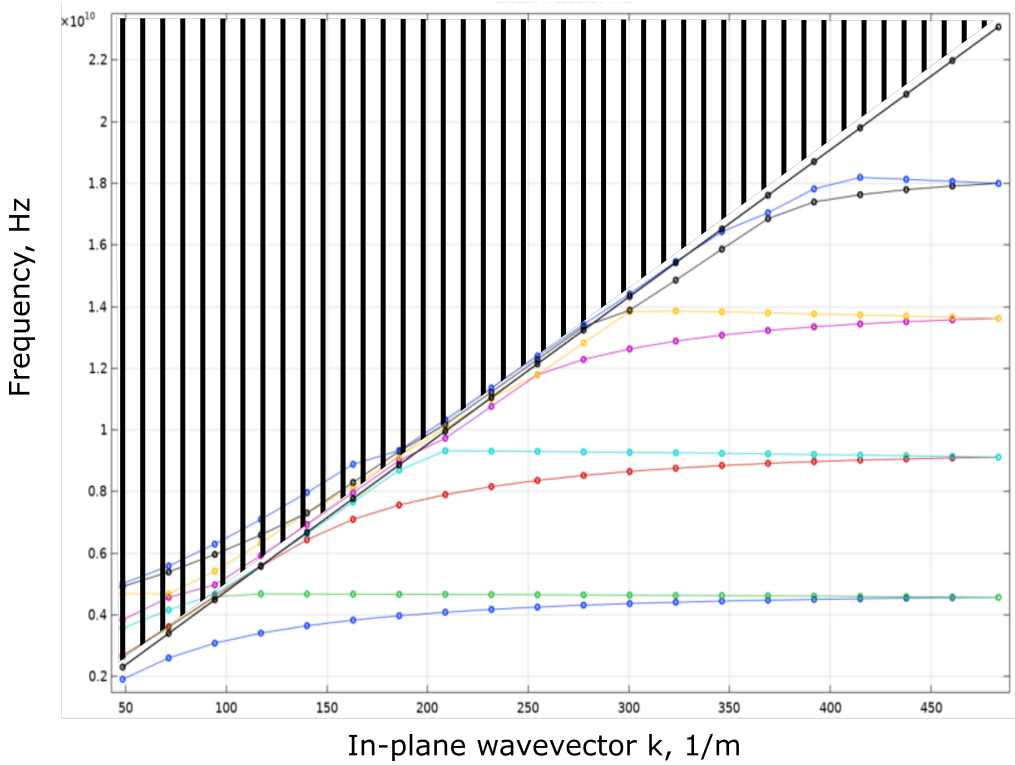

Figure 4.11: Modelled dispersion of bound surface waves for a sample comprised of $l = 30$ mm rods and rod spacing $a = 5$ mm. The region above the light line is shaded as it is not of interest for this study.

Fig. 4.12b the dependence of the first Dirac crossing is plotted against the rod length.

Let us now vary the lattice constant and observe how the mutual coupling between the rods affects the resonance frequency and the Dirac point locations. In Fig. 4.13 we plot the results of nine models with the rod spacing changing from 3 mm to 11 mm with a 1 mm step. The frequency decreases with the increasing distance between the rods and varies from 12.8 GHz for 3 mm spacing to 9.1 GHz for 11 mm spacing.

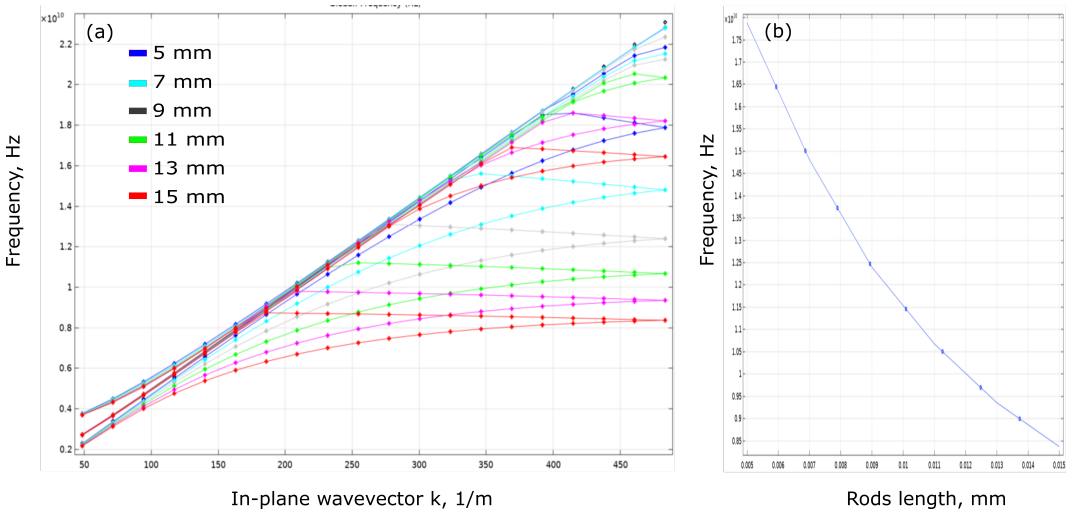

Figure 4.12: Modelling results for various rods length with fixed lattice constant. Rods length varies from 5 mm to 10 mm with a 2 mm step. (a) Dispersion diagram from Γ to K . (b) Changes of the Dirac frequency of the lower branch mode with the rods length variation.

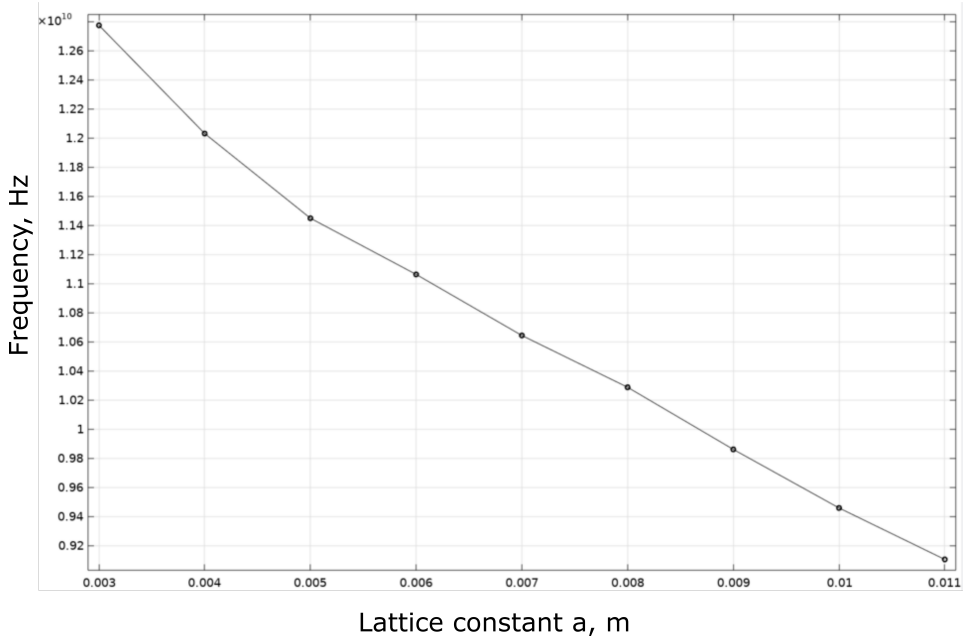

Figure 4.13: Dependency of the Dirac frequency of the lower branch on the rod spacing. With lattice constant increase from 3 mm to 11 mm the Dirac frequency falls from 12.8 GHz to 9.1 GHz.

4.2 Electric Field at High Symmetry Points

In this section we demonstrate a technique for measuring local fields and matching them to specific points in the reciprocal space. For comparison purposes, results from FEM will be provided together with the experimental data.

There are two distinct modes at the M point of the BZ for the lower dispersion branch ($K_M = \frac{2\pi}{3a}$). For $a = 5$ mm the M point has the following values of the wave vector $k_x = 418$ mm^{-1} and $k_y = 0$ mm^{-1} meaning that the waves are propagating strictly in the x direction. Thus, the scanning should be chosen also be in the x direction with respect to the hexagonal lattice. Frequencies of the modes at the M points can be obtained from the dispersion plots of Fig. 4.2: $f_1 = 8.2$ GHz and $f_2 = 8.5$ GHz.

Measurements of the magnitude of the electric field are presented in Fig. 4.14a and Fig. 4.14c. The area of four unit cells was scanned with a 0.2 mm step size to achieve a higher spatial resolution. One can reasonably expect to observe two standing waves at the edge of the BZ at the M point with the wavelength equal to $\lambda = 2\pi/K_M = 15$ mm and with the wave nodes shifted in real space by $\frac{\lambda}{4}$. Let us examine the obtained field distribution of the lower mode (Fig. 4.14 (a, b)). It can be seen that experimental and modelling results are in a good agreement with each other. The wavelength calculated from the plotted field profiles is equal to 15 mm with the minimum of the field located in between the rods. Let us also examine the obtained field profiles of the upper mode, (Fig. 4.14 (c, d)). As noted earlier, the spatial distribution of the wave field should be shifted by $\frac{\lambda}{4}$ with the minimum of the electric field pinned to the metallic rods edges. This explains the peculiar curly shape of the upper mode fields.

At the K point there are also two solutions which are degenerate. Therefore, only one field distribution plot will be presented below. One can choose K point

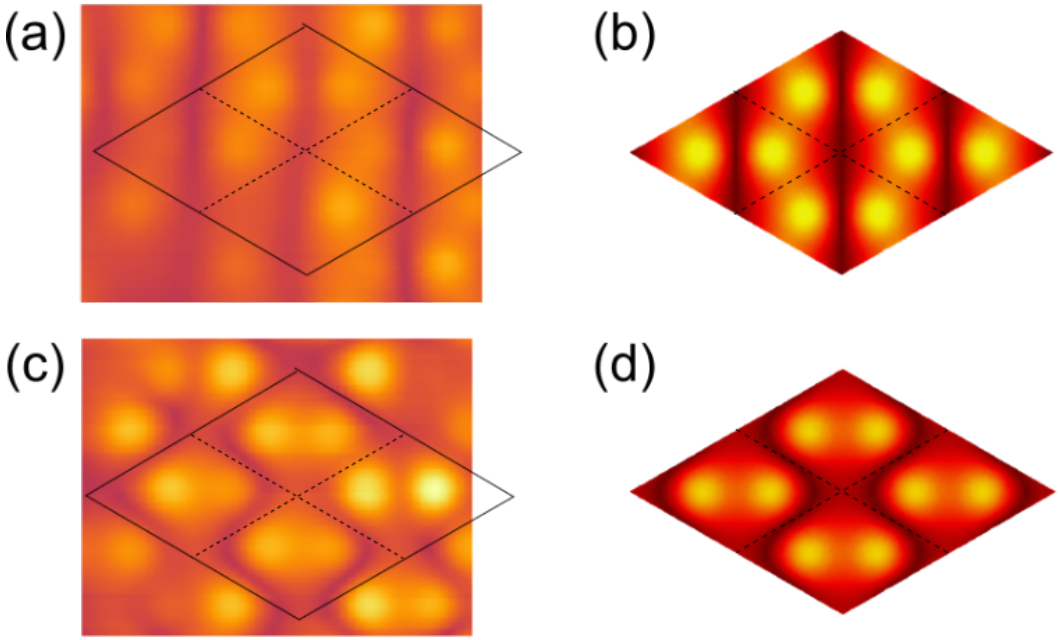

Figure 4.14: Normal component of the electric field above the surface for two standing wave solution at the M point. Dashed lines show unit cells boundaries. (a) and (c) Experimental results; (b) and (d) Modelling results. Two standing waves are shifted with respect to each other by $\frac{\lambda}{4}$

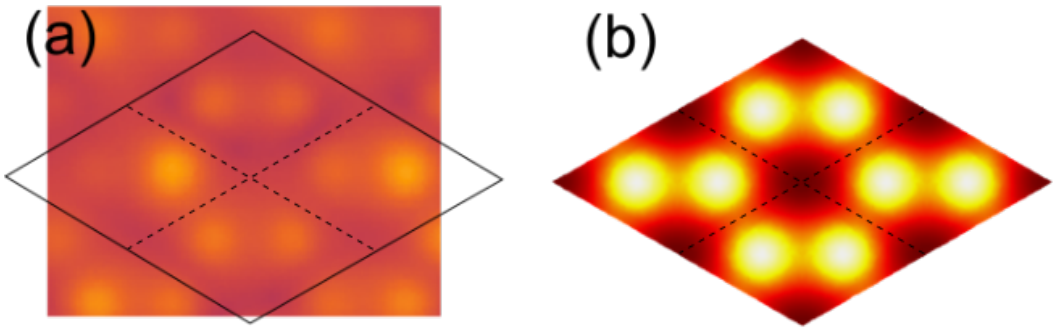

Figure 4.15: Normal component of the electric field above the surface for the K point. Dashed lines show unit cells boundaries. (a) Experimental results. (b) Modelling results.

in BZ which only has y component wavelength and thus the scanning area should be chosen in the y direction. The Dirac frequency of $f_{D1} = 8.325$ GHz was scanned. As before, experimental data is a good match with the modelling results (Fig. 4.15).

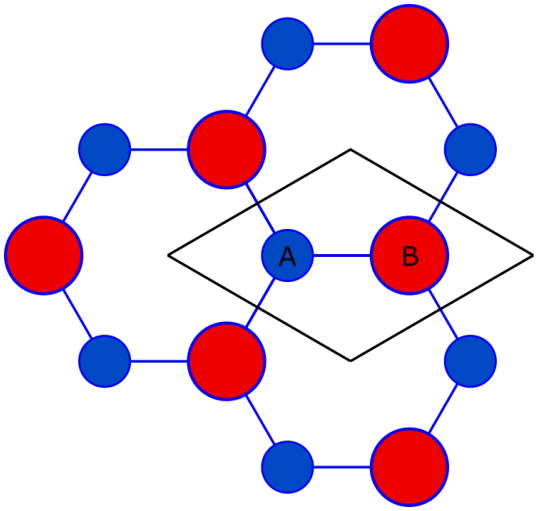

Figure 4.16: Honeycomb structure where sub-lattice A of the studied artificial graphene system is different from the sub-lattice B.

4.3 Breaking Inversion Symmetry

Dirac dispersion is a unique feature of graphene. Attention of the scientific community has turned to graphene as one of the potential candidates to replace silicon-based electronics as it possesses high mobility charged carriers. Nevertheless, a non-zero band gap is required to enable the on-off transistor behaviour [119, 120]. Several approaches which allow one to manipulate graphene band gap have been suggested and studied. Namely, substrate effects [121, 122], dopings [123], sub-lattice symmetry breaking, and many other techniques [124, 125] can be used to create a band gap at the the Direct crossings.

Many of these manipulations are either difficult or even impossible to implement in real graphene. However, such experiments can be easily performed for electromagnetic waves at microwave frequency in the AG system. In this section we will show modelling results for breaking graphene inversion symmetry through making rods in the first graphene sub-lattice thicker than in the second sub-lattice. By introducing asymmetry in the two graphene sub-lattices (see Fig. 4.16) we immediately break the six fold symmetry and thus a band

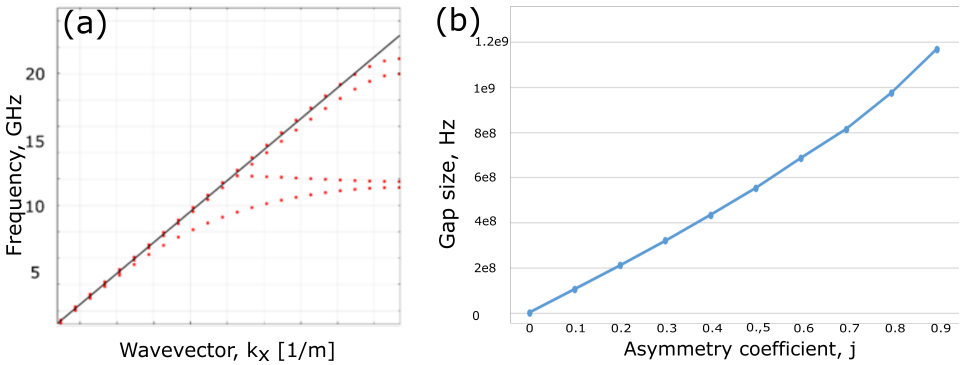

Figure 4.17: (a) Modelled dispersion relationship for the system with differing "atoms" in the two sub-lattices (one rod is thicker than another). The broken inversion symmetry causes the gap opening at K point. (b) Gap size introduced by breaking inversion symmetry depending on the asymmetry of the rods in two sub-lattices, where 0 corresponds to identical rods, and 1 corresponds to one rod being twice as thick as another.

gap opens. The modelled dispersion is plotted in Fig. 4.17a. One can see that at the K point there is no degeneracy anymore, the Dirac crossing is destroyed with the two modes splitting to form a band gap. The size of the created gap is proportional to the strength of the distortion, the bigger the asymmetry, the bigger is the created band gap (Fig. 4.17b).

By plotting mode fields in the proximity of one of the K points one can notice that the two modes are localised either on one or other sub-lattice. This is a known phenomena, when previously degenerate modes mix with each other in the vicinity of the K point and thus split to localise on the two non-equivalent sub-lattices [126].

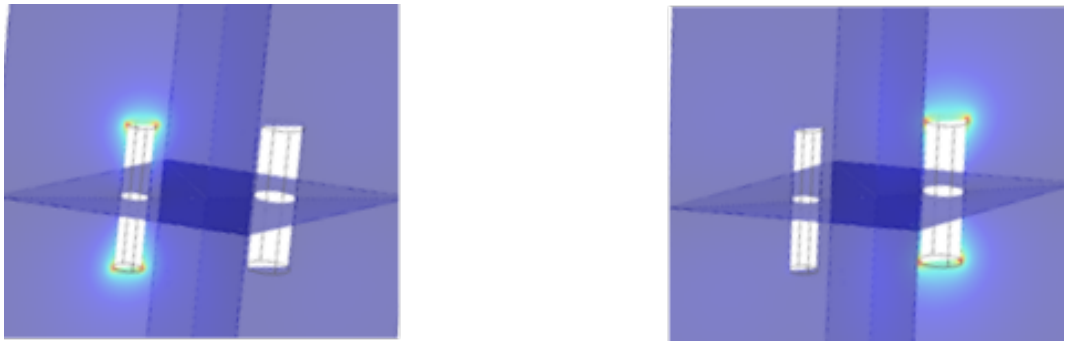

Figure 4.18: Mode mixing in presence of the broken inversion symmetry. Distribution of the electric field of the upper and lower modes along the rods length. In the vicinity of the K point the modes are localised on one of the graphene sub-lattices.

4.4 Conclusions

In conclusion, we have fabricated artificial hexagonal mesh graphene made of metallic rods arranged in a honeycomb array and experimentally measured the confined eigenmodes supported. We have determined the dispersion curves of this system and have shown two linear crossings at the K points of the hexagonal BZ, mimicking the well-celebrated Dirac cones in graphene. The presence of two Dirac points arises from two different modes supported by the individual rods.

The Dirac point positions and the slope of the crossings can be controlled by changing the structure parameters, i.e. honeycomb period and rod dimensions [95, 127, 128]. Results of the numerical modelling of various parameters variations were presented.

Manipulation of a system band structure can be used for engineering new materials which do not occur naturally but possess properties required for specific applications [127, 129]. In the studied case of artificial rodded graphene, we showed that destroying the inversion symmetry between its two sub-lattices results in a band gap opening at the Dirac crossings. We note that it is rather challenging to create a band gap for real graphene but it is easily achievable in the artificial system such as that presented in this work where the lattice

is created in an “atom-by-atom” manner. Therefore, it should be possible to construct 2D waveguides for supported electromagnetic waves by combining gapless artificial graphene and the graphene structure with a purposely created band gap [130].

CHAPTER 5

HEXAGONAL MESH ARTIFICIAL GRAPHENE

In this chapter we study the band structure of bound electromagnetic modes supported by a plane, hexagonal, assumed perfectly-conducting metal mesh. Contrary to previously considered electromagnetic graphene systems [98, 104, 131], our mesh has an exceedingly large ratio of in-plane to out-of-plane dimensions (lattice constant / wire thickness ≈ 200), which is even higher than graphene itself. Metallic wires play the role of bonding terms between sites on the hexagonal lattice. Such structure allows for a simple analytic treatment using electric circuit theory and we demonstrate its benefits for predicting and analysing various graphene-like phenomena. The developed electric circuit model is validated by comparing modelling result with experimentally measured dispersion curves of the bound electromagnetic waves at microwave frequencies. We then demonstrate how an effective uniaxial strain can be induced in the artificial hexagonal mesh graphene by modifying its lattice structure but without physically straining the system. Dispersion curves of the surface waves supported by artificially strained artificial hexagonal mesh graphene are calculated.

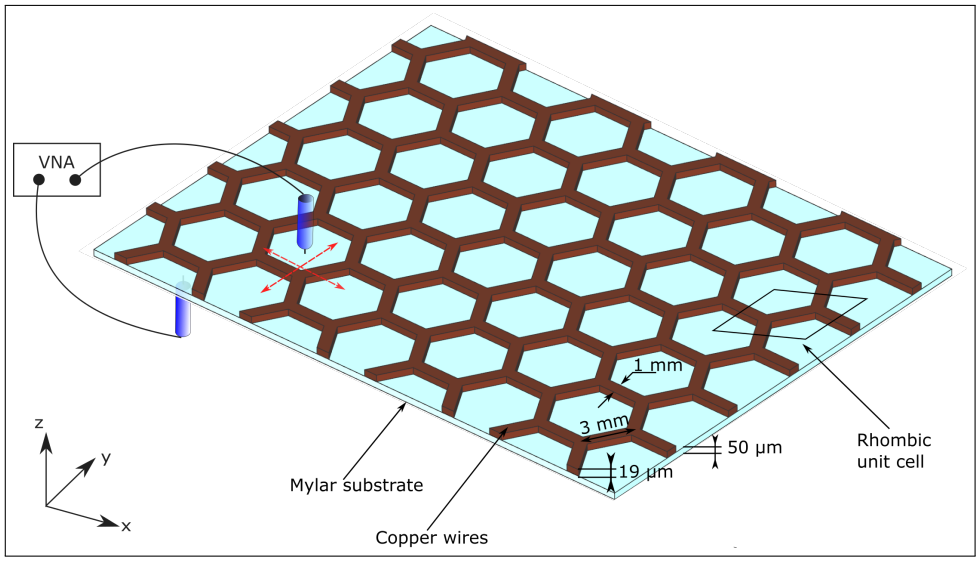

Figure 5.1: Schematic representation of the sample studied. It is a copper hexagonal mesh 19 μm thick on a dielectic substrate 50 μm thick. The length and width of the wire interconnects are 3 mm and 1 mm respectively. Source and detection antennas are positioned on opposite sides of the sample and connected to a VNA. Red dashed arrows indicate scanning directions of the detecting probe.

5.1 Dispersion of Surface Waves

The sample was fabricated via conventional lithographic techniques. The hexagonal pattern was etched into a 19 μm-thick copper layer on a 50 μm thick dielectric substrate. The sample comprises approximately 5000 hexagons of side length $a = 3$ mm and wire width $d = 1$ mm (see Fig. 5.1).

Electromagnetic modes within the sample are excited and detected using a pair of stripped-end coaxial cables as near-field antennas, each connected to a port of a microwave vector network analyser (VNA). Both antennas are placed with their coaxial axes normal to the sample surface with the metal tips approximately 0.5 mm away from the surface. Source and detection antennas are positioned on opposite sides of the sample to limit direct coupling between them. The detecting probe is raster scanned in the x and y directions across the sample surface with 1 mm step-spacing. The amplitude and relative phase of the local electric field (predominantly the z-component, due to the orientation

of the antenna) is measured at each spatial coordinate over a frequency range of 1 to 35 GHz, in 25 MHz steps. A Fast Fourier Transform (FFT) is then applied to the measured field-data in space to give a 2D map of the modes in the momentum space, (k_x, k_y) (equi-energy contours). Combining such curves for different frequencies produces the full mode-dispersion.

The measured band structure of the system is plotted in Fig. 5.2. As can be seen, there are linear Dirac crossings at the corners of the BZ at the K and K′ points at a frequency of $f_D = 30$ GHz. The frequency of the Dirac crossings is defined by the parameters of the mesh and is dictated by the

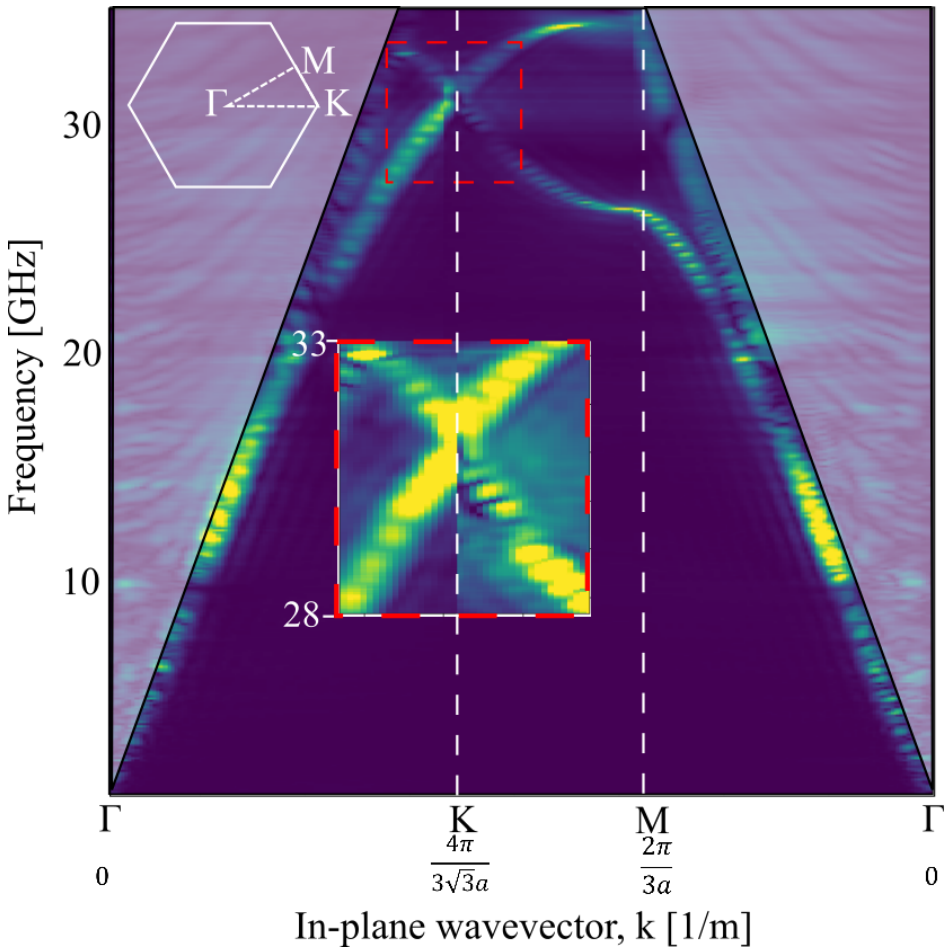

Figure 5.2: Dispersion of the electromagnetic bound modes supported by the wire-mesh sample, obtained by Fast Fourier Transform (FFT) of the measured near-field above the surface. Grayed triangular areas indicate the radiative region bound within the light cone. Inserted in the red dashed frame is a zoomed view of the area in the vicinity of the Dirac point, normalised to 1.

resonance frequency of the wires and will be discussed in the equivalent LC circuit section.

5.1.1 Iso-frequency Contours

The evolution of artificial hexagonal mesh graphene dispersion in the vicinity of the Dirac points is plotted in Fig. 5.3 for a range of frequencies from 27 GHz to 30 GHz. At the frequency of $f_D = 30$ GHz six Dirac points are located at the corners of BZ K-points. Away from the Dirac frequency the six crossing points evolve to iso-frequency curves of a circular shape. Starting from a frequency of $f = 29$ GHz, circular iso-frequency curves reshape to a trigonal profile. Six triangles are formed around the K-points, rotated by 60 deg in respect to each other. This deformation of iso-frequency circles into triangles at a certain distance away from the K-point is known as trigonal warping. This phenomena has been reported before in graphene and graphene-related structures, including multilayer graphene and nano-tubes [132–134]. It occurs because the band structure follows the symmetry of the crystal lattice [132]. This observation will be needed to explain some effects in Chapter 6.

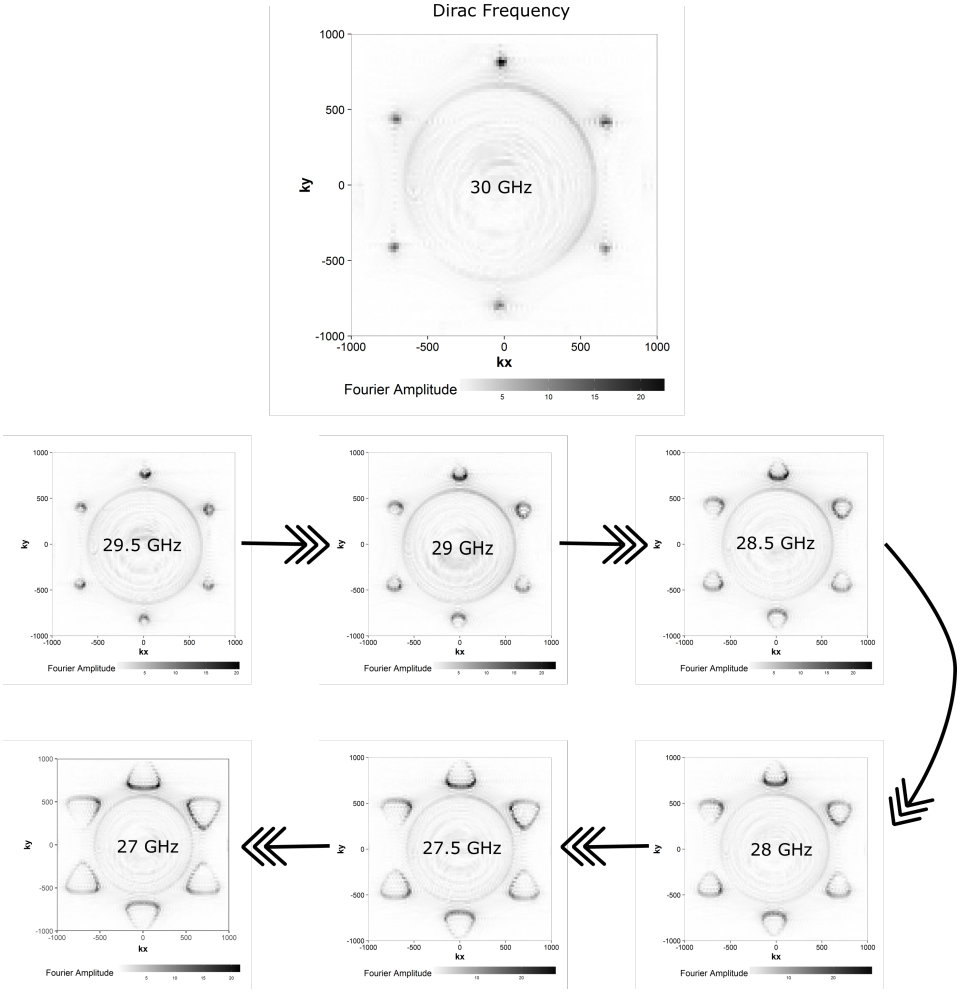

Figure 5.3: Evolution of the artificial hexagonal mesh graphene iso-frequency contours. Circular shape iso-frequency contours in the vicinity of the six Dirac points evolve into a trigonal shape.

5.1.2 Parameters Tuning

Let us model the dependence of Dirac frequency on the dimensions of the wire mesh which is forming the AG structure. In Fig. 5.5, we plot modelling results for a range of wire width w from 20 μm to 3 mm (Fig. 5.4). One can see that the Dirac frequency increases with increasing wire mesh width. The dependence of the Dirac frequency on the wire thickness is plotted in Fig. 5.6. The thicker the wires the higher is the frequency of the Dirac crossings. Thickness ranges from 20 μm to 8 mm. As will be shown below the frequency of the Dirac point purely depends on the wire dimensions, on the self- and cross- capacitance and

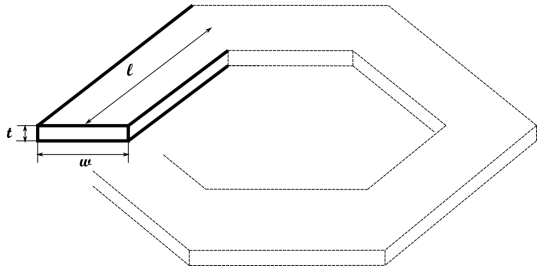

Figure 5.4: Sketch of cross-section of the wire forming the hexagonal mesh. l is length, w is width and t is thickness of wires.

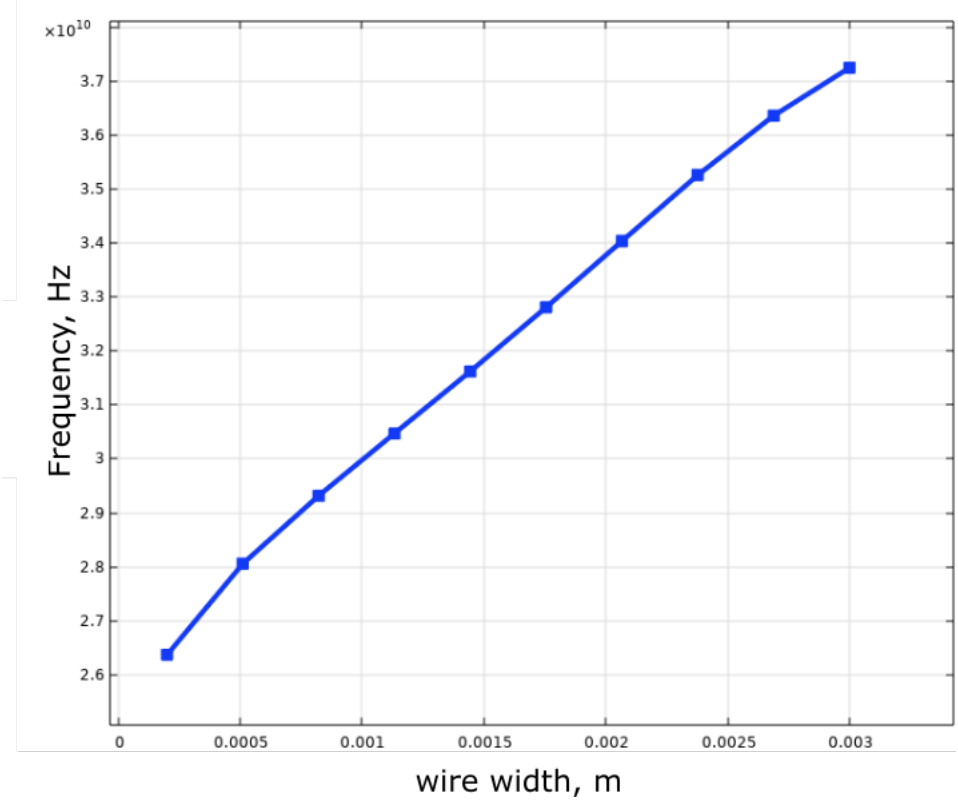

Figure 5.5: Dependency of the Dirac crossing of the artificial hexagonal mesh graphene on the width of the forming wires.

inductance of the wires, and thus varies with wire parameters in a non-trivial way.

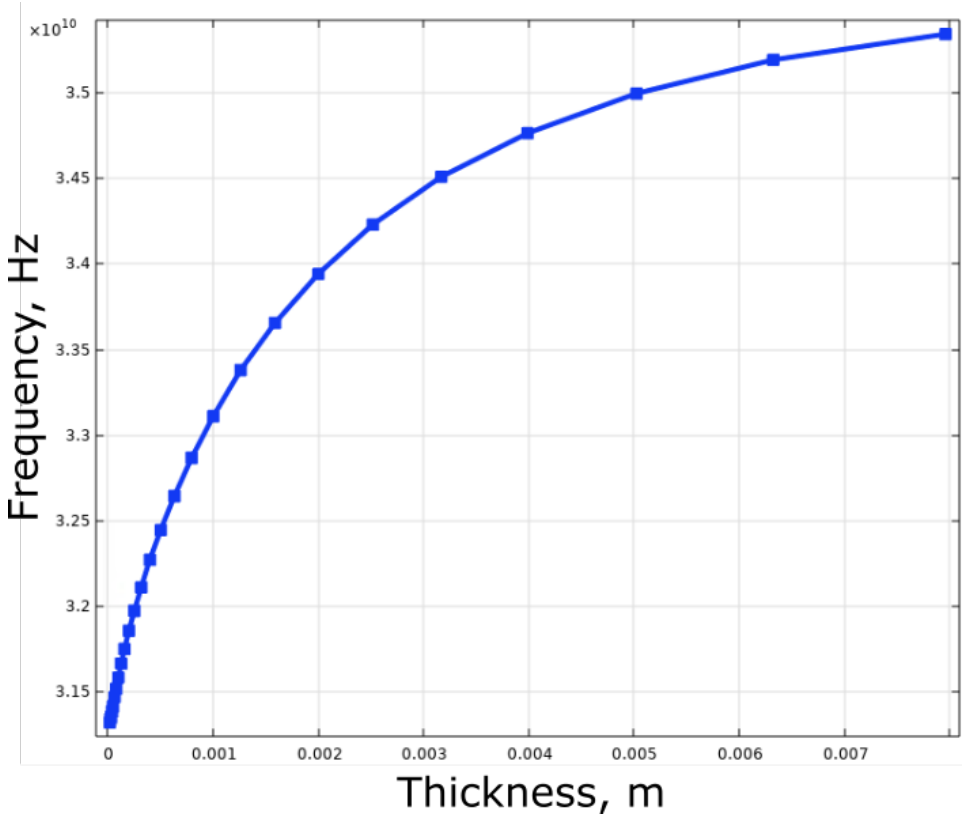

Figure 5.6: Dependency of the Dirac crossing of the artificial hexagonal mesh graphene on the thickness of the forming wires.

5.2 Equivalent *LC* Circuit Model

5.2.1 Minimal *LC* Model and Kirchhoff's Laws

The structure explored in this study is a simply connected hexagonal mesh formed by metallic wires. It may also be viewed as a triangular lattice with two Y-shaped elements per unit cell (see Fig. 5.7), each Y shaped element being equivalent to a carbon atom in graphene itself.

This system supports electric currents propagating in the wires, thus, it is possible to model the expected dispersion of the bound electromagnetic waves using electric circuit theory. Consider a minimal *LC* model which is capable of representing the electrodynamics of such a wire-based hexagonal mesh. The primary source of inductance and capacitance in the wire network is the self-inductance and self-capacitance of the wires. The units of capacitance and

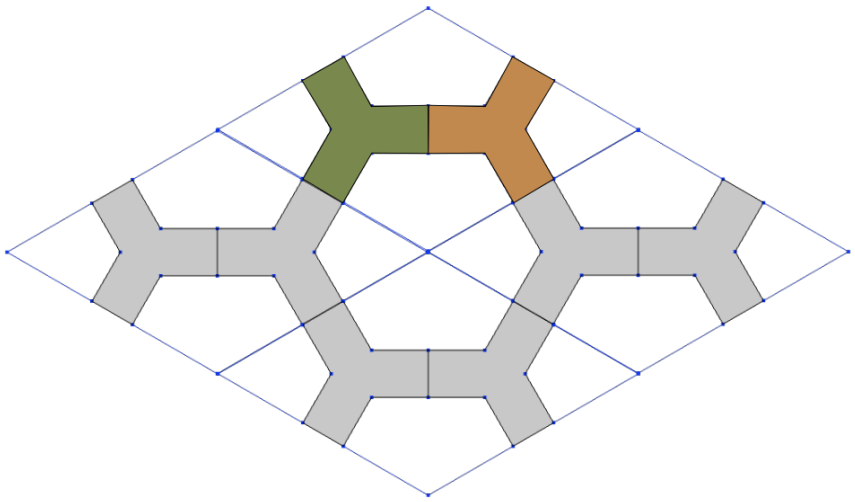

Figure 5.7: Unit cell of the hexagonal wire mesh. Triangular lattice with rhombic unit cell with two Y elements is shown.

inductance are proportional to units of length (via the electric ε_0, which has units of F/m and the magnetic constant μ_0 measured in H/m). Primarily, it is the charges in the wire network, which spread through the wires, rather than concentrated at junctions that dominate the behaviour. Later, we shall discuss why most of the other components are relatively unimportant.

We now construct a mathematical model for the minimal circuit. Let the voltage on each site shown in Fig. 5.8 be V_{X} where X is the site index. For a mode with Bloch wave vector $\mathbf{k} = (k_x, k_y)$ the voltages $V_{\mathrm{D}'}$ and $V_{\mathrm{E}'}$ can be obtained from the voltages on the sites D and E by applying respective translations by the relevant lattice vectors. It is convenient to introduce the translation factors for the Bloch mode which are defined by the equations below

$$\xi_{\mathbf{k}} \equiv exp\left(\frac{3i}{2}k_x a\right), \eta_{\mathbf{k}} \equiv exp\left(\frac{i\sqrt{3}}{2}k_y a\right), \tag{5.1}$$

where we assume the side of a hexagon to be a, it can be set to $a = 1$ in most of what follows. Using definitions of $\xi_{\mathbf{k}}$ and $\eta_{\mathbf{k}}$ we obtain

$$V_{\mathrm{D}'} = V_{\mathrm{D}}\xi_{\mathbf{k}}\eta^*_{\mathbf{k}}, V_{\mathrm{E}'} = V_E\xi_{\mathbf{k}}\eta_{\mathbf{k}}. \tag{5.2}$$

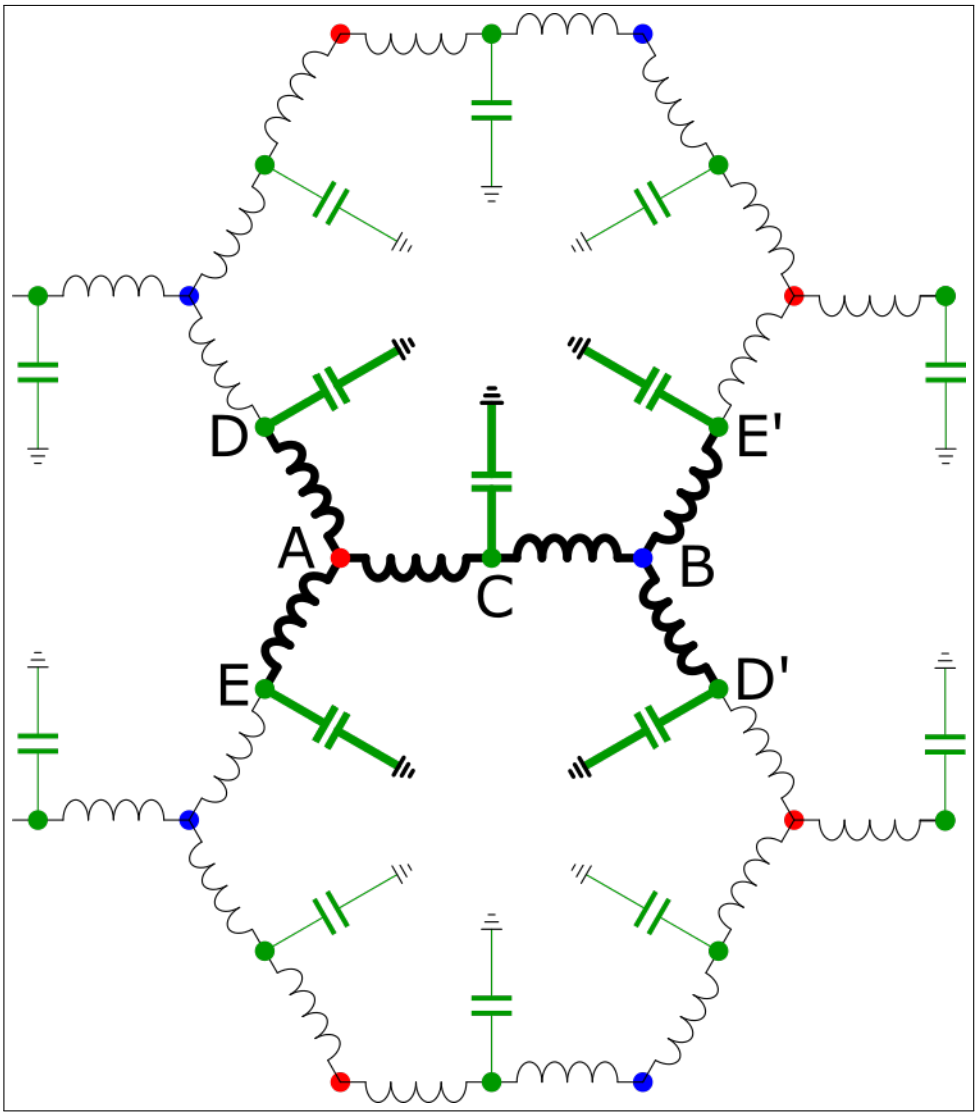

Figure 5.8: The equivalent LC circuit model for reproducing the electrodynamics of a artificial honeycomb mesh graphene. The unit cell is represented in bold.

The charges on the nodes C, D, and E are $Q_C = CV_C$, $Q_D = CV_D$, $Q_E = CV_E$, where C is the connector self-capacitance. Note that there is no charge accumulation on the A and B sites. The charges on the capacitors can change due to the current flowing through each link according to the standard capacitor

current-voltage relation

$$
\begin{aligned}
C\frac{dV_{\mathrm{C}}}{dt} &= J_{\mathrm{A}\to\mathrm{C}} + J_{\mathrm{B}\to\mathrm{C}},\\
C\frac{dV_{\mathrm{D}'}}{dt} &= J_{\mathrm{A}'\to\mathrm{D}'} + J_{\mathrm{B}\to\mathrm{D}'},\\
C\frac{dV_{\mathrm{E}'}}{dt} &= J_{\mathrm{A}'\to\mathrm{E}'} + J_{\mathrm{B}\to\mathrm{E}'}.
\end{aligned}
\tag{5.3}
$$

In turn, the currents are related to the relevant voltage drops via Faraday's induction law and the definition of inductance as

$$
-L\frac{dJ_{\mathrm{A}\to\mathrm{C}}}{dt} = V_{\mathrm{A}} - V_{\mathrm{C}}, etc.
\tag{5.4}
$$

Sites A and B participate "passively" - the algebraic sum of currents entering these sites is zero, according to Kirchhoff's law:

$$
\begin{aligned}
J_{\mathrm{A}\to\mathrm{C}} + J_{\mathrm{A}\to\mathrm{D}} + J_{\mathrm{A}\to\mathrm{E}} &= 0,\\
J_{\mathrm{B}\to\mathrm{C}} + J_{\mathrm{B}\to\mathrm{D}'} + J_{\mathrm{B}\to\mathrm{E}'} &= 0.
\end{aligned}
\tag{5.5}
$$

There are five voltages and six currents in each elementary cell. They are restricted by the two periodicity conditions, three equations for capacitors, four equations for the inductances, and two current conservation equations. This comprises eleven equations for eleven unknowns, hence the equations given above are sufficient to determine current and voltage dynamics.

To simplify this system of equations it is convenient to introduce flux variables $\Phi_{\mathrm{A}}, \Phi_{\mathrm{B}}$, etc., which are defined as $V_{\mathrm{A}} = -d\Phi_{\mathrm{A}}/dt$. These flux variables represent the line integral $\int \boldsymbol{A}\cdot d\boldsymbol{l}$ taken over the line passing through each circuit component where $\boldsymbol{A}$ is the vector potential. In particular, the flux across an inductor is given by the difference of flux variables between its terminals. One can write $LJ_{\mathrm{A}\to\mathrm{C}} = (\Phi_{\mathrm{A}} - \Phi_{\mathrm{C}})$, etc. In these variables, current conservation equations take the following form

$$
\begin{aligned}
\frac{\Phi_{\mathrm{C}} - \Phi_{\mathrm{A}}}{L} + \frac{\Phi_{\mathrm{D}} - \Phi_{\mathrm{A}}}{L} + \frac{\Phi_{\mathrm{E}} - \Phi_{\mathrm{A}}}{L} &= 0,\\
\frac{\Phi_{\mathrm{C}} - \Phi_{\mathrm{B}}}{L} + \frac{\Phi_{\mathrm{D}'} - \Phi_{\mathrm{B}}}{L} + \frac{\Phi_{\mathrm{E}'} - \Phi_{\mathrm{A}}}{L} &= 0
\end{aligned}
\tag{5.6}
$$

Hence, it is possible to exclude the variables Φ_A and Φ_B by expressing the flux variables through each other

$$\begin{aligned} \Phi_A &= \frac{1}{3}[\Phi_C + \Phi_D + \Phi_E], \\ \Phi_B &= \frac{1}{3}[\Phi_C + \Phi'_D + \Phi'_E]. \end{aligned} \tag{5.7}$$

One can also express the currents in terms of three flux variables. This gives the following equations for the sum of the currents at the points C, D, and E. For the current entering the node C we find

$$\begin{aligned} J_C = J_{A\to C} + J_{B\to C} = \frac{1}{L}[-\Phi_A - \Phi_B + 2\Phi_C] = \\ = \frac{1}{3L}[4\Phi_C - (1+\xi_{\mathbf{k}}\eta^*_{\mathbf{k}})\Phi_D - (1+\xi_{\mathbf{k}}\eta_{\mathbf{k}})\Phi_E], \end{aligned} \tag{5.8}$$

where $\eta_{\boldsymbol{k}}$ and $\xi_{\boldsymbol{k}}$ are the translation factors for the Bloch mode defined by Eq. (5.1). For the current entering the node E′ we find

$$J_{E'} = J_E \xi_{\mathbf{k}}\eta_{\mathbf{k}} = -\frac{1}{L}[\xi_{\mathbf{k}}\eta_{\mathbf{k}}\Phi_A + \Phi_B - 2\Phi_{E'}]. \tag{5.9}$$

A similar calculation yields the following expressions for the currents which are entering nodes E and D

$$J_E = \frac{1}{3L}[-(1+\xi^*_{\mathbf{k}}\eta^*_{\mathbf{k}})\Phi_C - (1+(\eta^2_{\boldsymbol{k}})^*)\Phi_D + 4\Phi_E], \tag{5.10}$$

$$J_D = \frac{1}{3L}[-(1+\xi^*_{\mathbf{k}}\eta_{\mathbf{k}})\Phi_C - (1+\eta^2_{\boldsymbol{k}})\Phi_E + 4\Phi_D]. \tag{5.11}$$

Additionally, the current J_C is given by $J_C = C\dot{V}_C = -C\ddot{\Phi}_C$. For a mode with frequency ω, this quantity can be replaced with $C\omega^2\Phi_C$. Thus, the dynamics of the modes can be determined from the following system of three equations

$$\begin{aligned} C\omega^2\Phi_C = J_C &= \left[4\Phi_C - (1+\xi_{\mathbf{k}}\eta^*_{\mathbf{k}})\Phi_D - (1+\xi_{\mathbf{k}}\eta_{\mathbf{k}})\Phi_E\right]/3L, \\ C\omega^2\Phi_D &= \left(-(1+\xi^*_{\mathbf{k}}\eta_{\mathbf{k}})\Phi_C - (1+(\eta^2_{\mathbf{k}}))\Phi_E + 4\Phi_D\right)/3L, \\ C\omega^2\Phi_E &= \left(-(1+\xi^*_{\mathbf{k}}\eta^*_{\mathbf{k}})\Phi_C - (1+(\eta^2_{\mathbf{k}})^*)\Phi_D + 4\Phi_E\right)/3L. \end{aligned} \tag{5.12}$$

These equations define an eigenvalue problem that can be easily solved to yield the dispersion of the modes supported by the hexagonal wire mesh, either

numerically or analytically. The square of the frequency ω^2 is the eigenvalue to be found, and the flux variables (or potentials) on the sites C, D, and E form an eigenvector for each normal mode.

Before solving this problem we will introduce another way of deriving the same set of equations which is useful for analysing more complex circuits.

5.2.2 Energy Contributions and Lagrangian Approach

In a more general case the left hand side of Eq. (5.12) can be recast in a matrix form as $\widehat{\mathscr{C}}(\mathbf{k})\omega^2\Phi$, where $\widehat{\mathscr{C}}(\mathbf{k})$ is the capacitance matrix, and $\Phi = (\Phi_C, \Phi_D, \Phi_E)$ is the vector formed by the flux variables. The right-hand side is $\widehat{\mathscr{L}}(\mathbf{k})\Phi$, where the elements of the matrix $\widehat{\mathscr{L}}$ represent inductances. Hence, the vector formed by the flux variables must satisfy the equation below

$$\omega^2(\mathbf{k})\widehat{\mathscr{C}}(\mathbf{k})\Phi(\mathbf{k}) = \widehat{\mathscr{L}}(\mathbf{k})\Phi(\mathbf{k}). \tag{5.13}$$

Such an equation defines a generalised eigenvalue problem. The dispersion $\omega(\mathbf{k})$ can be found from the characteristic equation

$$\det[\widehat{\mathscr{C}}(\mathbf{k})\omega^2 - \widehat{\mathscr{L}}(\mathbf{k})] = 0. \tag{5.14}$$

Instead of deriving the matrices $\widehat{\mathscr{L}}(\mathbf{k})$ and $\widehat{\mathscr{C}}(\mathbf{k})$ from Kirchhoff's laws, one can analyse the capacitive and inductive contributions to the energy, W_E and W_M. The former contribution is of the form of $\frac{1}{2}V^*\widehat{\mathscr{C}}(\mathbf{k})V$, where the potentials $V = -\dot{\Phi}$ while the latter is given by $\frac{1}{2}\Phi^*\widehat{\mathscr{L}}(\mathbf{k})\Phi$. For the minimal circuit, the energy of the capacitors is simply the sum of energies stored in each capacitor

$$W_{\mathrm{E}} = \sum \frac{C_i V_i^2}{2} = \frac{C}{2}\left[|\dot{\Phi}_{\mathrm{C}}^2| + |\dot{\Phi}_{\mathrm{D}}^2| + |\dot{\Phi}_{\mathrm{E}}^2|\right] \tag{5.15}$$

The magnetic energy stored in each inductor is given by $\frac{1}{2}L_i J_i^2 = \Phi_i^2/(2L)$. Hence for the minimal LC circuit we can write

$$W_M = \frac{1}{2L}[(\Phi_{\mathrm{A}} - \Phi_{\mathrm{C}})^2 + (\Phi_{\mathrm{A}} - \Phi_{\mathrm{D}})^2 + (\Phi_{\mathrm{A}} - \Phi_{\mathrm{E}})^2 + (\Phi_{\mathrm{B}} - \Phi_{\mathrm{C}})^2 + (\Phi_{\mathrm{B}} - \Phi_{\mathrm{D}'})^2 + (\Phi_{\mathrm{B}} - \Phi_{\mathrm{E}'})^2].$$

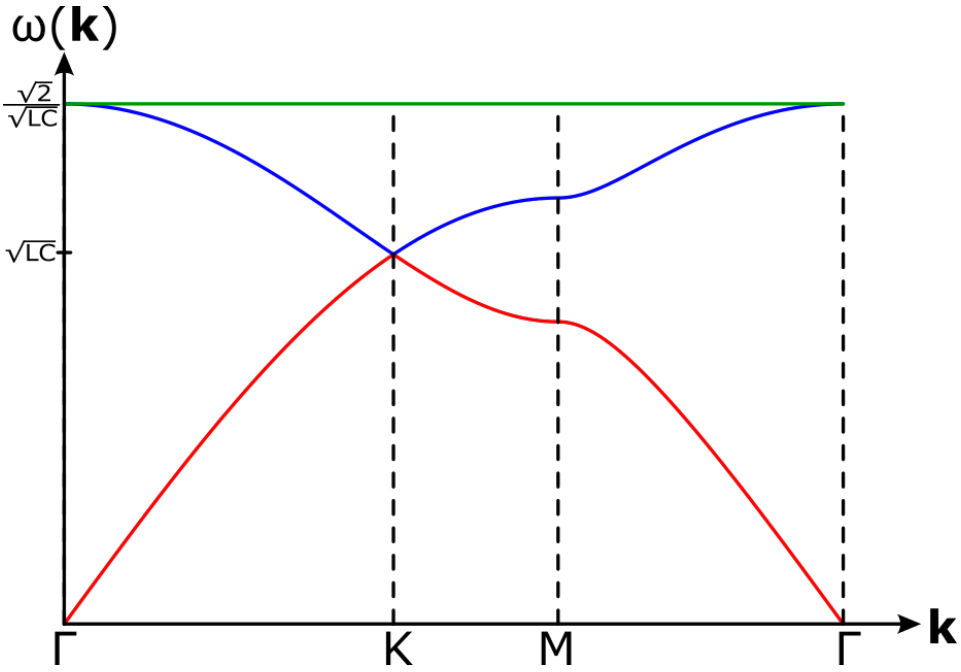

Figure 5.9: Dispersion relation obtained from the LC circuit model. The flat mode (green) is an artefact.

Note that Eq. (5.7) can be derived from the minimisation of the magnetic energy $\partial W_M/\partial \Phi_\mathrm{A} = 0$. Writing the energy in terms of Φ_C, Φ_D and Φ_E yields the following matrices for the minimal circuit

$$\widehat{\mathscr{C}}(\mathbf{k}) = C\begin{pmatrix} 1 & 0 & 0 \\ 0 & 1 & 0 \\ 0 & 0 & 1 \end{pmatrix}, \quad \widehat{\mathscr{L}}(\mathbf{k}) = \frac{1}{3L}\begin{pmatrix} 4 & -(1+\xi_k\eta_k^*) & -(1+\xi_k\eta_k) \\ -(1+\xi_k^*\eta_k) & 4 & -(1+\eta_k^2) \\ -(1+\xi_k^*\eta_k^*) & -(1+(\eta_k^2)^*) & 4 \end{pmatrix}$$

Once the matrices for the two energy contributions are known, one can construct Lagrangian $\mathscr{L} = W_E - W_M$. The Lagrangian is equivalent to that of a system of coupled oscillators with the mass matrix given by $\widehat{\mathscr{C}}(\mathbf{k})$ and the spring constant matrix given by $\widehat{\mathscr{L}}(\mathbf{k})$. This leads straightforwardly to the eigenvalue problem of Eqs (5.13) and (5.14) described above. For the matrices $\widehat{\mathscr{L}}$ and $\widehat{\mathscr{C}}$ which are given, this reproduces Eq. (5.12).

The system of equations and the eigenvalue problem can be solved numerically using a convenient mathematical package. The Python programming

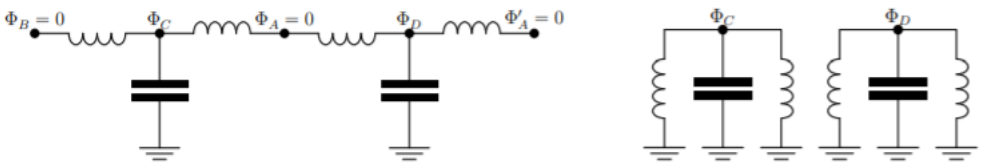

Figure 5.10: Decoupled LC circuits. This model explains zero gradient mode, an artefact of the minimum LC circuit model.

language with Numpy package was used for this purpose. Jupiter Notebook was used as an Integrated Development Environment (IDE).

Let us discuss the obtained mode dispersion that is plotted in Fig. 5.9. First, one can notice the presence of an unusual flat (zero gradient) branch at the highest frequency (green line). The origin and structure of this mode can be explained as follows. Let us assume that the flux variables Φ_{C}, Φ_{D}, $\Phi_{\mathrm{D}'}$, Φ_{E}, and $\Phi_{\mathrm{E}'}$ are arranged in such a way so that they cancel the flux variables Φ_{A} and Φ_{B} (and hence the voltages on all A and B sites). If this is indeed the case, full decoupling should occur as capacitors are only connected to each other via A and B sites. In the configuration in which $\Phi_{\mathrm{A}} = \Phi_{\mathrm{B}} = 0$ each capacitor is effectively discharged to the ground via the two parallel inductances, see Fig. 5.10. In other words, in the analysis of the flat-banded mode A and B can be replaced with a virtual ground. This is equivalent to an array of decoupled LC-circuits, each of inductance $L/2$ and capacitance C, which gives the degenerate resonant frequency $\sqrt{2}\Omega_0 = \sqrt{2/LC}$.

For the other two modes in Fig. 5.9, the dispersion is obtained by diagonalizing the eigenvalues equations. This gives

$$\omega^2(\mathbf{k}) = \frac{\Omega_0^2}{3}\left(3 \pm \left|2\cos\left(\frac{\sqrt{3}}{2}k_y a\right) + \exp\left(\frac{i3}{2}k_x a\right)\right|\right), \tag{5.16}$$

where k_x and k_y are the components of the wave vector, and a is the side of the hexagon. Unsurprisingly, this reproduces the dispersion law for electrons in graphene found using the framework of the TB model [97]. Similarly to the real graphene and other artificial graphenes, Dirac crossings at K and K′ points are

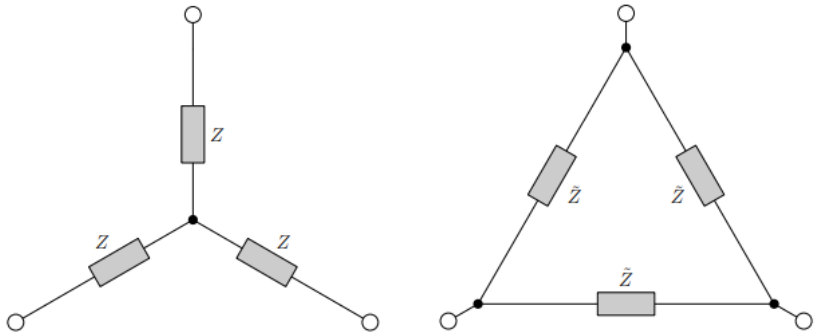

(a) (b)

Figure 5.11: The star (a) formed by the three impedances $Z(\omega)$ connecting three terminals can be transformed into a triangle (b) formed by impedances $\tilde{Z}(\omega)$ connecting the same terminals. For three equal impedances $\tilde{Z}(\omega) = 3Z(\omega)$.

a result of the lattice symmetry (i.e. two elements per unit cell in a hexagonal array). Near the Γ-point $\mathbf{k} \to 0$ and the above solution yields a linear dispersion $\omega(\mathbf{k}) = \Omega_0 a|\mathbf{k}|/2$. Positions of the Dirac points in the BZ are determined by requiring that the splitting between the modes vanishes. This condition gives $\boldsymbol{K} = (4\pi/3\sqrt{3}a, 0)$, $\boldsymbol{K}' = (-4\pi/3\sqrt{3}a, 0)$ with the frequency $\omega(\boldsymbol{K}) = \Omega_0 = 1/\sqrt{LC}$. Near each of the Dirac points one can expand the modulus in Eq. (5.16) as

$$|1 + 2cos\frac{k_y a\sqrt{3}}{2}\exp(3ik_x a/2)| \approx \frac{3a}{2}|\mathbf{k} - \mathbf{K}|. \tag{5.17}$$

This gives the following dispersion of the graphene modes in the vicinity of the Dirac points

$$\omega(\mathbf{k}) \approx \Omega_0 (1 \pm (|\mathbf{k} - \boldsymbol{K}|a)), \tag{5.18}$$

where the Dirac velocity is $\Omega_0 a/4$, one half of the velocity near the Γ-point.

Let us discuss several ways in which the model can be extended. Before doing this, however, it is helpful to recall the following fact from the circuit theory: a star formed by three impedances connected through the central point can be transformed to an equivalent triangle connecting the same vertices, and vice versa, as shown in Fig. 5.11. In the geometry of the graphene lattice this transformation makes several circuit configurations equivalent. For example, one can try to introduce link-to-link capacitance. The corresponding circuit is

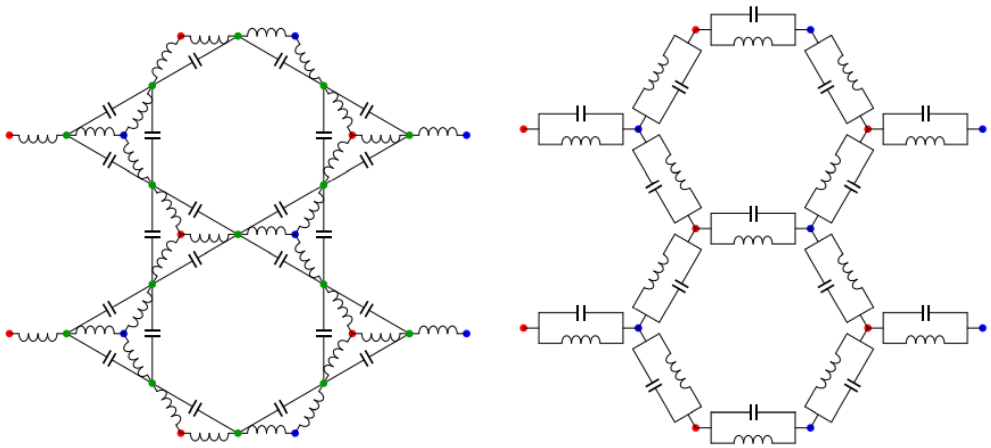

(a) (b)

Figure 5.12: (a) The circuit formed by link inductances and cross-capacitances. Each inductance is L, each capacitor is C_{cross}. (b) The circuit equivalent to the one shown in (a): each inductance is $2L$, each capacitor is $C_{cross}/2$.

shown in Fig. 5.12a with the mid-link capacitors removed. A detailed analysis shows that such a circuit has three degenerate and perfectly flat dispersionless modes of the frequency $1/\sqrt{LC_{cross}}$.

This can be explained by transforming triangles formed by the capacitors into stars as shown in Fig. 5.12b. The circuit is formed by connected elementary parallel LC-circuits. The impedance of the whole system being proportional to the impedance of a single elementary LC-circuit . Hence, the resonant frequencies of this whole network are given by the frequency of a single elementary LC-circuit.

It is now obvious that the circuit is formed from connected elementary parallel LC-circuits with the impedance of the whole system being proportional to the impedance of a single contour. Hence, the resonant frequencies of this network are given by the frequency of a single contour.

One could also introduce mutual inductances M between the links, however, these components would also contribute to the total link inductance while they do not contribute to the dispersion of the modes. This can be paraphrased as follows. All components that surround the sites of the triangular lattice can

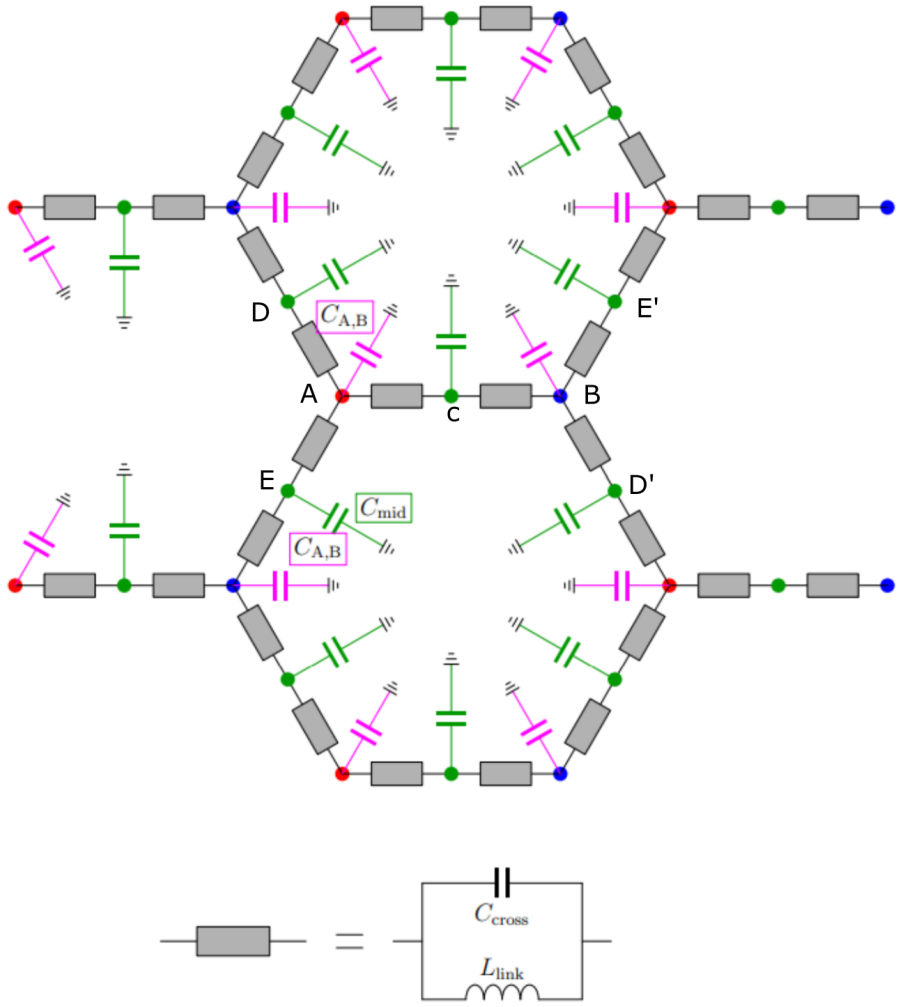

Figure 5.13: A more general circuit. Each link is represented via its inductance L_{link} and capacitance C_{cross}. The effect of mid-link capacitors C_{mid} (green) were discussed in the context of the minimal circuit model. The site capacitors $C_{\mathrm{A,B}}$ (magenta) make site potentials to be independent dynamic variables and hence result in two extra dispersion branches.

be transformed into their link-based counterparts, however, at the expense of making the link capacitance $L(\omega)$ frequency-dependent. These components do not contribute to the mode dispersion on their own. Hence one has to introduce extra components at the midpoints or on the A and B sites. It is natural to think of the latter as capacitors. Therefore, we arrive to a more general equivalent circuit shown in Fig. 5.13 in which the side capacitances $C_{\mathrm{A,B}}$ are included.

Without the site capacitors $C_{\mathrm{A,B}}$ the site fluxes and potentials were completely defined by the values at the midpoint, as given by Eq. (5.7). With

the site capacitors connected, the potentials on the sites become full-fledged dynamic variable which can be found from the equations of motion. The new circuit has five degrees of freedom and thus should support five modes.

The corresponding matrices of inductances and capacitances can be easily derived by analysing the energy. Let's us start with the magnetic contribution given by six inductances:

$$W_M = \frac{|\Phi_A - \Phi_C|^2}{2L} + \frac{|\Phi_A - \Phi_D|^2}{2L} + \frac{|\Phi_A - \Phi_E|^2}{2L} + \\ + \frac{|\Phi_B - \Phi_C|^2}{2L} + \frac{|\Phi_B - \Phi_{D'}|^2}{2L} + \frac{|\Phi_B - \Phi_{E'}|^2}{2L}. \tag{5.19}$$

The values of the flux variables at points D′ and E′ are given by the Bloch theorem. Expanding this expression and recasting it in a quadratic form, $W_M = \frac{1}{2}\Phi^* \hat{A}(k)\Phi$, one finds the following inverse inductance matrix

$$\widehat{\mathscr{L}}(k) = \frac{1}{L_{link}} \begin{pmatrix} 3 & 0 & -1 & -1 & -1 \\ 0 & 3 & -1 & -\xi_k \eta_k^* & -\xi_k \eta_k \\ -1 & -1 & 2 & 0 & 0 \\ -1 & -\xi_k^* \eta_k & 0 & 2 & 0 \\ -1 & -\xi_k^* \eta_k^* & 0 & 0 & 2 \end{pmatrix}$$

Similarly, the capacitive contributions to the energy are defined as shown below

$$W_E = \frac{C_{cross}}{2}\left\{ \left|\dot{\Phi}_A - \dot{\Phi}_C\right|^2 + \left|\dot{\Phi}_A - \dot{\Phi}_D\right|^2 + \left|\dot{\Phi}_A - \dot{\Phi}_E\right|^2 + \right. \\ \left. + \left|\dot{\Phi}_B - \dot{\Phi}_C\right|^2 + \left|\dot{\Phi}_B - \dot{\Phi}_{D'}\right|^2 + \left|\dot{\Phi}_B - \dot{\Phi}_{E'}\right|^2 \right\} + \\ + \frac{C_{A,B}}{2}\left\{ \left|\dot{\Phi}_A\right|^2 + \left|\dot{\Phi}_B\right|^2 \right\} + \frac{C_{mid}}{2}\left\{ \left|\dot{\Phi}_C\right|^2 + \left|\dot{\Phi}_D\right|^2 + \left|\dot{\Phi}_E\right|^2 \right\} \tag{5.20}$$

This finally gives the five-by-five capacitance matrix of the following form:

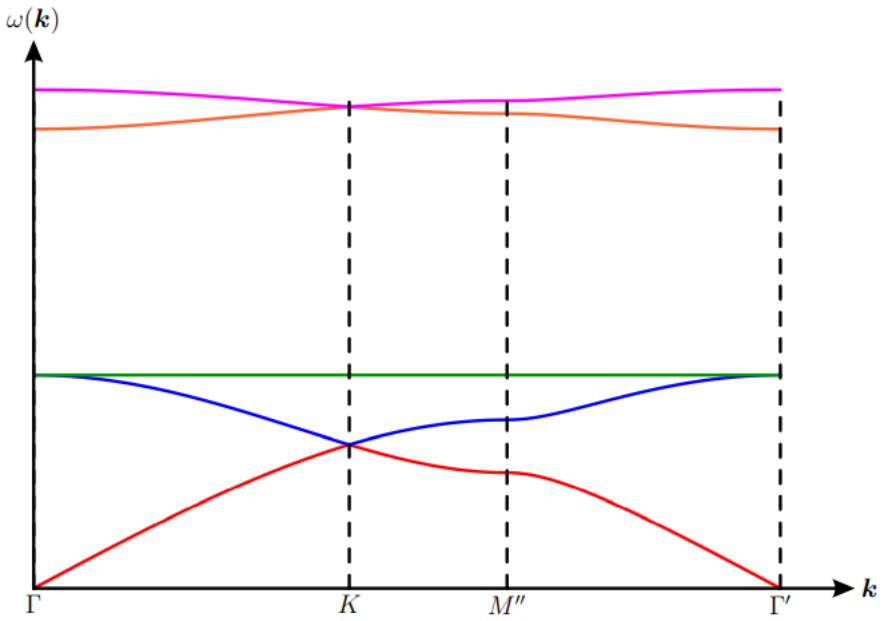

Figure 5.14: Modes dispersion for the general circuit shown in Fig. 5.13 calculated using the LC circuit model developed in this section. $L = C = 1$, $C_{\mathrm{A,B}} = 0.1C$ and $C_{cross} = 0.25C$

$$\widehat{\mathscr{C}}(k) = \begin{pmatrix} C_{\mathrm{A,B}} + 3C_{cross} & 0 & -C_{cross} & -C_{cross} & -C_{cross} \\ 0 & C_{\mathrm{A,B}} + 3C_{cross} & -C_{cross} & -C_{cross}\xi_k\eta_k^* & -C_{cross}\xi_k\eta_k \\ -C_{cross} & -C_{cross} & C_{mid} + 2C_{cross} & 0 & 0 \\ -C_{cross} & -C_{cross}\xi_k^*\eta_k & 0 & C_{mid} + 2C_{cross} & 0 \\ -C_{cross} & -C_{cross}\xi_k^*\eta_k^* & 0 & 0 & C_{mid} + 2C_{cross} \end{pmatrix}$$

The resulting dispersion is shown in Fig. 5.14. One can see that the primary effect of the site capacitance is the appearance of a pair of new modes exhibiting Dirac-like behaviour. One should expect the site capacitance to be smaller, hence values of $C_{\mathrm{A,B}} = 0.1C$ and $C_{cross} = 0.25C$ were chosen.

5.2.3 Applying *LC* Model to Experimental Data

The minimal LC circuit model reproduces both the Dirac crossing at the K-points and, qualitatively, the shape of the measured dispersion curves. However, a far better comparison between the experimental and analytical disper-

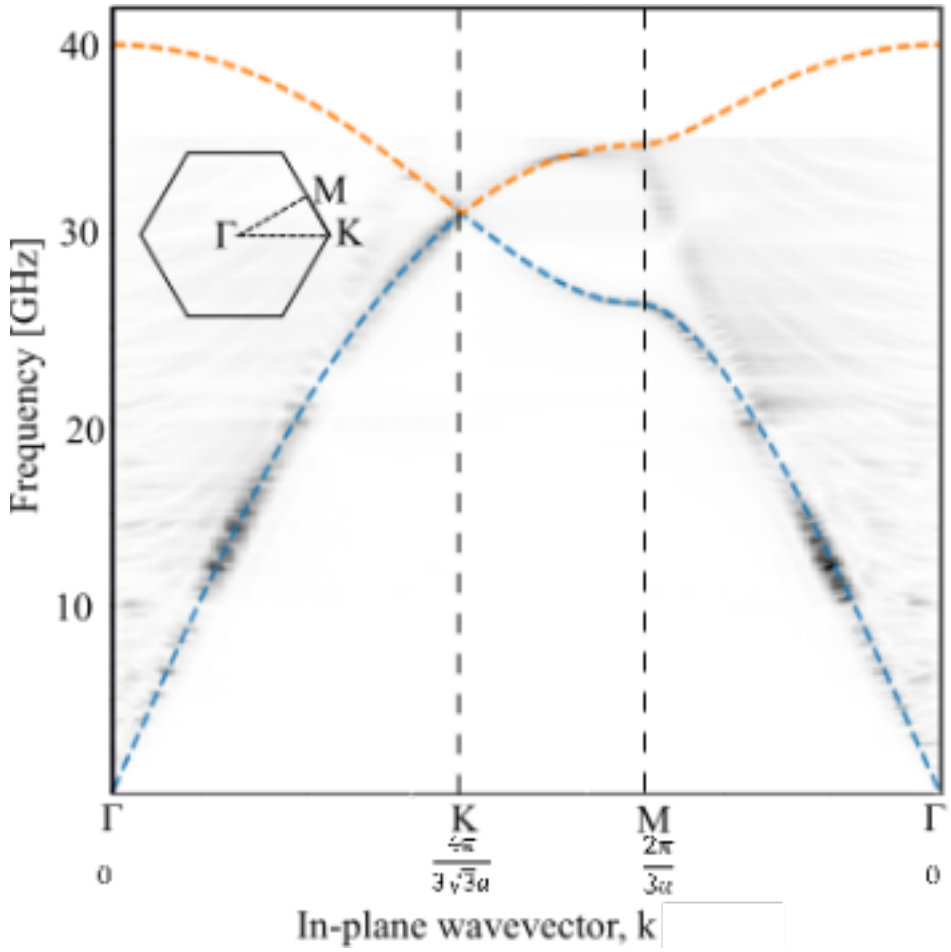

Figure 5.15: Modes dispersion obtained through Fast Fourier Transform (FFT) of the experimental data (black and white) and dispersion of the two lowest modes obtained from the LC circuit model (color dashed lines).

sion curves is achieved by taking into account the mutual capacitance of the wires, C_{cross}, and self-capacitance of the nodes A and B, C_{node}, as shown above.

There is no aim to determine the exact and accurate values of wire capacitance and inductance, but rather to assess whether the model can predict the resonance frequency and shape of the modes in general.

Calculating the capacitance of wires is not a trivial task. A few empirical studies were conducted in the middle of 20th century. As a basis of our calculations of an equivalent LC circuit we take "The calculation of electrical capacitance" by Iossel, Kochanov, and Strunskiy [135]. The equation for capacity of a rectilinear wire of a finite length is given by

$$C \approx \frac{2\pi\epsilon l}{\ln(l/a) - 0.3069 - 0.1775/\ln(l/a) - 0.5519/\ln^2(l/a)}, \tag{5.21}$$

where ϵ is permittivity (for air $\epsilon = \epsilon_0 = 1/(36\pi)\cdot 10^{-9} F/m$), l length of the wire, $2a$ is the side of wire cross section. Inductance can be calculated using the equation taken from [136]

$$L \approx 0.00508 l \left(2.303 \log \frac{2l}{w+t} + 0.5 + 0.2235 \frac{w+t}{l}\right) \mu H, \tag{5.22}$$

where l is the length in cm, w is the width in cm, and t is the thickness in mm.

Using the above equations we find values of self-inductance and self-capacitance which can match the Dirac frequency. The following values were taken to model the LC circuit: self-inductance of half the mesh wire $L = 2.8nH$, self-capacitance $C = 0.0075pF$, cross capacitance $C_{cross} = 0.25C$, and capacitance of the node $C_{node} = 0.1C$.

The eigenvalue problem of the system with the mutual capacitance taken into account is solved numerically. The resulting dispersion of the first two modes is shown in Fig. 5.15 where it is overlaid on top of the experimental data. There is a very good agreement between the modeled and measured dispersion curves.

5.3 Charge Distribution in the High Symmetry Points

In Chapter 4 it was shown that the lower and the upper modes have different field distributions in the unit cell. Namely, the upper mode is anti-symmetric along the high symmetry axis of the BZ. This explains why dispersion vanishes after the FFT is applied to the experimental data. In this section we will compare the charge distribution in the artificial hexagonal mesh graphene

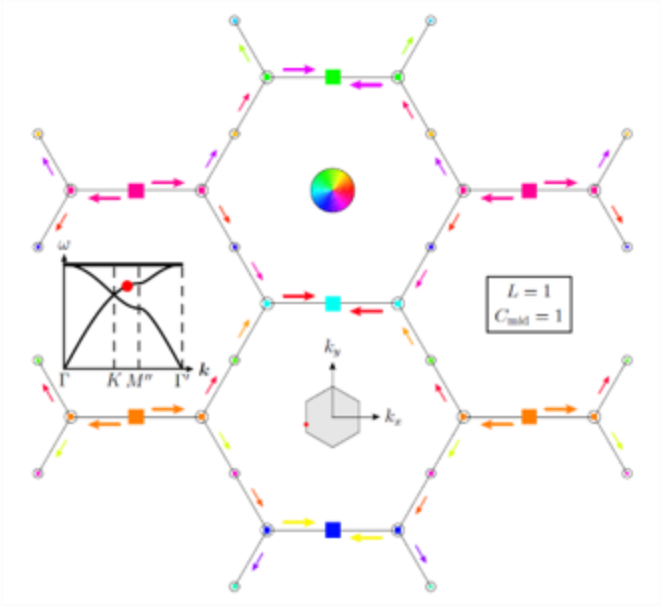

(a)

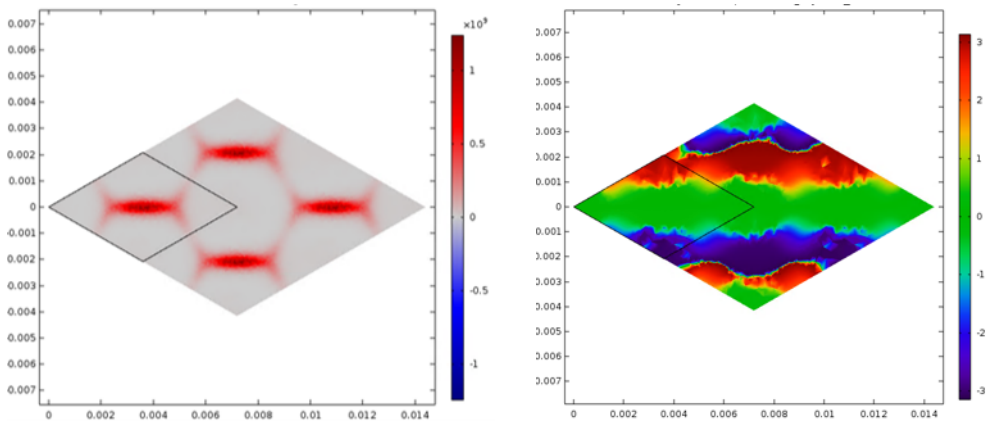

(b) (c)

Figure 5.16: Charge distribution for the mode indicated by the red point in the dispersion diagram shown in the inset. (a) From the equivalent LC model; (b) and (c) Normal component of electric field above the surface of the wire mesh and electric field phase as calculated using COMSOL Multiphysics®.

obtained from the equivalent LC model and from The COMSOL Multiphysics® modelling for modes with different momentum.

The equivalent LC circuit model is a discrete model, LC elements are located at specific points whereas the real system with wires and in COMSOL Multiphysics® model the charges which are flowing through the system are spacialy distributed.

In Fig. 5.16 and Fig. 5.17 we plot and compare fields from the LC model

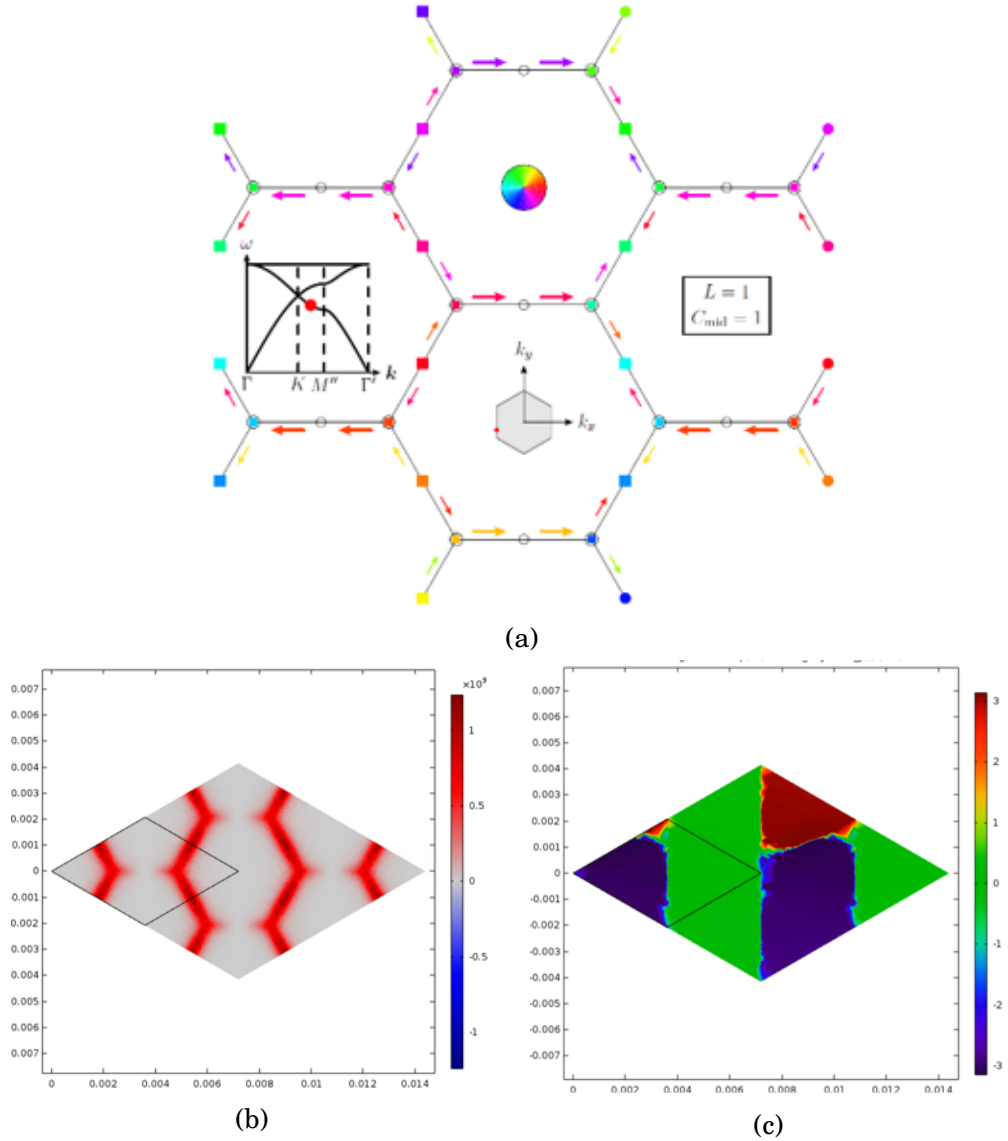

(a)

(b) (c)

Figure 5.17: Charge distribution for the mode indicated by red point in the dispersion diagram shown in the inset. (a) From the equivalent LC model; (b) and (c) Normal component of electric field above the surface of the wire mesh and electric field phase as calculated using COMSOL Multiphysics®.

(panels **a**) and from The COMSOL Multiphysics® (panels **b** and **c**). In Fig. 5.16a and Fig. 5.17a charges are represented by squares while arrows represent currents in the system. The squares and arrows size is proportional to the charge and current magnitude respectively. Their colour indicates relative phase (inset shows color map of the circular phase). In Fig. 5.16b and Fig. 5.17b the magnitude of the normal component of the electric field above the surface of the wire mesh is plotted, Fig. 5.16c, Fig. 5.17c show the electric field phase map.

Results from COMSOL Multiphysics® and from LC models show great agreement. Let us examine in more details the top mode (Fig. 5.16). One can notice that the maximum of the potential is in the middle of the horizontal wire and almost vanishes in the middle of oblique wires. The mode is symmetric in respect to the graphene sub-lattices, one can see that phase is the same on the two sides of the horizontal wire. The phase is changing in the vertical direction while staying constant horizontally. In contrast, the bottom mode has maximum of the potential at the oblique wires and zero potential at the middle of the horizontal wires. The bottom mode is anti-symmetric in respect to the two sub-lattices.

These observations let us conclude that the equivalent LC-circuit model represents well the physics in the artificial hexagonal mesh graphene and is able to predict dispersion and field distribution as well as other phenomena.

Fig. 5.18 shows potentials and currents for the upper and lower modes at various locations in the momentum space. Top panels demonstrate eigenmodes before one reaches the K point. The two bottom panels demonstrate eigenmodes past the K point. It can be seen that modes swap with each other upon crossing through the Dirac point. Whereas the bottom mode was symmetric with respect to the sub-lattices in panel (a) it becomes anti-symmetric in panel (c).

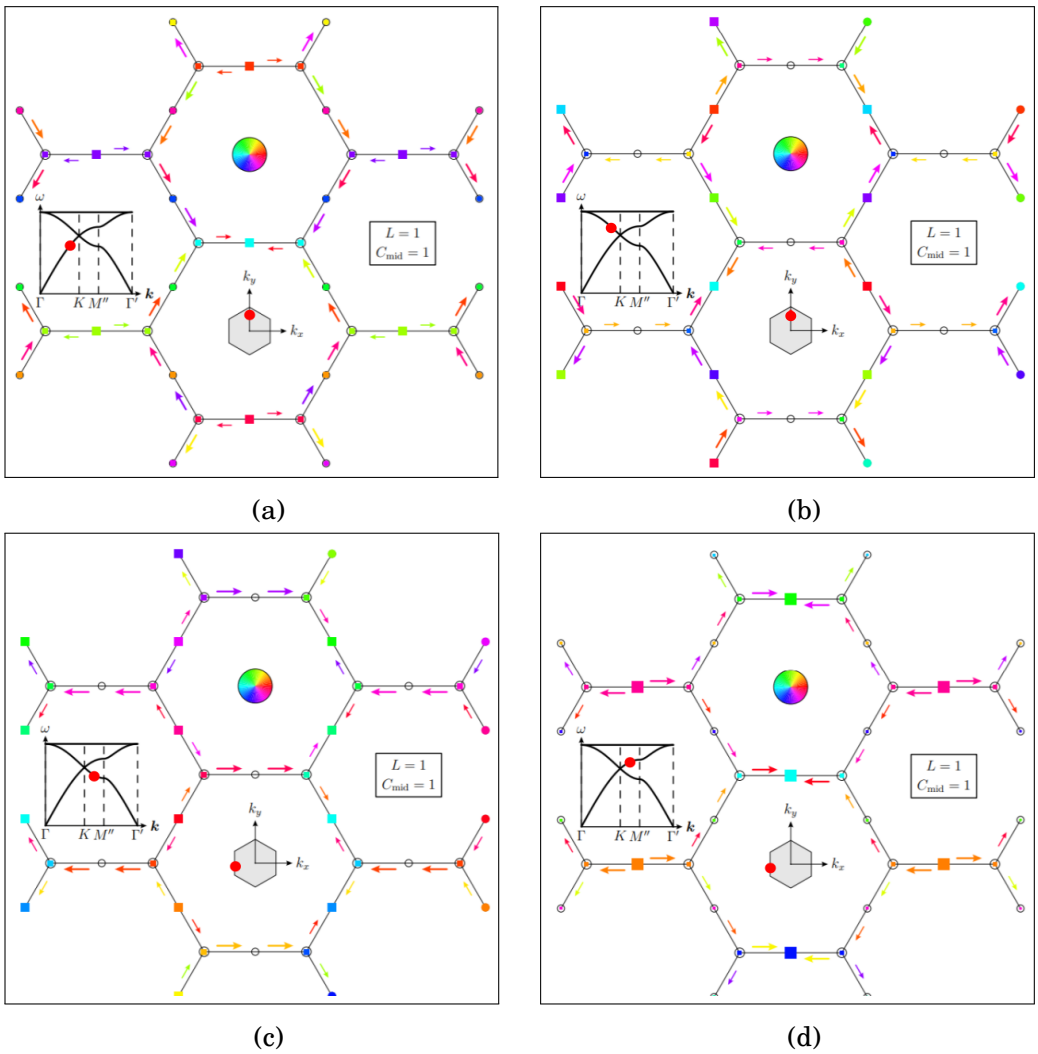

Figure 5.18: Charge distribution across the wire mesh for two points in k-space. (a) and (b) before reaching the K point; (c) and (d) upon crossing the K point. The bottom mode changes its symmetry from being symmetric before the K point to anti-symmetric after the K point. The top mode changes its symmetry from being anti-symmetric before the K point to symmetric after the K point.

5.4 Analogue of the Strain Effect

In Chapter 4 we showed how a band gap can be opened at the K point of the roded artificial graphene by breaking its inversion symmetry. In this section an approach for achieving a uniaxial strain effect in the hexagonal wire mesh artificial graphene is demonstrated. Each wire can be changed individually meaning a great level of control over the symmetry. The simplicity of fabrication means it is easy and fast to modify the structure.

In a study by Pereira et. al. [137] the authors theoretically explored the effect of strain on the electronic band structure of graphene. It was found that the gapless spectrum is robust and that a gap can only appear under anisotropy in excess of 100 % in one of the hopping directions. In the TB approximation, which accurately describes electron hopping in graphene, the Hamiltonian reads as follows ([138])

$$H = \sum_{\mathbf{R},\delta} t(\mathbf{R},\delta) a^*(\mathbf{R}) b(\mathbf{R}+\delta) + H.C. \tag{5.23}$$

Here $\mathbf{R}$ denotes a position on the Bravais lattice and δ connects side $\mathbf{R}$ to its nearest neighbors; $a(\mathbf{R})$ and $b(\mathbf{R})$ are the field operators in the sublattices A and B, $t(\mathbf{R},\boldsymbol{\delta})$ is the hopping term to the nearest neighboring atom. In graphene each atom has three neighbours and all three hopping terms are equal to each other. However, if graphene is strained, this balance can be broken depending on the direction and strength of the applied strain. It is not possible to modify hopping terms in graphene while keeping positions of the carbon atoms unchanged. Instead, elastic deformation can be applied which slightly shifts the position of the carbon atoms and thus tunes the hopping terms. However, one can argue that, in fact, elastic deformation changes the unit cell of the structure and thus also modifies its BZ.

In the case of the hexagonal wire mesh AG such hopping terms are defined by the wires that connect sites of the honeycomb lattice. We can easily change

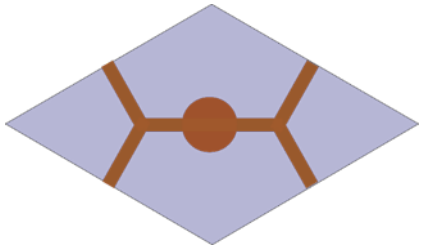

Figure 5.19: Rhombic unit cell with added circular patch to artificially imitate uni-axial strain in the horizontal direction.

each wire individually without modifying the shape of the rhombic unit cell. Let us study an increase of one of the three hopping terms by adding a circular patch onto the horizontal wire (as shown in Fig. 5.19).

The experimental dispersion relationship along the high symmetry directions for the modified system is presented in Fig. 5.20. One can notice that the Dirac crossings which were previously present at the K point of the BZ are shifted. This can be far better illustrated using iso-frequency contours (Fig. 5.21). We thus plot iso-frequency contours for the Dirac frequency $f_D = 29.75$ GHz (top) and below $f = 28$ GHz (bottom). Solid black hexagons indicate boundaries of the BZ for the reader's reference. As can be seen from these plots, Dirac crossings are shifted in k_y direction from the K points of the system BZ along the K – M direction. The size and direction of the effective deformation define new locations of the Dirac crossings. Iso-frequency contours below the Dirac frequency $f_D = 29.75$ GHz have an elliptical shape whereas for un-distorted graphene they were circular.

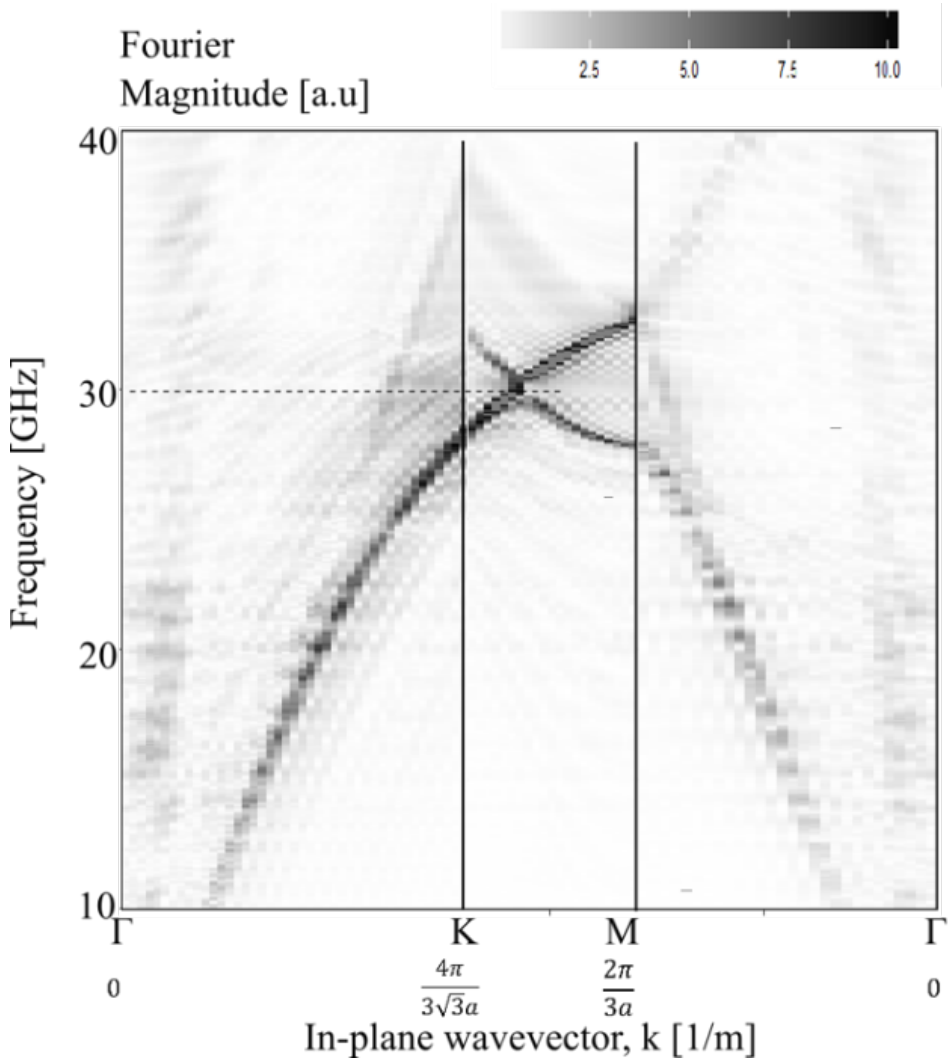

Figure 5.20: Experimental dispersion of the hexagonal wire mesh artificial graphene with artificial uniaxial strain, plotted along the high symmetry lines (Γ-K-M).

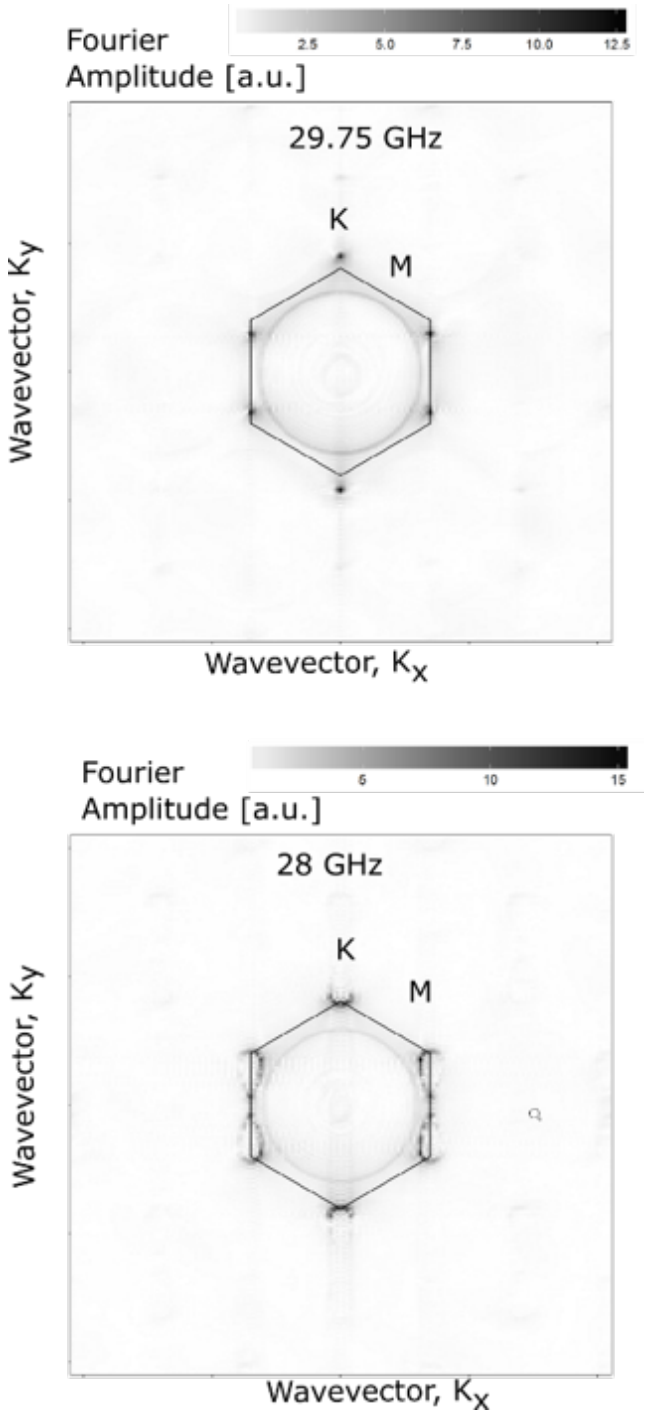

Figure 5.21: Isofrequency plots for $f = 29.75$ GHz (top) and $f = 28$ GHz (bottom). Black solid hexagon shows the BZ boundaries. We clearly see that Dirac points are moved away from K points of the BZ.

5.5 Conclusions

In conclusion, we have fabricated a simple metallic hexagonal mesh as a microwave-photonic-analogue to graphene, and experimentally measured the bound electromagnetic eigenmodes it supports. We determine the dispersion of these modes and show linear crossings at the K and K′ points of its hexagonal BZ - mimicking the well-celebrated Dirac cones in real graphene. We propose a simple, analytical LC circuit capable of representing the electrodynamics of the propagating modes. Dispersion curves calculated with this circuit model are shown to fully match the experimental data using realistic values of the inductance and capacitance of the wire mesh.

We also prove that the equivalent LC model may well represent the charge and current distribution of the hexagonal wire mesh. Comparing results with FEM show striking agreement. Results for uniaxial strain are presented at the end of this chapter. We evidence shift of Dirac points away from K points and distortion of the conical shaped dispersion.We believe that results of this work will help in a wider exploration of graphene physics.

CHAPTER 6

TOPOLOGICAL EDGE STATES IN HEXAGONAL MESH

Topological insulators have no current-carrying states in the bulk, due to a gap in the spectrum, nevertheless they conduct electricity via the edge modes [139, 140]. These modes are topologically protected in systems with broken time reversal symmetry, such as quantum Hall bars. The protection makes such edge modes immune to scattering by impurities of a non-magnetic nature. Inspired by advances in condensed matter physics, one may engineer photonic systems that host topologically protected states. This may open the route to designing scattering-free waveguides with unidirectional flow of electromagnetic energy [112, 113, 141, 142].

Early attempts to implement topologically protected edge modes in photonics relied on the use of magnetic fields [111, 143, 144], by analogy to the quantum Hall edges with chirality defined by the external magnetic field [145]. However, strong magnetic fields may be hard to achieve, hence one may also explore the topological photonic modes that are invariant under time reversal,

akin to electron states in topological insulators with spin-orbit coupling exhibiting quantum spin-Hall effect [112, 113, 146]. To emulate this physics with photons, one may consider a bipartite photonic crystal, so that the sublattice index would play the role of a pseudospin. The edge of a gapped crystal would then host a pair of degenerate helical photonic modes with opposite pseudospins propagating in two opposite directions. Wu et. al. [147] demonstrated that a two-dimensional (2D) photonic crystal with C_6 symmetry does indeed support a topological phase transition associated with contracting or expanding elements in the hexagonal unit cell. Thereby, an interface between such crystals may host helical edge modes. Such an approach is completely scalable, and it has therefore been applied to a range of photonic systems to design unidirectional wave propagation. These include, for example, topological systems based on dielectric [148–150] and metallic elements [151], at infrared [150, 152] and microwave [148] frequencies. The idea can also be applied to acoustic waves [153, 154]. The edge states in the papers cited above are detected by means of transmission experiments. The fields are scanned to visualize the edge mode. However, there was no direct measurement of edge state dispersion, to demonstrate how edge modes connect to bulk modes. In the current work we will show experimental dispersion relationships for both bulk and edge modes.

We study microwave helical edge modes hosted by an interface between two plane conducting meshes with C_6 symmetry but different unit cell types, one in which alternate hexagons are shrunk and one in which alternate hexagons are expanded. Indeed, the interface exhibits two edge states. Our measurements also reveals that the behaviour of the edge modes is sensitive to the orientation of the edge. Using near-field measurements of the normal component of the electric field we prove that edge modes propagating along the Γ-to-K interface are weakly hybridized with each other and thus exhibit a small band gap. However, if the interface is formed along the Γ-to-M direction, the edge modes

remain topologically protected and continue across the band gap of the bulk states. Our findings are supported by equivalent LC model and explained by the effective Hamiltonian.

6.1 Equivalent *LC* circuit

6.1.1 Dispersion of Surface Modes

The previously studied artificial microwave graphene Chapter 5 system was chosen as a basis for the transformations proposed in [147]. The plane copper hexagonal wire mesh, which well mimics graphene physics for the supported electromagnetic waves, can be described in terms of massless Dirac fermions with two conic points at K and K′ of the BZ.

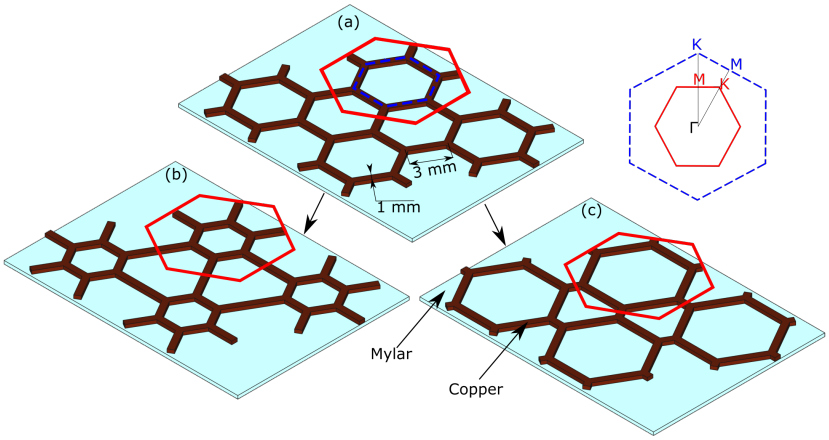

Figure 6.1: Schematic representation of the systems studied. (a) Undistorted original copper hexagonal mesh on a thin layer of dielectric. Blue dashed hexagon indicates the original unit cell, red solid lines indicate the bigger hexagonal unit cell introduced for distortion purposes. (b) Contracted Structures (CS) - the sides of the hexagon inside the unit cell are shortened. (c) Expanded Structures (ES) - the sides of the hexagon inside the unit cell are increased. Insert shows the BZ for the original structure (dashed blue hexagon) and for the distorted systems (solid red hexagon).

To obtain two topologically different phases of the base system, we choose a new, larger, unit cell containing a single hexagon structure, and then contract and expand it, as shown in Fig. 6.1. In terms of Dirac fermions, the deformation results in finite fermion mass, with opposite sign at the two conic points. The mass is propotional to the deformation, hence its sign is opposite for contracted and expanded phases.

The structure explored in the current work is a simply-connected hexagonal mesh formed by metallic wires that support electric currents, and thus its equivalent LC circuit can be readily introduced using circuit theory. As shown in Chapter 5 each wire of the hexagonal mesh can be replaced by equivalent L and C elements, representing self-inductance and self-capacitance of the wires (we assume the wires to be perfect conductors, which is a reasonable approximation at microwave frequencies). The cross-capacitance and cross-inductance can be ignored as the physics remains the same, as explained in Chapter 5. The minimal LC circuit capable of qualitatively representing the electrodynamics of the system is shown in Fig. 6.2. The basic hexagonal unit is bordered by the black dashed line and consists of fifteen nodes. The nodes A and A', B and B', C and C' are connected with each other by the translation vectors. To mimic the Contracted Structures (CS) and Expanded Structures (ES), capacitors and inductors that are indicated in blue need to be changed with respect to the capacitors and inductors shown in black.

The generalized eigenvalue problem of the introduced LC circuit model is defined by $\omega^2(\mathbf{k})\widehat{\mathscr{C}}(\mathbf{k})\Phi(\mathbf{k}) = \widehat{\mathscr{L}}(\mathbf{k})\Phi(\mathbf{k})$, where $\widehat{\mathscr{C}}(\mathbf{k})$ and $\widehat{\mathscr{L}}(\mathbf{k})$ are generalized capacitance and inductance matrices, and $\mathbf{k}$ is the Bloch wave vector for a given mode. The flux variable $\Phi(\mathbf{k})$ is defined at the nodes via $J_X(\mathbf{k}) = C\dot{V}_X(\mathbf{k}) = -C\ddot{\Phi}(\mathbf{k})$ with $J_X(\mathbf{k})$ and $V_X(\mathbf{k})$ being current and voltage at the circuit node X, respectively (see Chapter 5). The mode dispersion $\omega(\mathbf{k})$ is easily found by solving the characteristic equation $\det[\widehat{\mathscr{C}}(\mathbf{k})\omega^2 - \widehat{\mathscr{L}}(\mathbf{k})] = 0$. The generalized

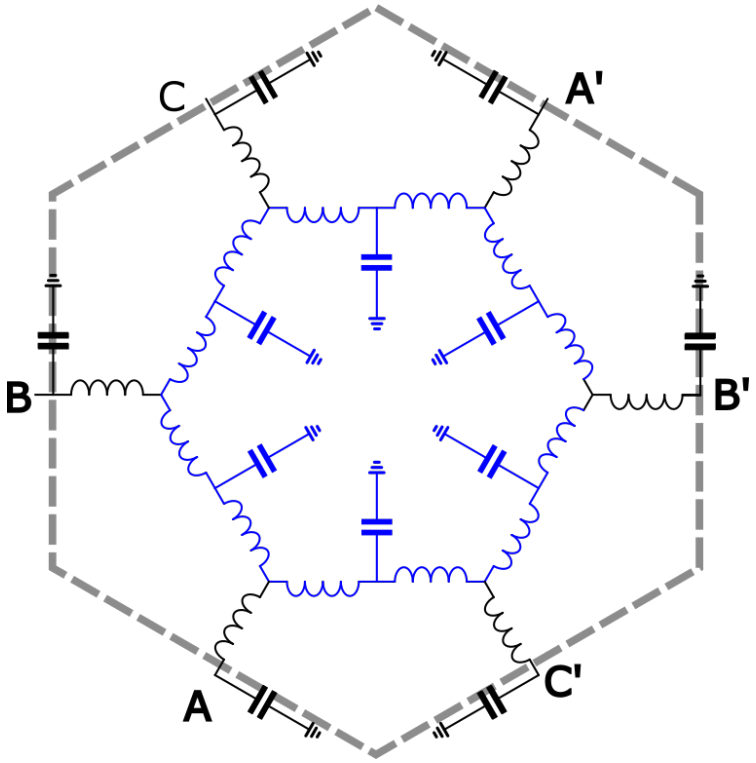

Figure 6.2: The circuit model employed for reproducing and analyzing the electrodynamics in a wired honeycomb mesh. Dashed grey line indicates the base cell where points A and A′, B and B′, C and C′ are equivalent and connected by Bloch translation vectors. Inductors and capacitance represent self-inductance and self-capacitance of the copper wires.

capacitance and inductance matrices can be found either by solving Kirchhoff's laws or from analyzing their contributions to the energy which is expressed through matrices $\widehat{\mathscr{C}}$ and $\widehat{\mathscr{L}}$ as $W_E = V^* \widehat{\mathscr{C}}(\mathbf{k}) V/2$, $W_M = \Phi^* \widehat{\mathscr{L}}(\mathbf{k}) \Phi/2$, as was derived in Chapter 5.

To model the behaviour of the undistorted system we constructed two matrices [15x15] for inductances and capacitors in the system and applied Bloch boundary conditions to the edges of the unit cell. We set all capacitances C and inductances L equal to 1 (blue and black in Fig. 6.2). We then solve the eigenvalue problem for these matrices to obtain the dispersion and the charge distribution of the circuit.

For the CS system, the wires on the inner hexagon are shortened by 10 %, and thus the corresponding capacitance (blue) and inductance (blue) values

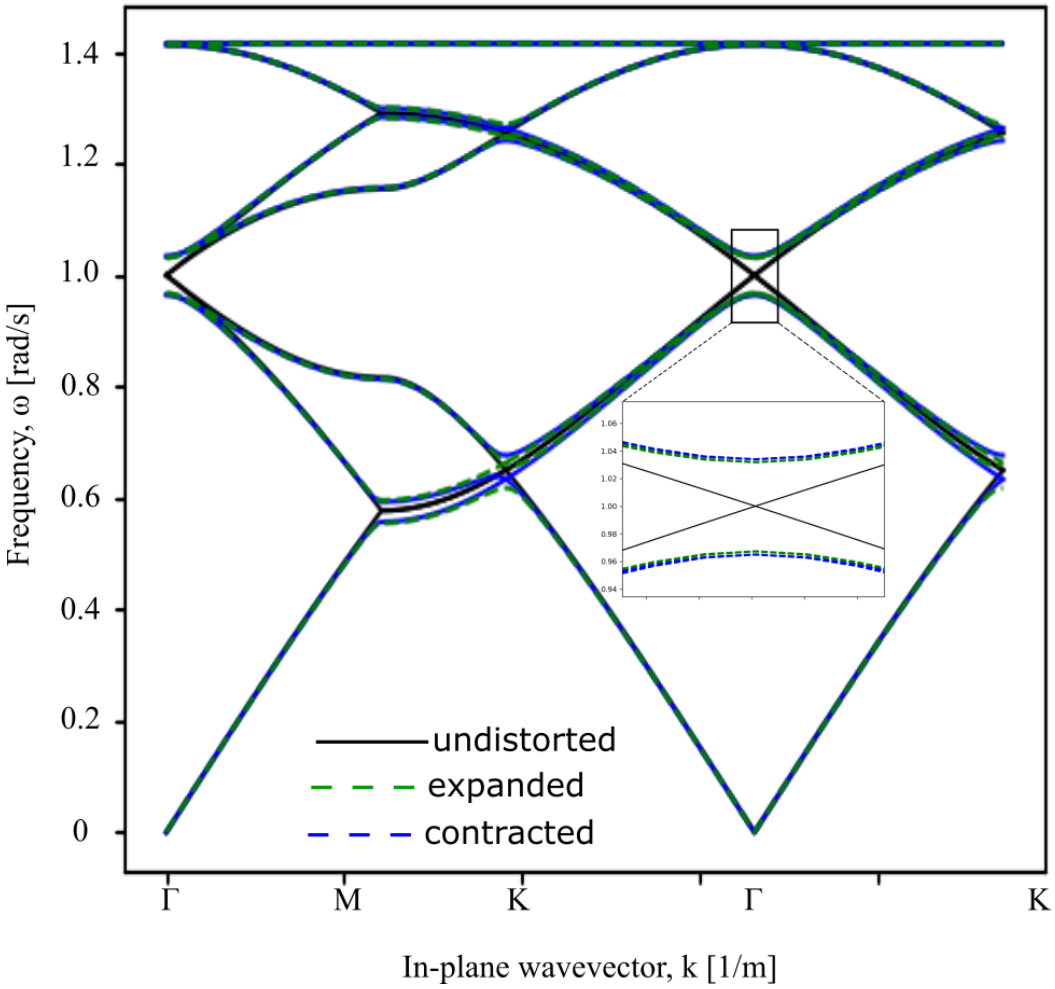

Figure 6.3: Band structure of modes supported by the undistorted (black lines) equivalent LC circuit (L=C=1), where the unit cell is chosen to be three times bigger leading to band folding. Dispersion of expanded (dashed green) and contracted (dashed blue) lattices are overlaid. Inset shows zoom of the modes around the Γ point.

need to be decreased by 10 %. For the ES system the inner hexagon wires are extended and thus we increase values of the corresponding capacitance and inductance by 10 %. Modelled dispersion curves of undistorted, contracted, and expanded structures are plotted in Fig. 6.3. The enlarged unit cell for the undistorted case leads to modes back-folding and, as a result, the four Dirac cones at K and K′ points relocate to the Γ point of the new BZ (plotted in black line). For the distorted cases, a band gap opens at the Γ point proportional to the applied distortion. Modes for expanded and contracted structures are

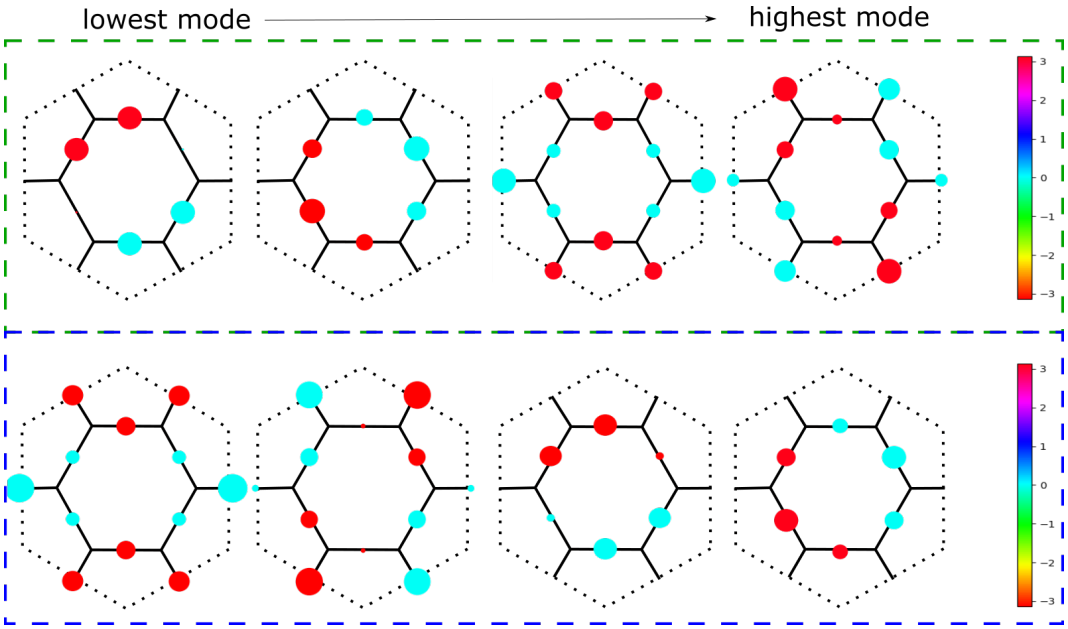

Figure 6.4: Charge distribution of modes supported by the expanded (in dashed green box) and contracted (in dashed blue box) structures at the Γ point. Color of the circles represents phase and the size of the circles represents value of the charge

plotted as green and blue dashed lines. Inset shows a zoom of the region near the Γ point.

In Fig. 6.4 we plot the charge distribution of modes at the Γ point for ES and CS. Modes for the expanded case are plotted in the dashed green box and for the contracted case in the dashed blue box. Size of the circles is proportional to the value of the charges. The color of the circles sweeps from red-cyan-blue-green-yellow-red and represents the phase sweep from $-\pi$ to π. We can see that for the expanded case the two lower energy modes are dipole-like while the two upper energy modes are quadrupole-like. However, for the contracted case there is band inversion, and the dipole-like modes are higher in frequency and energy than the quadrupole-like modes, which is a mark of topological non-trivial systems [155]. It should be noted that contrary to the previous studies band inversion appears when the structure was contracted, while in original work the authors showed that band inversion is a feature of expanded deformation [147]. This can be understood from the nature of the generalized

inductance matrix $\widehat{\mathscr{L}}$. It is analogues to the spring constant of a classical mechanical resonator but with all of its elements being inversely proportional to the self-inductance of the circuit wires L_{X}. Therefore, with decreasing value of L_{X}, the coupling strength of the neighbouring elements is increased. This behaviour contrasts with the coupled dielectric resonators considered in other studies.

Previously massless fermions at the Γ point now have mass - the previously linear dispersion has now a higher order contribution, see inset in Fig. 6.3. Depending on the sign of deformation (contracted or expanded) the mass has a different sign too. Jackiw and Rebbi showed that there is a solution of the bound state at the interface between the regions of positive and negative masses [156]. The solution is dominantly distributed near the interface and decays exponentially away from the interface.

6.1.2 Interface Configuration and Edge Modes

To form the interface between the structures, CS and ES grids can be readily connected along either of the two orthogonal directions: the Γ-to-K direction or the Γ-to-M direction. Let's call the interface formed in Γ-to-K direction the "zig-zag" interface, as it forms zig-zag profile, when the two structures are connected, see Fig. 6.5a. Similarly, direction Γ-to-M we will call the "arm-chair" interface, see Fig. 6.5b.

To model the edge states, we connect two 15 unit cell-long ribbons of CS and ES structures to each other. Bloch boundary conditions are then applied to make the structure infinite in the direction of the interface. Fig. 6.6 shows dispersion of the bulk modes (plotted in grey) and edge modes (plotted in orange and blue) for the case when the interface is parallel to the Γ-to-K direction (zig-zag). The small band gap $\hat{\Delta}$ formed between the edge modes can be seen clearly. This mini gap is a second order gap of that between bulk modes, Δ_0,

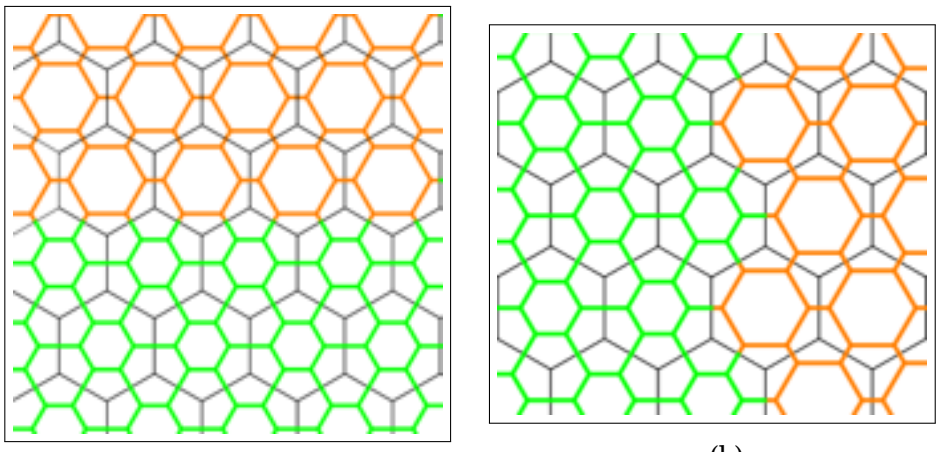

(a) (b)

Figure 6.5: Two ways of forming a simple interface between contracted and expanded structures. Orange lines - expanded mesh, green lines - contracted mesh, black lines - indication of the hexagonal cell boundaries for visualisation purposes. (a) Structure is formed along the Γ to K direction (zig-zag). (b) Structure is formed by connecting flat sides of the hexagonal cells together, which forms an interface along the Γ to M direction (arm-chair).

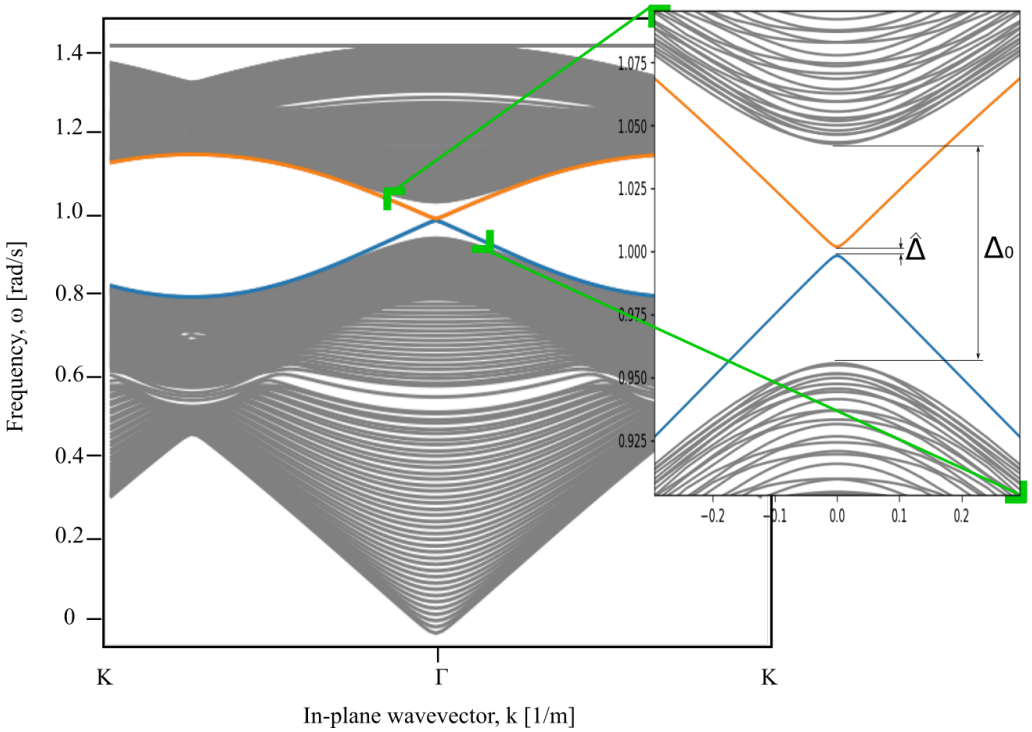

Figure 6.6: Mode dispersion modelled with LC-equivalent circuit for the zigzag interface. Bulk modes are plotted in grey, edge modes are plotted in orange and blue. Inserts show a zoom of the edge mode dispersion at the Γ point. There is a gap between the edge modes.

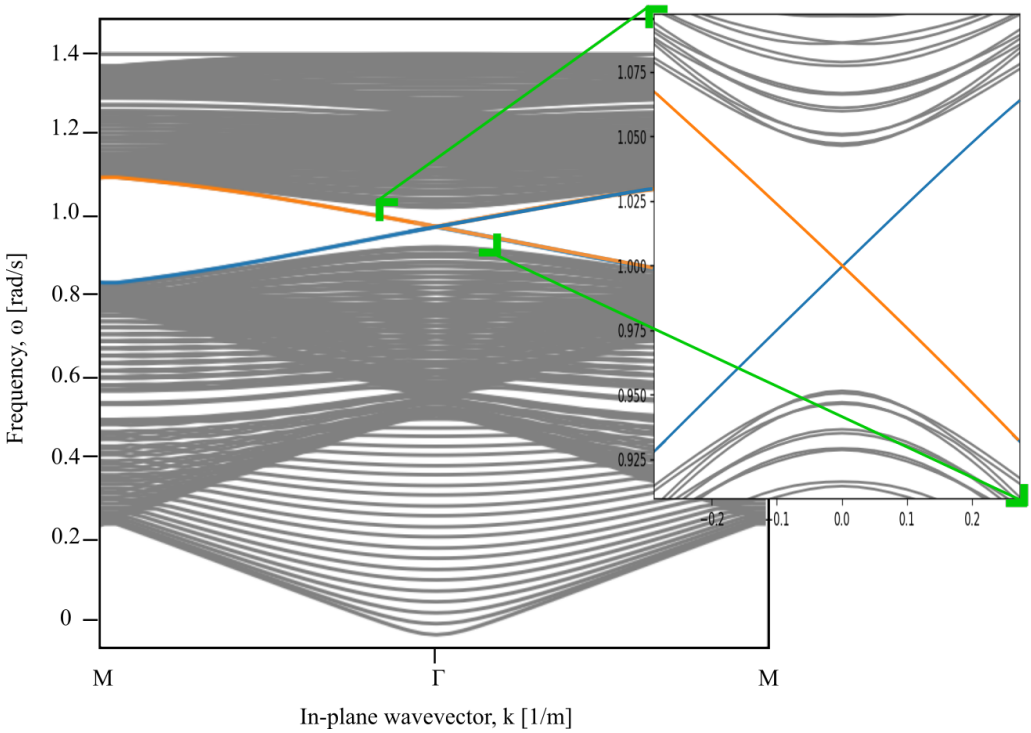

Figure 6.7: Mode dispersion modelled with *LC*-equivalent circuit for the armchair interface. Bulk modes are plotted in grey, edge modes are plotted in orange and blue. Inserts show a zoom of the edge mode dispersion at the Γ point. There is no gap between the edge modes.

which itself is a first order value of the deformation applied.

If the interface is parallel to the Γ-M direction the gap $\hat{\Delta}$ does not open regardless of the applied distortion (Fig. 6.7). We plot and compare the charge distributions for gapped and gapless interfaces in Fig. 6.8 and Fig. 6.9 respectively. First we plot total charge magnitude in each unit cell across the interface between the two structures for the modes in the gap (blue and orange) and closest bulk modes (grey) in the vicinity of the Γ point. A plot for the zigzag interface is presented in Fig. 6.8a and a plot for the armchair interface is presented in Fig. 6.9a. We confirm that modes are concentrated at the interface decaying exponentially away from the interface and no edge effects, which could cause a mini gap, are interfering with the modes. Bulk modes (plotted in grey) have maximum at the middle of each half of the structure, gradually

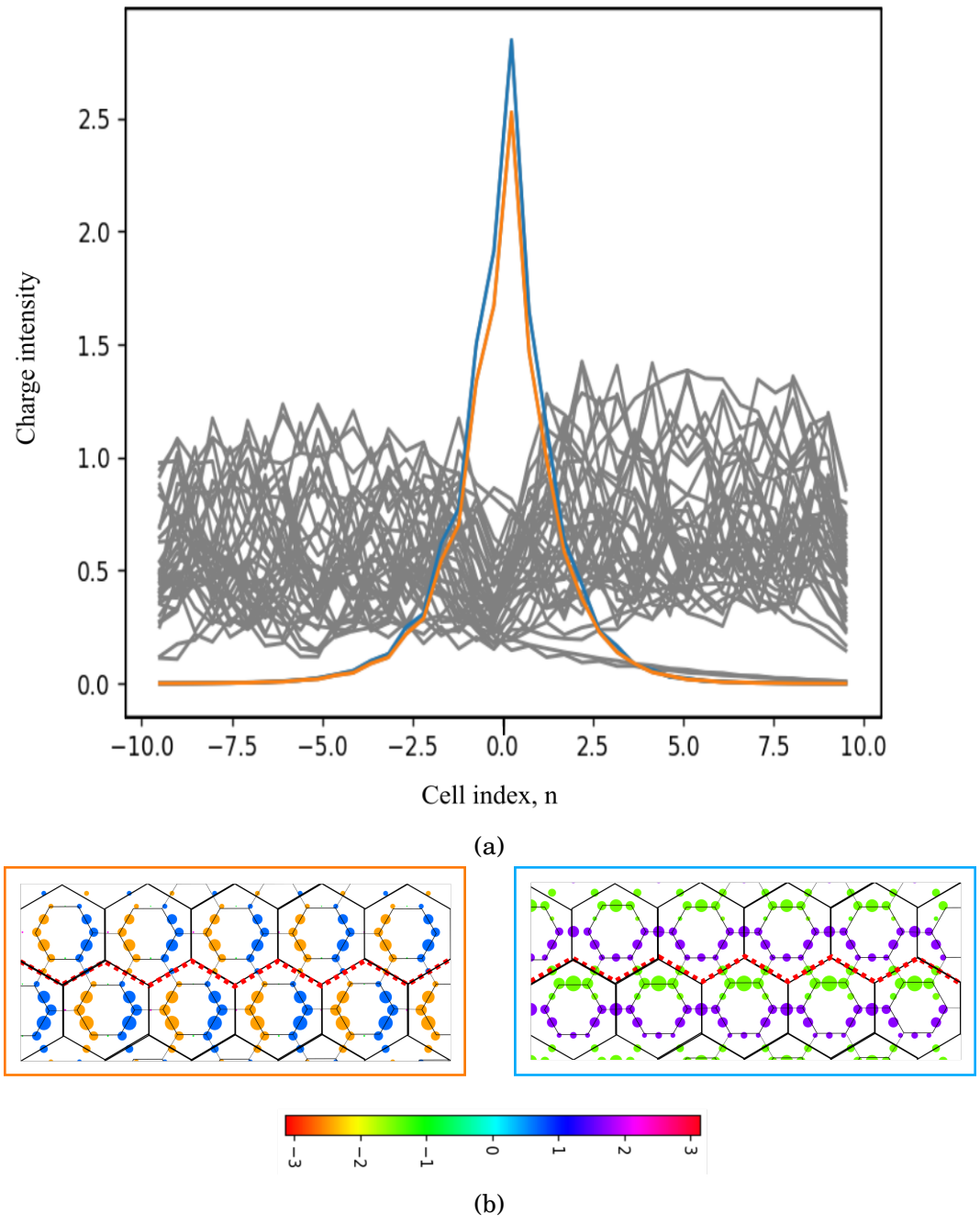

Figure 6.8: Charge distribution for the modes in the vicinity of Γ for the zig-zag interface. (a) Charge distribution is plotted across the interface for edge modes (in orange and blue) and some bulk modes (in grey). X-axis shows the unit cell number with the interface located at 0. (b) Charge distribution is plotted inside the unit cell along the interface for two edge modes (in orange and blue boxes). Dotted red line show the interface between contracted and expanded structures. Size of the circles is proportional to the charge magnitude and color indicate relative phase. Zigzag interface configuration gives symmetric and antisymmetric modes with phase changing by π across the unit cell.

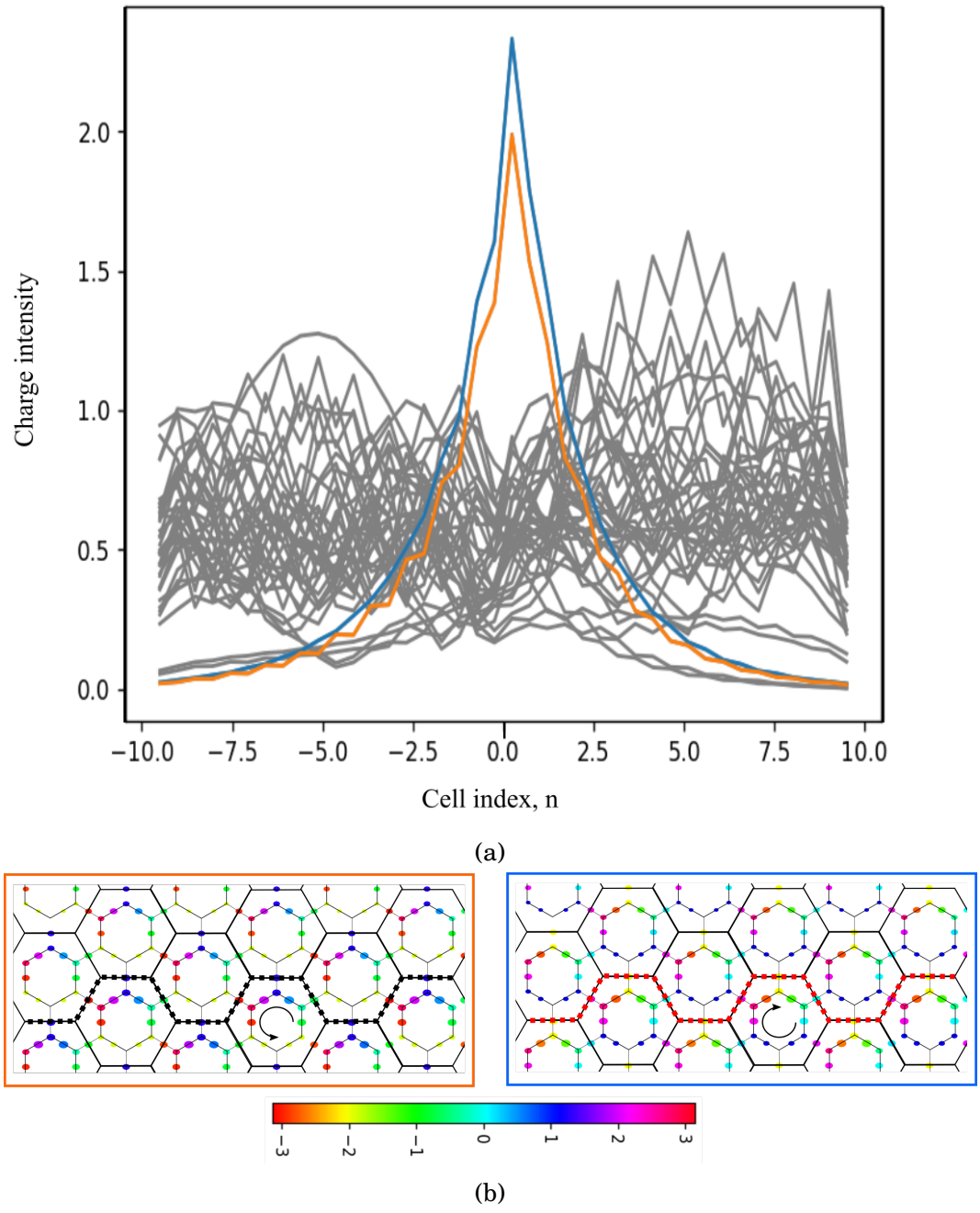

Figure 6.9: Charge distribution for the modes in the vicinity of Γ for the armchair interface. (a) Charge distribution is plotted across the interface for edge modes (in orange and blue) and some bulk modes (in grey). X-axis shows the unit cell number with the interface located at 0. (b) Charge distribution is plotted inside the unit cell along the interface for two edge modes (in orange and blue boxes). Dotted red line show the interface between contracted and expanded structures. Size of the circles is proportional to the charge magnitude and color indicate relative phase. Armchair configuration gives modes with chirality in phases which progressively change around the circle.

decaying to the edges. Let us examine the field profile inside the unit cells for edge modes and cross compare them for the two interface configurations. Our results reveal that the formation of the band gap $\hat{\Delta}$ along one direction and its absence along the other direction are also manifest in the charge distribution of the corresponding edge modes. In Fig. 6.8b we plot fields for the zigzag case where the modes form a mini gap and see that fields of one mode are symmetric within a unit cell with respect to the interface line, and anti-symmetric for the second mode. However Fig. 6.9b shows that for gapless modes the fields are 'handed' where one mode changes phase in the clockwise direction and the second mode in the anti-clockwise direction.

6.1.2.1 Hamiltonian

To understand further the nature of the two edge modes present at the interface between CS and ES systems and why one edge configuration results in a mini-gap, while the other yields a gapless spectrum we analyze the Hamiltonians of both the undistorted and deformed systems.

Let us introduce a coordinate system in which the x-axis is aligned along the Γ-to-K direction and the y-axis is aligned along the Γ-to-M direction. The honeycomb structure possesses pairwise equivalent K and K′ points. In the vicinity of each K and K′ point, Bragg scattering mixes waves corresponding to the two non-equivalent sub-lattices of the honeycomb structure. This results in linear Dirac crossings located at the corners of the BZ and trigonal warping when moving slightly away from the K and K′ points. The effective Hamiltonian of the undistorted system can be expressed as

$$H_0 = v_{\mathrm{F}}\left(\hat{\sigma}_x\hat{p}_x + \hat{\sigma}_y\hat{p}_y\right) + 2\lambda\hat{\tau}_z\left(2\hat{\sigma}_x\hat{p}_x\hat{p}_y + \hat{\sigma}_y\left(\hat{p}_x^2 - \hat{p}_y^2\right)\right), \tag{6.1}$$

where v_{F} is the Fermi velocity, $\hat{\sigma}_x$, $\hat{\sigma}_y$ are the Pauli matrices, $\hat{p}_x$, $\hat{p}_y$ are the momentum operators, λ is a generic complex-valued trigonal warping

amplitude and $\hat{\tau}_z$ is the isospin operator defined so that $\hat{\tau}_z = 1$ near the K point while $\hat{\tau}_z = -1$ near the K′ point. This Hamiltonian is invariant under time reversal. Now let us consider the deformation. As discussed previously, we have chosen the new unit cell shown in Fig. 6.1 and the K and K′ points of the old BZ back-fold into the Γ point of the new BZ. This results into coupling of K and K′ modes. The Hamiltonian of the deformed system reads as

$$\hat{H}_1 = H_0 + \Delta_x \hat{\tau}_x \hat{\sigma}_z + \Delta_y \hat{\tau}_y \hat{\sigma}_z, \tag{6.2}$$

where Δ_x, Δ_y are the terms characterizing the mode mixing strength and $\hat{\tau}_x$, $\hat{\tau}_y$ are the coupling operators. Spin operator $\hat{\sigma}_z$ is required to preserve time-reversal symmetry. Earlier we noted that four Dirac cones at the Γ point of the new BZ originate from the K and K′ modes of the original honeycomb lattice. If the interface is along the y-direction, then the trigonal term $\hat{V} = -2\lambda \hat{\tau}_z \hat{\sigma}_y p_x^2$ does not mix the two edge modes. However if the interface is formed along the x-direction the trigonal term $\hat{V} = 2\lambda \hat{\tau}_z \hat{\sigma}_y p_y^2$ results in mode mixing and a gap between modes. Trigonal warping in the vicinity of the K and K′ points manifests itself in equienergy contours of triangular shape. The triangular equienergy contour around the K point is rotated by 30 degrees with respect to the similar equienergy contour around the K′ point. When folded back to the Γ point, these triangles overlap and share symmetry in the Γ to K direction. Thus the edge modes will mix with each other resulting in the band gap opening. The general equation for the gap which depends on the interface direction can be given as [157]:

$$\Delta = \frac{2\lambda \Delta_0^2}{v^2} |\cos 3\alpha|, \tag{6.3}$$

where Δ_0 is the gap in the bulk, α is the angle between the interface and the x-axis, giving a maximum when the interface is along the x-axis.

6.2 Experimental Verification

6.2.1 Bulk Surface Modes

To perform experimental measurements we fabricate a plane hexagonal wire mesh made of 19 μm thick copper on top of 50 μm dielectric substrate using the procedure described in Chapter 3. The wires forming the hexagonal mesh are each 3 mm long and 1 mm wide for an undistorted sample. For CS and ES cases wires for the inner hexagons were 2.7 mm and 3.3 mm long respectively. The rest of the wires were adjusted as needed. The total size of the mesh was 40x30 cm.

To excite and detect bound electromagnetic modes supported by the samples, a pair of stripped-end coaxial cables, used as near-field antennas, were placed with their coaxial axes normal to the sample surface and with the metal tips approximately 0.5 mm away from the surface. The exciting antenna was placed above the wire in the centre of the sample while the detecting antenna was raster-scanning across the surface on the opposite side of the sample. Both antennas were connected to ports of a microwave VNA measuring S_{21} values as a function of the position and over a frequency range from 10 to 40 GHz. The spatial Fast Fourier Transform (FFT) is then applied to the field profile to obtain a 2D dispersion map of the supported modes in momentum space (k_x, k_y). Combining these maps measured at different frequencies produces the full 3D dispersion data array.

The band structure of the original undistorted system exhibits Dirac crossings at K and K$'$ points at 30 GHz Chapter 5. For the distorted cases, the modes from K and K$'$ are back-folded to the Γ point when one passes to the smaller BZ for the superlattice. On the dispersion diagram for the CS case in Fig. 6.10 one can see that linear Dirac crossings are now gapped with a band gap of $\approx$ 2 GHz at Γ at a frequency around 30 GHz. We plot dispersion in the extended BZ

scheme to avoid obscuration of the bound modes by the radiative modes inside the light cone. In Fig. 6.10b we plot dispersion through equivalent Γ points in the next Billion zones to see clear dispersion at the Γ point . In Fig. 6.10c we plot instantaneous electric field for the frequency of 30 GHz and confirm that there are no modes propagating across the sample, neither bulk nor edge modes. Similar results can be shown for ES case.

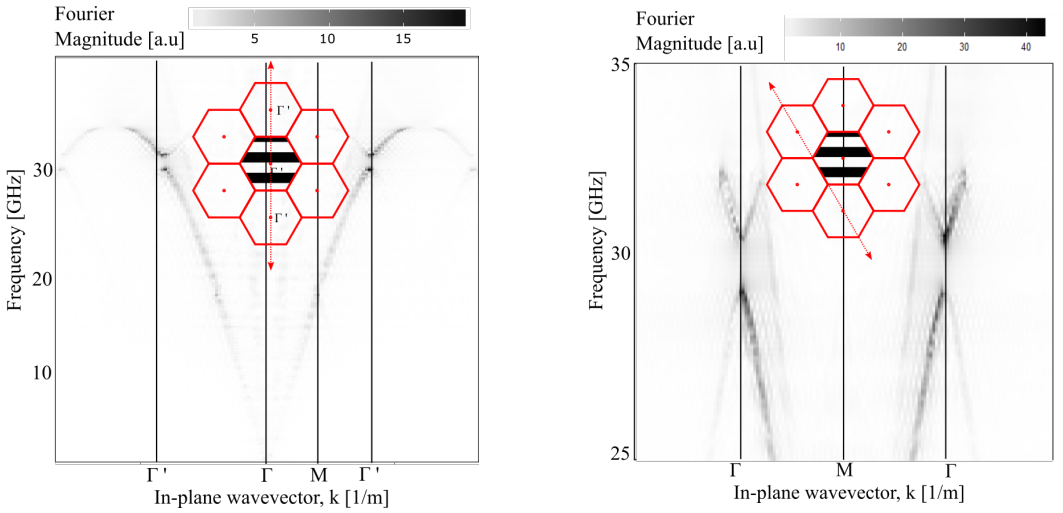

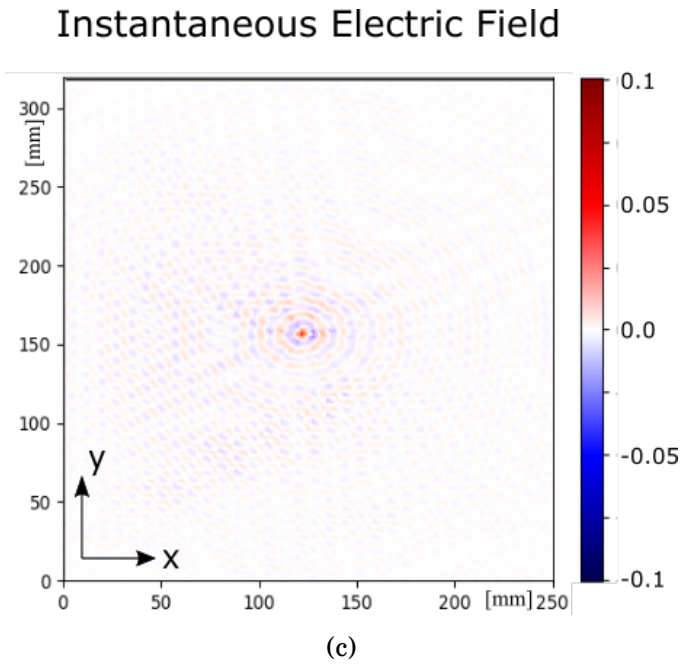

Figure 6.10: (a) and (b) Experimental dispersion of the microwave surface (bulk) modes supported by the distorted structure (CS). System possesses a complete band gap in the vicinity of the Γ point for frequencies between 29 and 31 GHz. The inset shows extended BZ structure and the direction of plotting is indicated with the red arrow. (c) Instantaneous Electric Field at $f = 30\,\mathrm{GHz}$ to show that indeed there are no propagating modes at the frequency.

6.2.2 Edge Modes

Having studied the bulk modes for the distorted case we then connect ES and CS hexagonal meshes along the Γ-to-K direction (see Fig. 6.5a) to study the edge modes and the gap.

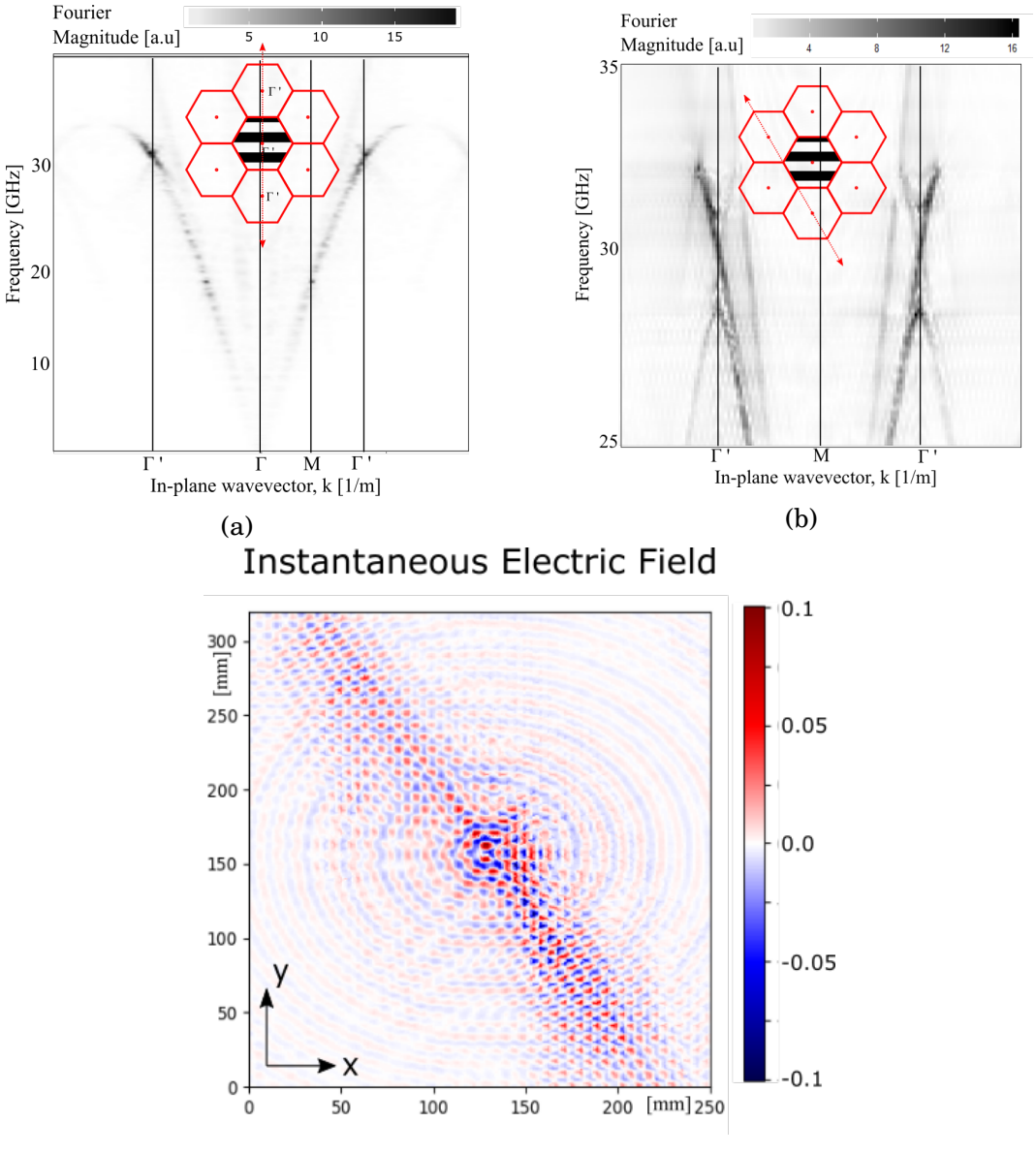

Figure 6.11: (a) Experimental dispersion of microwave surface modes supported by the structure of two connected distorted structures. Edge modes now occupy the frequency range where previously there was a band gap in the vicinity of the Γ point. (b) Shows the zoomed dispersion around the Γ point. (c) Instantaneous Electric Field at $f = 30$ GHz. A highly localised interface mode is visible.

We place the transmitting antenna in the centre of the interface between the two meshes. Rastering the detection antenna across the entire sample, and performing FFT of the measured electromagnetic fields, we simultaneously obtain both bulk and edge mode dispersion curves.

The edge mode dispersion is plotted by slicing the 3D band structure data array right through the Γ point in the direction parallel to the interface, see Fig. 6.11b. Edge modes are clearly seen for the range of the frequencies from 29 GHz to 31 GHz around the Γ point.

The finite k-space resolution (which is dictated by the sample size) and width of the edge modes (which is approximately 900 MHz, see Fig. 6.11b) limits our ability to observe the mini gap due to edge modes hybridization.

However we can examine the distribution of the near fields and analyze whether modes have been hybridized. If the fields of the two edge modes are symmetric and anti-symmetric as described above, the modes have hybridized; if the modes are circularly polarised this means they remained fully protected.

We compare the field distribution of the edge modes launched along the interface Γ-to-K (zig-zag) and Γ-to-M (armchair). In Fig. 6.12a and Fig. 6.12c we plot instantaneous electric fields for zig-zag and armchair cases correspondingly. It is immediately apparent that the field profile of the launched edge modes are very different. We can see that in the zig-zag direction the mode is anti-symmetric (Fig. 6.12a), as opposed to in the armchair direction (Fig. 6.12c) where the field profile is much more sophisticated. We explore phase maps and see that for the zig-zag interface profile, as expected, the phase across the interface has a π jump corresponding to the anti-symmetric profile (see Fig. 6.12b), however the phase for the gapless case (see Fig. 6.12d) changes gradually and continuously in an anti-clockwise, thus rotatory fashion. This result demonstrates the existence and character of the topologically protected state.

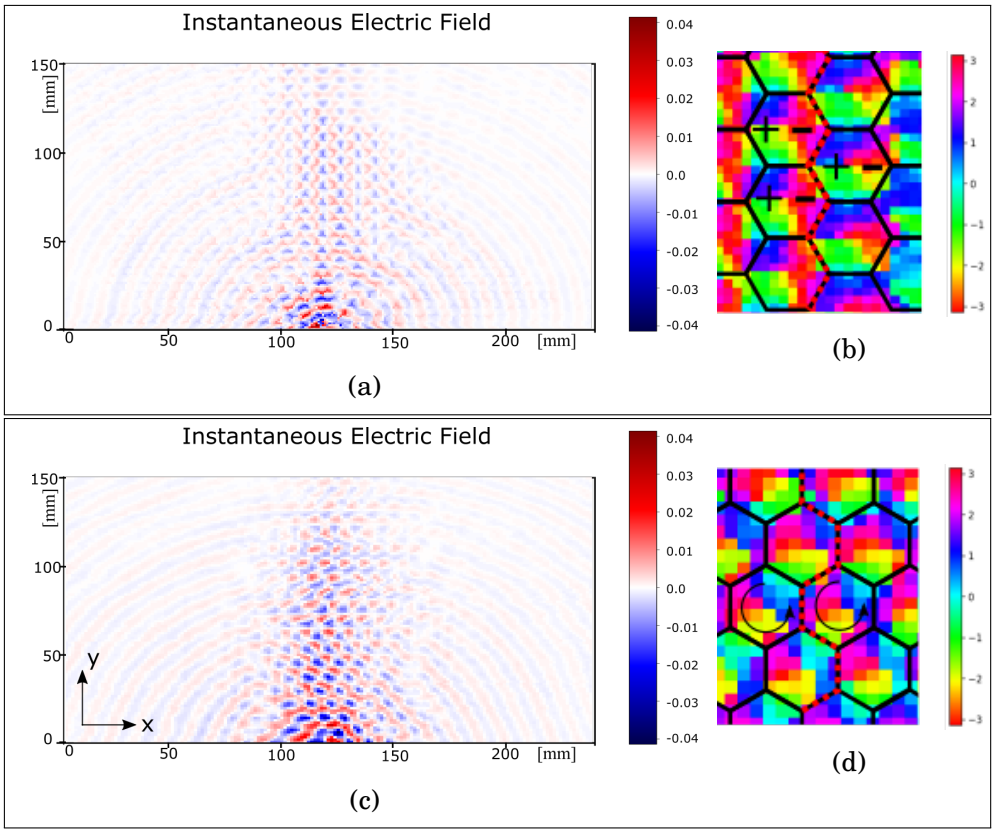

Figure 6.12: (a) Instantaneous electric field at f = 30GHz for the zig-zag configuration of the edge. (b) Instantaneous Electric Field at f = 30GHz for the arm-chair configuration of the edge. (c) Phase of the normal component of the electric field of one of the edge modes for the zigzag connection. The phase is anti-symmetric. Phase $|\phi| < \pi/2$ (green - light blue - blue) results in a positive value of the instantaneous electric field. Phase $|\phi| > \pi/2$ (cyan - red - yellow) results in a negative value of the instantaneous electric field. (d) Phase of the normal component of the electric field of one of the edge modes for the armchair connection. The phase is increasing anticlockwise.

When designing topological material a trust-worthy approach to determine whether it supports topologically protected edge modes is calculating the topological invariant, Chern number.

The Chern number can be defined for both electronic and photonic crystal systems and is related to the Berry curvature concept [158]. The Berry curvature of the n^{th} band is defined as $\Omega_n(\mathbf{k}) = \nabla_{\mathbf{k}} \times A_n(k)$, where $A_n(\mathbf{k}) = i\langle u_{\mathbf{nk}} | \nabla_{\mathbf{k}} | u_{\mathbf{nk}} \rangle$ is the Berry connection, $u_{\mathbf{nk}}$ is a periodic function defined by the Bloch theorem. The integral of the Berry curvature over the first BZ is

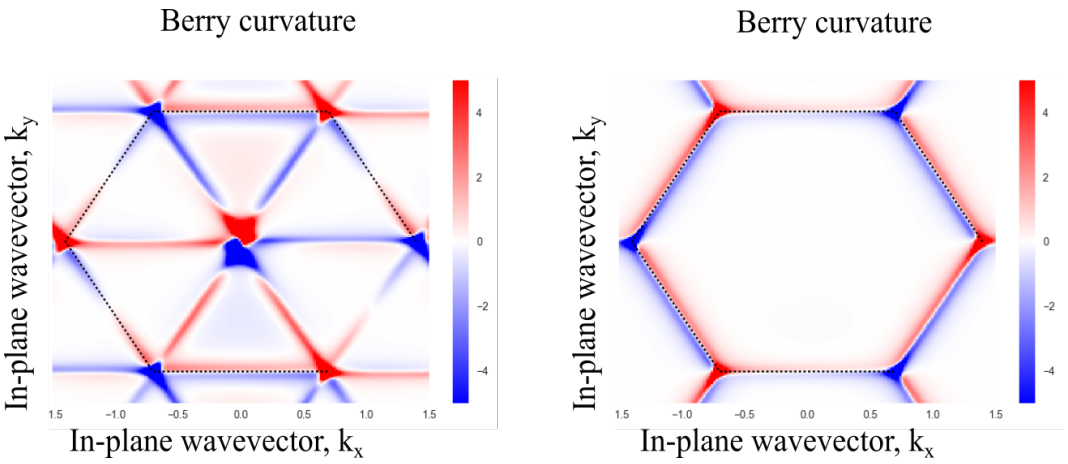

Figure 6.13: Berry curvatures of the edge mode of the studied hexagonal mesh AG system. Calculated using equivalent LC circuit model.

equal to the integer number of 2π. This integer number indicates how many topologically protected edge states are present and is called the Chern number.

The equivalent LC model can be used for calculating topological invariants and thus can help in searching hexagonal mesh AG designs that support topologically protected states. The eigen problem has to be solved for each band for the entire first BZ with fine resolution in the k-space. The accumulated phase is then calculated around a tiny closed loop for each point in the reciprocal space. While the Berry curvature is straight-forwardly defined for non-degenerate modes,it is a rather non-trivial task to calculate it when the modes are degenerate. The results of calculating the Berry curvature maps for non-degenerate modes in the studied hexagonal mesh AG system are presented in Fig. 6.13. However, further work is needed to determine the topological invariants for modes with degeneracy.

6.3 Conclusions

In conclusion, we have used a simple metallic hexagonal mesh as a microwave platform to study topological photonic edge states. An analytic LC circuit model was used to explore the band structures of surface (bulk) modes for undistorted,

contracted and expanded hexagonal meshes, as well as the edge states for semi-infinite structures with two different types of interface. We also showed that depending on the way the structures are connected, edge states can be fully protected or not. If the interface is formed along the direction Γ to M the two edge modes remain topologically protected, meaning they cross at the Γ point with no band gap, their electric field profiles are orthogonal (clockwise and anti-clockwise polarised). However if the interface is formed along the direction Γ to K the two edge modes hybridise, meaning they don't cross and have a mini gap at Γ point, and their fields turn out to be symmetrical and anti-symmetrical. A further Hamiltonian approach explained this behaviour as arising from trigonal warping. Theory and calculations are supported by experiment. Near-field scanning allowed us to determine the dispersion of both bulk and edge modes, as well as confirm modes hybridisation or full protection by means of electric field profiles.

Our technique is not limited to the microwave range. A similar approach may be applied at visible frequencies by using a laser beam focused on a plasmonic nanoantenna to excite propagating modes and measuring near-fields by Scanning Near-field Optical Microscopy (SNOM)[159–162].

CHAPTER 7

CONCLUSION AND FUTURE WORK

PhCs have been playing an important role in solid physics, helping to understand, prove and predict phenomena in optical frequencies, where fabrication, structural amendments are challenging due to the nano-scale or even impossible. We have fabricated and characterised two types of the microwave analogues of graphene comprised of vertical metallic rods and hexagonal wire mesh. These systems are extremely easy to fabricate, modify, can be analytically described, and thus make them ideal toy model for studying graphene.

Near-field measurements of the electric field were performed with the subsequent FFT of the obtained data. As expected, dispersion diagrams indicate that the studied systems support SEW featuring the well-celebrated Dirac cones in the vicinity of K and K′ points. Moreover, we observed evolution of the Dirac points in the iso-frequency plots showing how the circular shaped contours evolve into the triangular shape.

Using symmetry considerations it was shown that the upper and lower modes have symmetric and anti-symmetric charge distribution within the unit cell. This results in the vanishing of the upper mode in dispersion plots along

the high symmetry directions. Near-field measurements were used to detect symmetry of the modes at the M and K points of the BZ.

Both the studied system allows for great control over their structural parameters. Namely, by varying the length and width of the metallic wires and rods it is possible to control dispersion parameters such as the number of bands showing Dirac crossings, their frequencies and group velocity.

We also studied effects of symmetry breaking. Initial experiments showed that the presented structures are suitable for exploring various phenomena that are not easily achievable in the actual graphene. In Chapter 4 we studied an AG system comprised of metallic rods with the broken inversion symmetry. This was achieved by making the diameter of one of the rods in the unit cell larger than the other rod. The measured dispersion of the supported surface states shows PBG at the location of the previously gapless Dirac cones. In Chapter 5 a hexagonal wire mesh AG system with an asymmetric balance of the bonding wires was studied. This results in shifting the Dirac crossings in the reciprocal space which were previously present at the K point of the BZ.

As shown, modification of band structure is easily achievable in the artificial systems. Therefore, it should be possible to construct 2D waveguides for supposrted waves by combining gapless AG and the graphene structure with a purposely created band gap.

It is also known that the photonic environment of a PhC system can have a strong effect on its band structure. For example, in [163] it was theoretically demonstrated that AG comprised of dipolar meta-atoms embedded into a photonic cavity should possess two sets of Dirac points, of Type-I and Type-II. Conventional Type-I Dirac points are present due to the underlying honeycomb structure of AG while Type-II Dirac points emerge from a non-trivial winding in the light–matter interaction. By changing the cavity height, and thus tuning the light-matter coupling, one can control emergence and annihilation

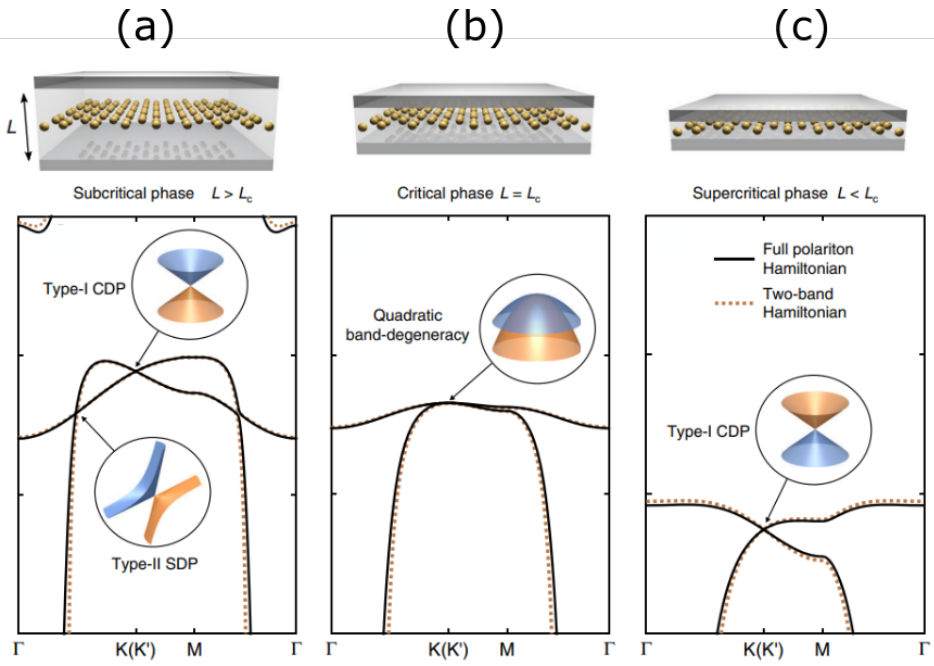

Figure 7.1: Dispersion relationship for the modes supported by the honeycomb lattice comprise of dipole resonators and embedded into a photonic cavity for (a) subcritical, (b) critical, and (c) supercritical regimes. Subcritical regime corresponds to the case when the cavity height is much bigger than the honeycomb lattice constant and features the Type-I Dirac cone and new type-II tilted Dirac cones (see inset of (a)). (b) At the critical cavity height, type-II Dirac crossings merge with the Type-I crossings resulting in a quadratic band-degeneracy at K(K′). (c) In the supercritical regime, the Type-II Dirac points annihilate each another and the massless Dirac cone re-emerges at the Type-I Dirac points. Adopted from [163]

of the Type-I and Type-II Dirac points. The authors identified the three distinct regimes, namely, the subcritical, critical and supercritical (Fig. 7.1). The subcritical phase, when the cavity walls are located far from the dipole resonators plane compared to the lattice constant, the system dispersion has the conventional Type-I Dirac crossing at the six corners of the BZ and six Type-II Dirac crossings inside the first BZ. The critical regime is characterised by the quadratic band-degeneracy, and happens when the cavity height is comparable to the lattice constant. In the supercritical regime, when the cavity walls are located at a close distance to the sample surface, only Type-I Dirac crossings are present in the corners of BZ.

At microwave frequency this can be realised with an array comprised of

metallic helices placed inside two metal plates. The fundamental resonance of a helix is proportional to the length of the unwind wire. However, geometrical parameters of the helix, such as wire thickness, number and radius of turns, etc., will not only shift the resonance frequency but will determine the coupling strength between helices in the array. Helix parameters were taken as following: wire radius - 1 mm, four turns of 2.5 mm radius, pitch - 3 mm. The distance between the closest helices is 10 mm. In Fig. 7.2 we present the preliminary modelling results. It is clear that by changing the cavity height one can modify the dispersion relationship of the modes supported by the array of helices inside the cavity. In Fig. 7.2a the dispersion is plotted for the subcritical regime. Two distinct crossings, one at the edge of the BZ and the second crossing in the middle of the BZ, can be observed. With the decreasing cavity height (panels b and c) the two modes start shifting towards each other and the two Dirac points are nearly annihilated. The flat dispersion shown in Fig. 7.2 (c) and the proximity of the modes make it difficult to resolve it experimentally. Thus, a fine tuning of the system parameters may be needed so that three different regimes are distinct and therefore could be resolved experimentally. The measurements set-up needed to study the proposed system is shown in Fig. 7.3. A cavity with movable walls and with a hole for antennas enables direct access to the near-fields of the collective dipolar elements.

Due to their unique properties AG systems are often used as a platform to study topologically protected states. The interface between the hexagonal wire mesh systems with the expanded and contracted unit cell was used to create and measure topologically protected edge modes in Chapter 6. Experimental dispersion plots of the bulk and edge states were presented. The equivalent LC circuit model developed in Chapter 5 was then used to reproduce and analyse dispersion of the bulk modes for the wire mesh AG systems with undistorted and distorted unit cells, edge mode dispersion, and how the interface type

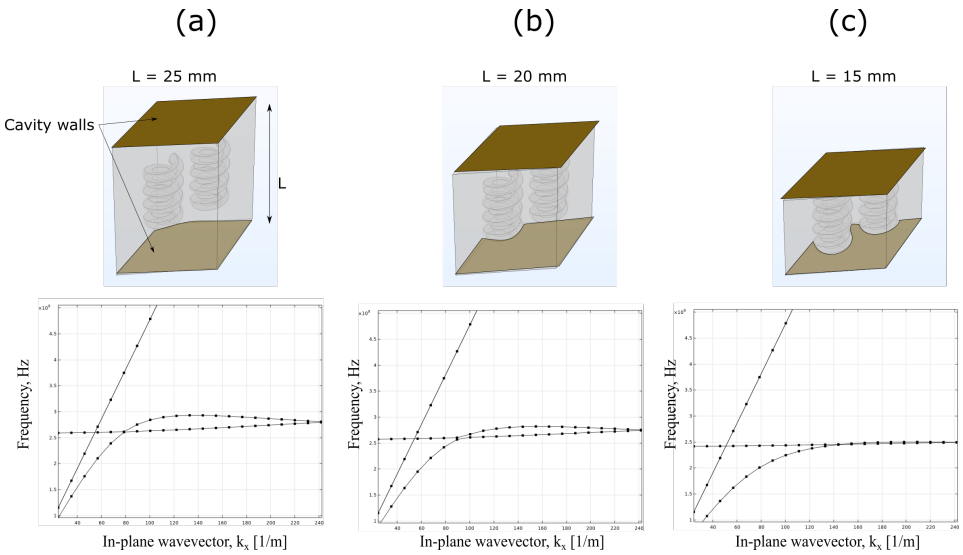

Figure 7.2: Honeycomb array of the metallic helices is placed between the two metallic plates. Helices are made of 1 mm radius wire and have 4 turns of 2.5 mm radius. Distance between the nearest helices is 10 mm. (a) Modelled dispersion for the case when distance between the metallic plates is L = 25 mm. For L= 20 mm the dispersion is plotted on (b). In (c) the dispersion relationship is plotted for the smallest possible distance between the plates. The critical regime is nearly achieved.

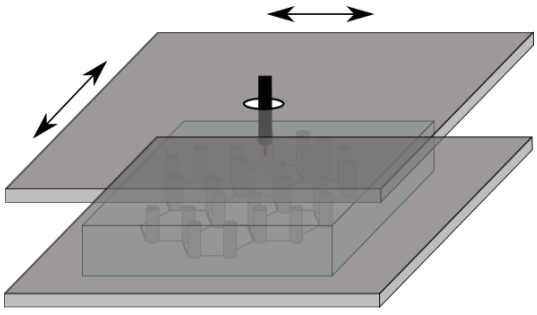

Figure 7.3: Cavity with movable side walls and with holes for the exciting and receiving antennas. Such experimental set-up allows direct access to the near fields of the collective modes of the studied system.

affects hybridisation of the edge modes. This model is a powerful modelling tool yet very simple and easy to implement. It can be programmed in an open-source IDE using a preferred programming language and solves the eigenstates problem on the order of magnitude faster than the FEM.

The equivalent LC circuit model revealed that the direction of the formed interface plays a significant role in the hybridisation of the edge modes and their topological properties. We demonstrated that if the edge interface is oriented in the Γ-to-M direction the mode remains topologically protected , whereas a different direction of the interface results in a mode mixing and opening of a mini-gap in the dispersion between the two edge modes. Effective Hamiltonian description supported these findings and explained the mechanisms of the edge modes mixing due to "trigonal warping".

The edge states studied in this work appeared to be not of a true topological nature despite showing signatures intrinsic to topological states: their dispersion connects conduction and valence bands and the system also demonstrates band inversion. To determine whether the system supports topologically protected edge modes one needs to calculate the topological invariant, Chern number. We demonstrated the principle how the equivalent LC model can be used for calculating topological invariants and thus can help in searching hexagonal mesh AG designs that support topologically protected states. However, further work is needed to determine the topological invariants for modes with degeneracy. The possible designs for exploration may include thickening selected wires, rotating the element inside the unit cell, etc.

Flat metallic mesh that promises existence of topologically protected photonic states, may advance the industry of printed circuit boards and on-chip application. In telecommunication industry, it could be used to create one-way waveguides, splitters, rotators, and etc.

BIBLIOGRAPHY

[1] J. B. Pendry, L. Martín-Moreno, and F. J. Garcia-Vidal, "Mimicking surface plasmons with structured surfaces.," *Science (New York, N.Y.)*, vol. 305, no. 5685, pp. 847–8, 2004.

[2] K. S. Novoselov, A. K. Geim, S. V. Morozov, D.-e. Jiang, Y. Zhang, S. V. Dubonos, I. V. Grigorieva, and A. A. Firsov, "Electric field effect in atomically thin carbon films," *science*, vol. 306, no. 5696, pp. 666–669, 2004.

[3] M. Dyakonov, "New type of electromagnetic wave propagating at an interface," *Sov. Phys. JETP*, vol. 67, no. 4, pp. 714–716, 1988.

[4] A. Sommerfeld, "Ueber die fortpflanzung elektrodynamischer wellen längs eines drahtes," *Annalen der Physik*, vol. 303, no. 2, pp. 233–290, 1899.

[5] J. Zenneck, "Über die fortpflanzung ebener elektromagnetischer wellen längs einer ebenen leiterfläche und ihre beziehung zur drahtlosen telegraphie," *Annalen der Physik*, vol. 328, no. 10, pp. 846–866, 1907.

[6] C. C. Cutler, *Electromagnetic waves guided by corrugated conducting surfaces*. Bell Telephone Lab, 1944.

[7] G. Goubau, "Surface waves and their application to transmission lines," *Journal of Applied Physics*, vol. 21, no. 11, pp. 1119–1128, 1950.

[8] D. L. Mills and A. A. Maradudin, "Surface corrugation and surface-polariton binding in the infrared frequency range," *Physical Review B*, vol. 39, no. 3, pp. 1569–1574, 1989.

[9] T. Leskova, A. Maradudin, and I. Simonsen, "Surface electromagnetic waves on two-dimensional rough perfectly conducting surfaces," *Revista mexicana de física*, vol. 54, no. 2, pp. 54–65, 2008.

[10] B. Auld, J. Gagnepain, and M. Tan, "Horizontal shear surface waves on corrugated surfaces," tech. rep., DTIC Document, 1976.

[11] Y. V. Gulyaev and V. Plesskii, "Slow, shear surface acoustic waves in a slow-wave structure on a solid surface," *Sov. Phys. Tech. Phys*, vol. 23, pp. 266–269, 1978.

[12] A.-R. Baghai-Wadji and A. Maradudin, "Shear horizontal surface acoustic waves on large amplitude gratings," *Applied physics letters*, vol. 59, no. 15, pp. 1841–1843, 1991.

[13] N. Glass and A. Maradudin, "Shear surface elastic waves on large amplitude gratings," *Electronics Letters*, vol. 17, p. 773, 1981.

[14] A. Maradudin and W. Zierau, "Surface acoustic waves of sagittal and shear-horizontal polarizations on large-amplitude gratings," *Geophysical Journal International*, vol. 118, no. 2, pp. 325–332, 1994.

[15] W. Rotman, "A study of single-surface corrugated guides," *Proceedings of the IRE*, vol. 39, no. 8, pp. 952–959, 1951.

[16] A. A. Maradudin, "Surface electromagnetic waves on structured perfectly conducting surfaces," in *Handbook of Surface Science*, vol. 4, pp. 223–251, Elsevier, 2014.

[17] R. H. Ritchie, "Plasma losses by fast electrons in thin films," *Physical review*, vol. 106, no. 5, p. 874, 1957.

[18] R. Ritchie, "Optical emission from surface plasmons," *physica status solidi (b)*, vol. 39, no. 1, pp. 297–308, 1970.

[19] P. J. Feibelman, "Surface electromagnetic fields," *Progress in Surface Science*, vol. 12, no. 4, pp. 287–407, 1982.

[20] A. Liebsch, *Electronic excitations at metal surfaces*. Springer Science & Business Media, 1997.

[21] H. Raether, "Surface plasmons on gratings," in *Surface plasmons on smooth and rough surfaces and on gratings*, pp. 91–116, Springer, 1988.

[22] T. W. Ebbesen, H. J. Lezec, H. Ghaemi, T. Thio, and P. Wolff, "Extraordinary optical transmission through sub-wavelength hole arrays," *Nature*, vol. 391, no. 6668, pp. 667–669, 1998.

[23] E. Economou, "Surface plasmons in thin films," *Physical review*, vol. 182, no. 2, p. 539, 1969.

[24] J. Nelayah, M. Kociak, O. Stéphan, F. J. G. de Abajo, M. Tencé, L. Henrard, D. Taverna, I. Pastoriza-Santos, L. M. Liz-Marzán, and C. Colliex, "Mapping surface plasmons on a single metallic nanoparticle," *Nature Physics*, vol. 3, no. 5, pp. 348–353, 2007.

[25] A. P. Hibbins, B. R. Evans, and J. R. Sambles, "Experimental verification of designer surface plasmons," *Science*, vol. 308, no. 5722, pp. 670–672, 2005.

[26] F. Garcia-Vidal, L. Martin-Moreno, and J. Pendry, "Surfaces with holes in them: new plasmonic metamaterials," *Journal of optics A: Pure and applied optics*, vol. 7, no. 2, p. S97, 2005.

[27] M. Qiu, “Photonic band structures for surface waves on structured metal surfaces,” *Optics express*, vol. 13, no. 19, pp. 7583–7588, 2005.

[28] S. A. Maier and S. R. Andrews, “Terahertz pulse propagation using plasmon-polariton-like surface modes on structured conductive surfaces,” *Applied Physics Letters*, vol. 88, no. 25, p. 251120, 2006.

[29] Y.-C. Lan and R.-L. Chern, “Surface plasmon-like modes on structured perfectly conducting surfaces,” *Optics express*, vol. 14, no. 23, pp. 11339–11347, 2006.

[30] E. Hendry, A. P. Hibbins, and J. R. Sambles, “Importance of diffraction in determining the dispersion of designer surface plasmons,” *Physical Review B - Condensed Matter and Materials Physics*, vol. 78, no. 23, pp. 1–10, 2008.

[31] L. Shen, X. Chen, and T.-J. Yang, “Terahertz surface plasmon polaritons on periodically corrugated metal surfaces,” *Optics express*, vol. 16, no. 5, pp. 3326–3333, 2008.

[32] B. Wang, L. Liu, and S. He, “Propagation loss of terahertz surface plasmon polaritons on a periodically structured ag surface,” *Journal of Applied Physics*, vol. 104, no. 10, p. 103531, 2008.

[33] T. Jiang, L. Shen, X. Zhang, and L.-X. Ran, “High-order modes of spoof surface plasmon polaritons on periodically corrugated metal surfaces,” *Progress In Electromagnetics Research M*, vol. 8, pp. 91–102, 2009.

[34] F. G. De Abajo and J. Sáenz, “Electromagnetic surface modes in structured perfect-conductor surfaces,” *Physical review letters*, vol. 95, no. 23, p. 233901, 2005.

[35] S. Li, M. M. Jadidi, T. E. Murphy, and G. Kumar, "Terahertz surface plasmon polaritons on a semiconductor surface structured with periodic v-grooves," *Optics express*, vol. 21, no. 6, pp. 7041–7049, 2013.

[36] A. Fernández-Domínguez, E. Moreno, L. Martin-Moreno, and F. Garcia-Vidal, "Guiding terahertz waves along subwavelength channels," *Physical Review B*, vol. 79, no. 23, p. 233104, 2009.

[37] A. Fernández-Domínguez, E. Moreno, L. Martín-Moreno, and F. García-Vidal, "Terahertz wedge plasmon polaritons," *Optics letters*, vol. 34, no. 13, pp. 2063–2065, 2009.

[38] D. F. Sievenpiper, *High-impedance electromagnetic surfaces*. University of California, Los Angeles, 1999.

[39] D. Sievenpiper, L. Zhang, R. F. Jimenez Broas, N. G. Alexöpolous, and E. Yablonovitch, "High-impedance electromagnetic surfaces with a forbidden frequency band," *IEEE Transactions on Microwave Theory and Techniques*, vol. 47, no. 11, pp. 2059–2074, 1999.

[40] S. Maci, "Metasurfing: Addressing waves on metasurfaces for realizing antennas and microwave devices," in *2011 4th IEEE International Symposium on Microwave, Antenna, Propagation and EMC Technologies for Wireless Communications*, pp. K1–K4, IEEE, 2011.

[41] G. Piefke, "The transmission characteristics of a corrugated guide," *IRE Transactions on Antennas and Propagation*, vol. 7, no. 5, pp. 183–190, 1959.

[42] Y. Chen, Z. Song, Y. Li, M. Hu, Q. Xing, Z. Zhang, L. Chai, and C.-Y. Wang, "Effective surface plasmon polaritons on the metal wire with arrays of subwavelength grooves," *Optics Express*, vol. 14, no. 26, pp. 13021–13029, 2006.

[43] A. Fernandez-Dominguez, L. Martin-Moreno, F. Garcia-Vidal, S. R. Andrews, and S. Maier, "Spoof surface plasmon polariton modes propagating along periodically corrugated wires," *IEEE Journal of Selected Topics in Quantum Electronics*, vol. 14, no. 6, pp. 1515–1521, 2008.

[44] F. Rüting, A. Fernández-Domínguez, L. Martín-Moreno, and F. García-Vidal, "Subwavelength chiral surface plasmons that carry tuneable orbital angular momentum," *Physical Review B*, vol. 86, no. 7, p. 075437, 2012.

[45] S. I. Bozhevolnyi, V. S. Volkov, E. Devaux, J.-Y. Laluet, and T. W. Ebbesen, "Channel plasmon subwavelength waveguide components including interferometers and ring resonators," *Nature*, vol. 440, no. 7083, pp. 508–511, 2006.

[46] Z. Gao, L. Shen, and X. Zheng, "Highly-confined guiding of terahertz waves along subwavelength grooves," *IEEE Photonics Technology Letters*, vol. 24, no. 15, pp. 1343–1345, 2012.

[47] T. Jiang, L. Shen, J.-J. Wu, T.-J. Yang, Z. Ruan, and L. Ran, "Realization of tightly confined channel plasmon polaritons at low frequencies," *Applied Physics Letters*, vol. 99, no. 26, p. 261103, 2011.

[48] W. Zhao, O. M. Eldaiki, R. Yang, and Z. Lu, "Deep subwavelength waveguiding and focusing based on designer surface plasmons," *Optics Express*, vol. 18, no. 20, pp. 21498–21503, 2010.

[49] X. Shen, T. J. Cui, D. Martin-Cano, and F. J. Garcia-Vidal, "Conformal surface plasmons propagating on ultrathin and flexible films," *Proceedings of the National Academy of Sciences*, vol. 110, no. 1, pp. 40–45, 2013.

[50] R. Quesada, D. Martín-Cano, F. García-Vidal, and J. Bravo-Abad, "Deep-subwavelength negative-index waveguiding enabled by coupled conformal surface plasmons," *Optics letters*, vol. 39, no. 10, pp. 2990–2993, 2014.

[51] X. Liu, Y. Feng, K. Chen, B. Zhu, J. Zhao, and T. Jiang, "Planar surface plasmonic waveguide devices based on symmetric corrugated thin film structures," *Optics express*, vol. 22, no. 17, pp. 20107–20116, 2014.

[52] X. Gao, J. Hui Shi, X. Shen, H. Feng Ma, W. Xiang Jiang, L. Li, and T. Jun Cui, "Ultrathin dual-band surface plasmonic polariton waveguide and frequency splitter in microwave frequencies," *Applied Physics Letters*, vol. 102, no. 15, p. 151912, 2013.

[53] X. Gao, L. Zhou, X. Y. Yu, W. P. Cao, H. O. Li, H. F. Ma, and T. J. Cui, "Ultra-wideband surface plasmonic y-splitter," *Optics express*, vol. 23, no. 18, pp. 23270–23277, 2015.

[54] J. Y. Yin, J. Ren, H. C. Zhang, B. C. Pan, and T. J. Cui, "Broadband frequency-selective spoof surface plasmon polaritons on ultrathin metallic structure," *Scientific reports*, vol. 5, no. 1, pp. 1–5, 2015.

[55] X. Gao, L. Zhou, Z. Liao, H. F. Ma, and T. J. Cui, "An ultra-wideband surface plasmonic filter in microwave frequency," *Applied Physics Letters*, vol. 104, no. 19, p. 191603, 2014.

[56] J. Xu, Z. Li, L. Liu, C. Chen, B. Xu, P. Ning, and C. Gu, "Low-pass plasmonic filter and its miniaturization based on spoof surface plasmon polaritons," *Optics Communications*, vol. 372, pp. 155–159, 2016.

[57] Q. Zhang, H. C. Zhang, H. Wu, and T. J. Cui, "A hybrid circuit for spoof surface plasmons and spatial waveguide modes to reach controllable band-pass filters," *Scientific reports*, vol. 5, no. 1, pp. 1–9, 2015.

[58] F. Medina, F. Mesa, and R. Marques, "Extraordinary transmission through arrays of electrically small holes from a circuit theory perspective," *IEEE Transactions on Microwave Theory and Techniques*, vol. 56, no. 12, pp. 3108–3120, 2008.

[59] A. B. Khanikaev, S. H. Mousavi, G. Shvets, and Y. S. Kivshar, "One-way extraordinary optical transmission and nonreciprocal spoof plasmons," *Physical review letters*, vol. 105, no. 12, p. 126804, 2010.

[60] F. J. Zucker, "Surface-wave antennas," in *Antenna engineering handbook*, McGraw-Hill, 1993.

[61] Y. J. Park, A. Herschlein, and W. Wiesbeck, "A photonic bandgap (PBG) structure for guiding and suppressing surface waves in millimeter-wave antennas," *IEEE Transactions on Microwave Theory and Techniques*, vol. 49, no. 10 II, pp. 1854–1859, 2001.

[62] C. Pfeiffer and A. Grbic, "A printed, broadband luneburg lens antenna," *IEEE Transactions on Antennas and Propagation*, vol. 58, no. 9, pp. 3055–3059, 2010.

[63] U. Leonhardt, "Perfect imaging without negative refraction," *New Journal of Physics*, vol. 11, no. 9, p. 093040, 2009.

[64] M. Casaletti, F. Caminita, S. Maci, M. Bosiljevac, and Z. Sipus, "New type of horn based on variable metasurface," in *2011 IEEE International Symposium on Antennas and Propagation (APSURSI)*, pp. 1048–1050, IEEE, 2011.

[65] A. Oliner and A. Hessel, "Guided waves on sinusoidally-modulated reactance surfaces," *IRE Transactions on Antennas and Propagation*, vol. 7, no. 5, pp. 201–208, 1959.

[66] G. Minatti, F. Caminita, M. Casaletti, and S. Maci, "Spiral leaky-wave antennas based on modulated surface impedance," *IEEE Transactions on Antennas and Propagation*, vol. 59, no. 12, pp. 4436–4444, 2011.

[67] R. E. Collin, *Field theory of guided waves*, vol. 5. John Wiley & Sons, 1990.

[68] P. Drude, "Zur elektronentheorie der metalle," *Annalen der Physik*, vol. 306, no. 3, pp. 566–613, 1900.

[69] S. A. Schelkunoff, "The impedance concept and its application to problems of reflection, refraction, shielding and power absorption," *Bell System Technical Journal*, vol. 17, no. 1, pp. 17–48, 1938.

[70] O. Heaviside, *Electrical papers*, vol. 2. Cambridge University Press, 2011.

[71] S. Tretyakov, *Analytical Modeling in Applied Electromagnetics*. Artech House, 2003.

[72] E. Yablonovitch, "Inhibited spontaneous emission in solid-state physics and electronics," *Physical Review Letters*, vol. 58, no. 20, pp. 2059–2062, 1987.

[73] S. John, "Strong localization of photons in certain disordered dielectric superlattices," *Physical Review Letters*, vol. 58, no. 23, pp. 2486–2489, 1987.

[74] E. Yablonovitch, T. Gmitter, and K. Leung, "Photonic band structure: The face-centered-cubic case employing nonspherical atoms," *Physical review letters*, vol. 67, no. 17, p. 2295, 1991.

[75] E. R. Brown, C. D. Parker, and E. Yablonovitch, "Radiation properties of a planar antenna on a photonic-crystal substrate," *Journal of the Optical Society of America B*, vol. 10, no. 2, p. 404, 1993.

[76] J. Joannopoulos, S. Johnson, J. Winn, and R. Meade, *Photonic Crystals: Molding the Flow of Light (Second Edition)*. Princeton University Press, 2008.

[77] S. John, "Strong localization of photons in certain disordered dielectric superlattices," *Physical review letters*, vol. 58, no. 23, p. 2486, 1987.

[78] D. Sievenpiper, M. Sickmiller, and E. Yablonovitch, "3D Wire Mesh Photonic Crystals," *Physical Review Letters*, vol. 76, no. 14, pp. 2480–2483, 1996.

[79] S. Fan, P. R. Villeneuve, and J. D. Joannopoulos, "Large omnidirectional band gaps in metallodielectric photonic crystals," *Physical Review B*, vol. 54, no. 16, pp. 11245–11251, 1996.

[80] S.-Y. Lin, E. Chow, V. Hietala, P. R. Villeneuve, and J. D. Joannopoulos, "Experimental demonstration of guiding and bending of electromagnetic waves in a photonic crystal," *Science*, vol. 282, no. 5387, pp. 274–276, 1998.

[81] F. Falcone, T. Lopetegi, M. A. G. Laso, and M. Sorolla, "Novel photonic crystal waveguide in microwave printed-circuit technology," *Microwave and Optical Technology Letters*, vol. 34, no. 6, pp. 462–466, 2002.

[82] A. Coves, A. A. San Blas, B. Gimeno, A. Díez, M. V. Andres, and V. E. Boria, "Two-dimensional photonic-crystal microwave waveguide," *Microwave and Optical Technology Letters*, vol. 39, no. 3, pp. 243–246, 2003.

[83] J. Martorell, R. Vilaseca, and R. Corbalan, "Second harmonic generation in a photonic crystal," *Applied physics letters*, vol. 70, no. 6, pp. 702–704, 1997.

[84] A. Merzlikin, A. Vinogradov, M. Inoue, A. Khanikaev, and A. Granovsky, "The faraday effect in two-dimensional magneto-photonic crystals," *Journal of magnetism and magnetic materials*, vol. 300, no. 1, pp. 108–111, 2006.

[85] S. Fan, P. R. Villeneuve, J. D. Joannopoulos, and H. A. Haus, "Channel drop filters in photonic crystals," *Optics express*, vol. 3, no. 1, pp. 4–11, 1998.

[86] L. Dekkiche and R. Naoum, "A novel all-optical switch based on a photonic crystal coupler," *Applied Sci*, vol. 7, pp. 3518–3523, 2007.

[87] O. Painter, R. Lee, A. Scherer, A. Yariv, J. O'brien, P. Dapkus, and I. Kim, "Two-dimensional photonic band-gap defect mode laser," *Science*, vol. 284, no. 5421, pp. 1819–1821, 1999.

[88] K. Inoue and K. Ohtaka, *Photonic crystals: physics, fabrication and applications*, vol. 94. Springer Science & Business Media, 2004.

[89] H.-B. Sun, S. Matsuo, and H. Misawa, "Three-dimensional photonic crystal structures achieved with two-photon-absorption photopolymerization of resin," *Applied Physics Letters*, vol. 74, no. 6, pp. 786–788, 1999.

[90] M. Campbell, D. Sharp, M. Harrison, R. Denning, and A. Turberfield, "Fabrication of photonic crystals for the visible spectrum by holographic lithography," *Nature*, vol. 404, no. 6773, pp. 53–56, 2000.

[91] T. J. Shepherd, C. R. Brewitt-Taylor, P. Dimond, G. Fixter, A. Laight, P. Lederer, P. J. Roberts, P. R. Tapster, and I. J. Youngs, "3D microwave

photonic crystals: Novel fabrication and structures," *Electronics Letters*, vol. 34, no. 8, pp. 787–789, 1998.

[92] M. Okano and S. Noda, "Analysis of multimode point-defect cavities in three-dimensional photonic crystals using group theory in frequency and time domains," *Physical Review B*, vol. 70, no. 12, p. 125105, 2004.

[93] Y.-C. Hsue, A. J. Freeman, and B.-Y. Gu, "Extended plane-wave expansion method in three-dimensional anisotropic photonic crystals," *Physical Review B*, vol. 72, no. 19, p. 195118, 2005.

[94] Z.-Y. Li and K.-M. Ho, "Application of structural symmetries in the plane-wave-based transfer-matrix method for three-dimensional photonic crystal waveguides," *Physical Review B*, vol. 68, no. 24, p. 245117, 2003.

[95] A. K. Geim and K. S. Novoselov, "The rise of graphene," *Nature materials*, vol. 6, no. 3, pp. 183–191, 2007.

[96] A. C. Neto, F. Guinea, N. M. Peres, K. S. Novoselov, and A. K. Geim, "The electronic properties of graphene," *Reviews of modern physics*, vol. 81, no. 1, p. 109, 2009.

[97] P. R. Wallace, "The band theory of graphite," *Physical review*, vol. 71, no. 9, p. 622, 1947.

[98] M. Polini, F. Guinea, M. Lewenstein, H. C. Manoharan, and V. Pellegrini, "Artificial honeycomb lattices for electrons, atoms and photons," *Nature nanotechnology*, vol. 8, no. 9, pp. 625–633, 2013.

[99] M. Plihal and A. Maradudin, "Photonic band structure of two-dimensional systems: The triangular lattice," *Physical Review B*, vol. 44, no. 16, p. 8565, 1991.

[100] S. Bittner, B. Dietz, M. Miski-Oglu, P. Oria Iriarte, A. Richter, and F. Schäfer, "Observation of a Dirac point in microwave experiments with a photonic crystal modeling graphene," *Physical Review B - Condensed Matter and Materials Physics*, vol. 82, no. 1, pp. 1–5, 2010.

[101] S. Bittner, B. Dietz, M. Miski-Oglu, and A. Richter, "Extremal transmission through a microwave photonic crystal and the observation of edge states in a rectangular Dirac billiard," *Physical Review B - Condensed Matter and Materials Physics*, vol. 85, no. 6, pp. 1–8, 2012.

[102] M. Bellec, U. Kuhl, G. Montambaux, and F. Mortessagne, "Topological transition of Dirac points in a microwave experiment," *Physical Review Letters*, vol. 110, no. 3, pp. 1–5, 2013.

[103] U. Kuhl, S. Barkhofen, T. Tudorovskiy, H.-J. J. Stöckmann, T. Hossain, L. De Forges De Parny, and F. Mortessagne, "Dirac point and edge states in a microwave realization of tight-binding graphene-like structures," *Physical Review B*, vol. 82, no. 9, p. 094308, 2010.

[104] M. Bellec, U. Kuhl, G. Montambaux, and F. Mortessagne, "Tight-binding couplings in microwave artificial graphene," *Phys. Rev. B*, vol. 88, p. 115437, 2013.

[105] G. Weick, C. Woollacott, W. L. Barnes, O. Hess, and E. Mariani, "Dirac-like plasmons in honeycomb lattices of metallic nanoparticles," *Physical review letters*, vol. 110, no. 10, p. 106801, 2013.

[106] G. Weick and E. Mariani, "Tunable plasmon polaritons in arrays of interacting metallic nanoparticles," *The European Physical Journal B*, vol. 88, no. 1, pp. 1–8, 2015.

[107] F. D. M. Haldane, “Model for a quantum hall effect without landau levels: Condensed-matter realization of the "parity anomaly",” *Physical Review Letters*, vol. 61, no. 18, pp. 2015–2018, 1988.

[108] F. D. M. Haldane and S. Raghu, “Possible realization of directional optical waveguides in photonic crystals with broken time-reversal symmetry,” *Physical Review Letters*, vol. 100, no. 1, pp. 1–4, 2008.

[109] S. Raghu and F. D. M. Haldane, “Analogs of quantum-Hall-effect edge states in photonic crystals,” *Physical Review A - Atomic, Molecular, and Optical Physics*, vol. 78, no. 3, pp. 1–21, 2008.

[110] Z. Wang, Y. Chong, J. D. Joannopoulos, and M. Soljačić, “Reflection-free one-way edge modes in a gyromagnetic photonic crystal,” *Physical review letters*, vol. 100, no. 1, p. 013905, 2008.

[111] Z. Wang, Y. Chong, J. D. Joannopoulos, and M. Soljačić, “Observation of unidirectional backscattering-immune topological electromagnetic states,” *Nature*, vol. 461, no. 7265, pp. 772–775, 2009.

[112] M. C. Rechtsman, J. M. Zeuner, Y. Plotnik, Y. Lumer, D. Podolsky, F. Dreisow, S. Nolte, M. Segev, and A. Szameit, “Photonic floquet topological insulators,” *Nature*, vol. 496, no. 7444, pp. 196–200, 2013.

[113] A. B. Khanikaev, S. H. Mousavi, W.-K. Tse, M. Kargarian, A. H. MacDonald, and G. Shvets, “Photonic topological insulators,” *Nature materials*, vol. 12, no. 3, pp. 233–239, 2013.

[114] L. Brillouin, *Wave Propagation in Periodic Structures*. McGraw-Hill Book Company, Inc., 1946.

[115] S. Tretyakov, *Analytical modeling in applied electromagnetics*. Artech House, 2003.

[116] F. Costa, A. Monorchio, and G. Manara, "An overview of equivalent circuit modeling techniques of frequency selective surfaces and metasurfaces," *The Applied Computational Electromagnetics Society Journal (ACES)*, pp. 960–976, 2014.

[117] J. B. Pendry, A. J. Holden, D. J. Robbins, and W. Stewart, "Magnetism from conductors and enhanced nonlinear phenomena," *IEEE transactions on microwave theory and techniques*, vol. 47, no. 11, pp. 2075–2084, 1999.

[118] J. D. Baena, J. Bonache, F. Martín, R. M. Sillero, F. Falcone, T. Lopetegi, M. A. Laso, J. Garcia-Garcia, I. Gil, M. F. Portillo, *et al.*, "Equivalent-circuit models for split-ring resonators and complementary split-ring resonators coupled to planar transmission lines," *IEEE transactions on microwave theory and techniques*, vol. 53, no. 4, pp. 1451–1461, 2005.

[119] S. Barkhofen, M. Bellec, U. Kuhl, and F. Mortessagne, "Disordered graphene and boron nitride in a microwave tight-binding analog," *Physical Review B - Condensed Matter and Materials Physics*, vol. 87, no. 3, pp. 1–11, 2013.

[120] K. Kim, J.-Y. Choi, T. Kim, S.-H. Cho, and H.-J. Chung, "A role for graphene in silicon-based semiconductor devices," *Nature*, vol. 479, no. 7373, pp. 338–344, 2011.

[121] S. Kim, J. Ihm, H. J. Choi, and Y.-W. Son, "Origin of anomalous electronic structures of epitaxial graphene on silicon carbide," *Physical review letters*, vol. 100, no. 17, p. 176802, 2008.

[122] Y. Guo, W. Guo, and C. Chen, "Bias voltage induced n-to p-type transition in epitaxial bilayer graphene on sic," *Physical Review B*, vol. 80, no. 8, p. 085424, 2009.

[123] J. L. McChesney, A. Bostwick, T. Ohta, T. Seyller, K. Horn, J. González, and E. Rotenberg, "Extended van hove singularity and superconducting instability in doped graphene," *Physical review letters*, vol. 104, no. 13, p. 136803, 2010.

[124] K. Novoselov, "Mind the gap," *Nature materials*, vol. 6, no. 10, pp. 720–721, 2007.

[125] G. W. Semenoff, "Condensed-matter simulation of a three-dimensional anomaly," *Physical Review Letters*, vol. 53, no. 26, p. 2449, 1984.

[126] T. Galvani, F. Paleari, H. P. Miranda, A. Molina-Sánchez, L. Wirtz, S. Latil, H. Amara, and F. Ducastelle, "Excitons in boron nitride single layer," *Physical Review B*, vol. 94, no. 12, p. 125303, 2016.

[127] N. Meinzer, W. L. Barnes, and I. R. Hooper, "Plasmonic meta-atoms and metasurfaces," *Nature Photonics*, vol. 8, no. 12, pp. 889–898, 2014.

[128] L. Tarruell, D. Greif, T. Uehlinger, G. Jotzu, and T. Esslinger, "Creating, moving and merging dirac points with a fermi gas in a tunable honeycomb lattice," *Nature*, vol. 483, no. 7389, pp. 302–305, 2012.

[129] N. I. Zheludev and Y. S. Kivshar, "From metamaterials to metadevices," *Nature materials*, vol. 11, no. 11, pp. 917–924, 2012.

[130] A. Chutinan and S. Noda, "Waveguides and waveguide bends in two-dimensional photonic crystal slabs," *Physical review B*, vol. 62, no. 7, p. 4488, 2000.

[131] Y. N. Dautova, A. V. Shytov, I. R. Hooper, J. R. Sambles, and A. P. Hibbins, "Gapless states in microwave artificial graphene," *Applied Physics Letters*, vol. 110, no. 26, p. 261605, 2017.

[132] T. Ando, T. Nakanishi, and R. Saito, "Berry's phase and absence of back scattering in carbon nanotubes," *Journal of the Physical Society of Japan*, vol. 67, no. 8, pp. 2857–2862, 1998.

[133] E. McCann and M. Koshino, "The electronic properties of bilayer graphene," *Reports on Progress in physics*, vol. 76, no. 5, p. 056503, 2013.

[134] J. Azizi, A. Phirouznia, and K. Hasanirokh, "Anisotropic resistivity of the monolayer graphene in the trigonal warping and connected fermi curve regimes," *Physica E: Low-dimensional Systems and Nanostructures*, vol. 68, pp. 28–32, 2015.

[135] Y. Y. Iossel, E. Kochanov, and M. Strunskii, *The calculation of electrical capacitance*. 1971.

[136] F. E. Terman, *Radio Engineers' Handbook*. McGraw-Hill Book Company, Inc., 1943.

[137] V. M. Pereira, A. C. Neto, and N. Peres, "Tight-binding approach to uniaxial strain in graphene," *Physical Review B*, vol. 80, no. 4, p. 045401, 2009.

[138] G. M. Dresselhaus, "Outline •! Historical Graphene to Graphene path •! Carbon Nanotubes as Prototype Materials •! Disordered Graphite •! Graphene and Graphene Ribbons •! Looking to the Future of Carbon Nanostructures," *APS March Meeting*, 2008.

[139] B. A. Bernevig and T. L. Hughes, *Topological insulators and topological superconductors*. Princeton university press, 2013.

[140] S. Roche and S. O. Valenzuela, *Topological insulators: Fundamentals and perspectives*. John Wiley & Sons, 2015.

[141] L. Lu, J. D. Joannopoulos, and M. Soljačić, "Topological photonics," *Nature photonics*, vol. 8, no. 11, pp. 821–829, 2014.

[142] A. B. Khanikaev and G. Shvets, "Two-dimensional topological photonics," *Nature Photonics*, vol. 11, no. 12, p. 763, 2017.

[143] K. Fang, Z. Yu, and S. Fan, "Microscopic theory of photonic one-way edge mode," *Physical Review B*, vol. 84, no. 7, p. 075477, 2011.

[144] Y. Poo, R.-x. Wu, Z. Lin, Y. Yang, and C. T. Chan, "Experimental realization of self-guiding unidirectional electromagnetic edge states," *Phys. Rev. Lett.*, vol. 106, p. 093903, Mar 2011.

[145] K. v. Klitzing, G. Dorda, and M. Pepper, "New method for high-accuracy determination of the fine-structure constant based on quantized hall resistance," *Physical review letters*, vol. 45, no. 6, p. 494, 1980.

[146] O. P. Sushkov and A. C. Neto, "Topological insulating states in laterally patterned ordinary semiconductors," *Physical review letters*, vol. 110, no. 18, p. 186601, 2013.

[147] L.-H. Wu and X. Hu, "Scheme for achieving a topological photonic crystal by using dielectric material," *Physical review letters*, vol. 114, no. 22, p. 223901, 2015.

[148] Y. Yang, Y. F. Xu, T. Xu, H.-X. Wang, J.-H. Jiang, X. Hu, and Z. H. Hang, "Visualization of a unidirectional electromagnetic waveguide using topological photonic crystals made of dielectric materials," *Physical review letters*, vol. 120, no. 21, p. 217401, 2018.

[149] X. Zhu, H.-X. Wang, C. Xu, Y. Lai, J.-H. Jiang, and S. John, "Topological transitions in continuously deformed photonic crystals," *Physical Review B*, vol. 97, no. 8, p. 085148, 2018.

[150] J. Noh, W. A. Benalcazar, S. Huang, M. J. Collins, K. P. Chen, T. L. Hughes, and M. C. Rechtsman, "Topological protection of photonic mid-gap defect modes," *Nature Photonics*, vol. 12, no. 7, pp. 408–415, 2018.

[151] M. Honari-Latifpour and L. Yousefi, "Topological plasmonic edge states in a planar array of metallic nanoparticles," *Nanophotonics*, vol. 8, no. 5, pp. 799–806, 2019.

[152] S. Barik, H. Miyake, W. DeGottardi, E. Waks, and M. Hafezi, "Two-dimensionally confined topological edge states in photonic crystals," *New Journal of Physics*, vol. 18, no. 11, p. 113013, 2016.

[153] C. He, X. Ni, H. Ge, X.-C. Sun, Y.-B. Chen, M.-H. Lu, X.-P. Liu, and Y.-F. Chen, "Acoustic topological insulator and robust one-way sound transport," *Nature physics*, vol. 12, no. 12, pp. 1124–1129, 2016.

[154] Z.-G. Geng, Y.-G. Peng, Y.-X. Shen, D.-G. Zhao, and X.-F. Zhu, "Topologically protected edge transport of sound in coupled cavities of a modified honeycomb lattice," *Journal of Physics: Condensed Matter*, vol. 30, no. 34, p. 345401, 2018.

[155] Z. Zhu, Y. Cheng, and U. Schwingenschlögl, "Band inversion mechanism in topological insulators: A guideline for materials design," *Physical Review B*, vol. 85, no. 23, p. 235401, 2012.

[156] R. Jackiw and C. Rebbi, "Solitons with fermion number 1/2," *Physical Review D*, vol. 13, no. 12, p. 3398, 1976.

[157] Y. N. Dautova, A. V. Shytov, J. R. Sambles, and A. P. Hibbins, "Microwave topological edge modes in a flat hexagonal wire mesh [in preparation]," *Supplementary materials [calculatinos done by Andrey Shytov]*.

[158] B. Simon, "Holonomy, the quantum adiabatic theorem, and berry's phase," *Physical Review Letters*, vol. 51, no. 24, p. 2167, 1983.

[159] F. Keilmann and R. Hillenbrand, "Near-field microscopy by elastic light scattering from a tip," *Philosophical Transactions of the Royal Society of London. Series A: Mathematical, Physical and Engineering Sciences*, vol. 362, no. 1817, pp. 787–805, 2004.

[160] Z. Fei, A. Rodin, G. Andreev, W. Bao, A. McLeod, M. Wagner, L. Zhang, Z. Zhao, M. Thiemens, G. Dominguez, *et al.*, "Gate-tuning of graphene plasmons revealed by infrared nano-imaging," *Nature*, vol. 487, no. 7405, p. 82, 2012.

[161] F. Walla, M. M. Wiecha, N. Mecklenbeck, S. Beldi, F. Keilmann, M. D. Thomson, and H. G. Roskos, "Anisotropic excitation of surface plasmon polaritons on a metal film by a scattering-type scanning near-field microscope with a non-rotationally-symmetric probe tip," *Nanophotonics*, vol. 7, no. 1, pp. 269–276, 2018.

[162] F. Walla, F. Bürkle, I. S. Sinev, M. Wiecha, N. Mecklenbeck, K. Ladutenko, R. Malureanu, F. Komissarenko, A. V. Lavrinenko, A. Bogdanov, *et al.*, "Near-field observation of guided-mode resonances on a metasurface via dielectric nanosphere excitation," *ACS Photonics*, 2018.

[163] C.-R. Mann, T. J. Sturges, G. Weick, W. L. Barnes, and E. Mariani, "Manipulating type-i and type-ii dirac polaritons in cavity-embedded honeycomb metasurfaces," *Nature communications*, vol. 9, no. 1, pp. 1–11, 2018.